Design, additive manufacturing and performance evaluation of auxetic structures

A thesis submitted

in partial fulfillment of the requirements

for the degree of

Doctor of Philosophy

by

Niranjan Kumar Choudhry
Roll No.-176103017

Under Supervision of

Dr. Biranchi Panda

Department of Mechanical Engineering

Indian Institute of Technology Guwahati

Guwahati, India

January 2024

Dedicated to

My Parents

(Late Smt. Lalmukhi Devi and Shri Deen Bandhu Choudhary)

Department of Mechanical Engineering
Indian Institute of Technology Guwahati
Guwahati-781039, INDIA

CERTIFICATE

This is certified that the work contained in the thesis entitled "**Design, additive manufacturing and performance evaluation of auxetic structures**", submitted by **Niranjan Kumar Choudhry**, Roll No. 176103017 to the Indian Institute of Technology Guwahati for the degree of Doctor of Philosophy has been carried out under my supervision in the Department of Mechanical Engineering, Indian Institute of Technology Guwahati. The thesis work, in my opinion, has reached the requisite standard fullling the requirements for the degree of Doctor of Philosophy.

This work has not been submitted elsewhere for the award of any other degree or diploma.

Dr. Biranchi Panda
Assistant Professor
Department of Mechanical Engineering
Indian Institute of Technology Guwahati
Guwahati-781039, Assam, India

Date: 05.01.2024

Declaration

I, Niranjan Kumar Choudhry (Roll No.: 176103017) declare that this written submission represents my idea in my own words and where other's ideas or words have been included, I have adequately cited and referenced the original sources. I also declare that I have adhered to all principles of academic honesty and integrity and have not misrepresented or fabricated or falsified any idea/data/fact/source in my submission. I understand that any violation of the above will be cause for disciplinary action by the institute can also evoke penal action from the sources which have thus not been properly cited or from whom proper permission has not been taken when needed.

Niranjan Kumar Choudhry
Roll No.: 176103017
Department of Mechanical Engineering
Indian Institute of Technology Guwahati
Guwahati-781039, Assam, India

Date: 05/01/2024

ACKNOWLEDGEMENT

I would like to take this opportunity to pay my deep sense of respect and sincere gratitude to my supervisor, Dr. Biranchi Panda, Department of Mechanical Engineering, Indian Institute of Technology Guwahati, Assam-781039 for his invaluable advice, resourceful guidance, inspiring instructions, active supervision and constant encouragement without which it would not have been possible for me to reach to this point.

I also wish to thank to my doctoral committee members, Dr. Swarup Bag, Dr. S. Senthilvelan, Dr. Santosha Kumar Dwivedy and Dr. Subashisa Dutta for their guidance, moral support and encouragement to my ideas in the subject as well as other areas of innovations. I must not miss the opportunity to thank all the Professors of Mechanical Engineering Department, Indian Institute of Technology Guwahati, whose motivation and timely help molded me in all possible forms.

I would like to acknowledge Central instrument facility (CIF) of IIT Guwahati for kind assistance to carry out my research work. Last, but not least, I am deeply indebted to my parents (Late Smt. Lalmukhi Devi and Shri Deen Bandhu Choudhary) for the sacrifices they have borne to ensure the fulfillment of my dreams. I would like to thank my brother Neeraj Kumar Choudhry, my wife Sushila Kachhap and my daughter Ditya Niranjana Choudhry for their support and motivation during my PhD.

The time I spent with all my friends and seniors at IIT Guwahati, Dr. Manjesh Kumar, Dr. Abhinav Kumar, Dr. Mukesh Kumar, Ambrish Singh, Hari Narayan Singh Yadav, Ranajit Mahanti, Dhrutiman Dey, Ramalingai Booda, Shubham Kumar, Dr. Kaustubh Khaire, Dr. Mukesh Sharma who made my life enjoyable and memorable on the campus.

NIRANJAN KUMAR CHOUDHRY

Abstract

Synergistic effects of 3D printing and composites expand the opportunities for designing high-performance light weight structures like auxetic lattices, that exhibit negative Poisson's ratio. This thesis endeavors design, simulation, and experimental verification of 3D printed auxetic structures with an aim to attain improved energy absorption and young's modulus by suggesting intuitive designs such as introducing low rotational stiffness nodes, vertical structs, and tessellation (arrangement of basic building block in the design space) followed by characterisation of compressive behaviour of cementitious composites embedded with 3D printed re-entrant structure.

The development of high-performance lightweight lattices with improved energy absorption and stiffness has attributes has attracted considerable attention in the research community. In this work, conventional auxetic structure (2D re-entrant honeycomb) was tested under quasi-static compressive loading. As the estimating energy absorption performance of auxetic structure during the design phase has been observed indispensable, finite element method (FEM) based simulation having appropriate boundary conditions has been developed to calculate the stress-strain response in corroboration with experimental measurement. It was found that rotational stiffness of the node influenced the energy absorption of the structure. Based on this finding, a novel auxetic unit cell with low rotational stiffness called, 'modified re-entrant auxetic structure' was designed, 3D printed and tested under compressive loading. With the help of statistical models (derived by response surface methodology) and parametric study, it has been shown that link length ratio has the highest influence on the energy absorption properties followed by joint angle effects. The crushing analysis indicates that the optimized structure outperforms (+36%) regular re-entrant honeycomb in terms of energy absorption performance, but compressive strength increment was marginal.

Two new auxetic lattices were designed by selectively introducing vertical ligaments to the modified re-entrant lattice and 3D printed via fused filament fabrication technique. The deformation patterns were investigated both via Finite Element (FE) simulations and experiments to understand the role of vertical ligaments under quasi-static compression. The measured mechanical characteristics of the two lattices were compared to conventional re-entrant honeycomb lattices of the same relative density. Despite higher Poisson's ratio, the specific energy absorption of two 3D printed auxetic lattices (Type A and Type B) were 165% and 147% higher than conventional re-entrant honeycomb respectively due to deformation of higher relative density cells at higher strains. Similarly, the elastic moduli of the Type A and

B lattices exhibit an improvement of about 355% and 198% with respect to conventional re-entrant honeycomb due to reduced bending dominated behaviour. The theoretical formulae for effective Young's modulus of the proposed structures were also developed using an energy-based approach and validated by FE results.

Next, interlocking designs based on tessellation such as 'edge-to-edge' 'non-edge-to-edge' and 'overlapping' were explored using the Type A auxetic structure. The findings of this study suggest that the strength, Young's modulus, energy absorption capacity and Poisson's ratio of auxetic lattices can be tailored by applying different tessellation strategies. The FE results corroborated by experiments unveil the role of tessellation on the effective mechanical properties of tessellated lattices. The results indicate that the overlapping tessellation offers highest Young's modulus and yield strength among all tessellated structures, which makes it most suitable for load-bearing applications. On the other hand, overlapping tessellation offers highest specific energy absorption without any interface failure. To understand the significance of auxetic structures, 3D printed auxetics were used to design high performing cementitious composites to strengthen existing structures due to their negative Poisson's ratio and high Young's modulus. The auxetics were used as reinforcing meshes into cementitious mortar matrix and tested in compression to understand their failure patterns, load-displacement responses, ductility and energy absorption. Despite lower peak stress, the lattice reinforced composites have higher yield strain than plain concrete. It was confirmed that Young's modulus of cementitious composite increases with increase in Poisson's ratio and Young's modulus of auxetic lattice and it can be accurately estimated using modified Hashin-Shtrikman model. Due to higher failure strain, auxetic reinforcement leads to larger plateau region and hence, higher energy absorption capacity.

Table of Contents

List of Figures

List of Tables

Chapter 1 Introduction

In this chapter, a general introduction to auxetic re-entrant structures, and systematic literature review on the stiffness and energy absorption performance of auxetic re-entrant structures made by the FDM 3D printing technique is presented. Further, research gap and motivation, objectives, scope, and organization of the thesis is included. [1]

[1]A portion of this chapter has been published in:

Choudhry, N. K., Panda B, Dixit US. Energy Absorption Characteristics of Fused Deposition Modeling 3D Printed Auxetic Re-entrant Structures : A Review. J Mater Eng Perform 2023. https://doi.org/10.1007/s11665-023-08243-3.

1.1 Overview

There is a great need for researchers to apply scientific approaches to enhance the understanding of auxetic materials and develop new knowledge toward improving the mechanical properties of auxetic structures for various applications. The overall goal of the research presented in this dissertation is to contribute to the development of new auxetic designs using additive manufacturing technologies. To achieve this goal, this dissertation is oriented toward overcoming the trade-off between auxetic behaviour and stiffness, while exploring the opportunities offered by this technology, such as the ability to fabricate tessellated structures with controlled architecture, in order to generate novel mechanical responses. This dissertation demonstrates a pathway to achieve novel auxetic cementitious composites with excellent compressive ductility using additive manufacturing on a small scale, that can enable new approaches in the design and fabrication of civil infrastructure components on a large scale.

1.2 Literature review

The word metamaterial is derived from two words one from the greek word “meta” which means ‘beyond’ and the other from the latin word “material” has meaning ‘matter or material’. So metamaterial is an engineered material which full fills the required properties which is not present in naturally occurring materials [1, 2]. The properties exhibited by metamaterials are not only dependent on the properties of their base material but are highly dependent on the design (i.e. shape, size, geometry, orientation and arrangements) of their unit cells from which they are made. It is first used for optical devices [1][3] and thereafter in acoustics and mechanics [4]. So, metamaterials can be classified into the following categories as optical metamaterials, acoustic metamaterials and mechanical metamaterials.

1.2.1 Cellular lattice structures

Cellular lattice structures also called mechanical metamaterials are solids made of by hollow or closed cells joined together at the edges or faces of the unit cell. In other words, a Cellular lattice structure is formed by filling the space by cells where cells are joined with the edges or sides of the cells. The word ‘cell’ used here comes from the Latin word ‘cella’, which means an enclosed space or a small compartment. The functional and structural properties of lattice structure depend on many factors such as the topology of the unit cell, the material being used, the relative density of the lattice structure and the manufacturing method, etc [5]. Cellular lattice structures exhibit unique mechanical properties such as higher energy absorption, higher

indentation resistance, higher fracture toughness, good compressive strength, and so on due to their designed nano/micro-architecture [3, 6]. Such micro- or nano-architected lattice cellular structures find applications in a wide range of fields including robotics, medical, soft electronics, sensors, acoustic cloaking, automobile, defense, aerospace and energy harvesting [3, 5–7].

1.2.1.1 Classification of cellular lattice structures

Cellular solids based on their arrangement of unit cells can be classified into two groups; periodic cellular structures and stochastic cellular structures. In periodic cellular structure, the cells of a lattice are translated in a given direction and are ordered, and showing repeatability while in stochastic structure the design space is filled randomly with the unit lattice cell/cells. Generally, natural cellular structures are stochastic, while man-made lattices can be both [8, 9].

Based on the movement of the fluid within the space occupied by the cells of a cellular solid, cellular lattice can be again classified into two groups; open cellular lattice structures and closed cellular lattice structures. The space is solely bounded by the edges of the unit cells in an open cellular solid which allows easy movement of fluid through them. Strut base lattices are examples of open cellular solids. On the other hand, the unit cell of closed cellular lattice structures is closed by the plates which form the wall of the unit cell, and space within the cell is occupied with fluid (generally air). In the closed cellular lattice structures the movement of fluid from one cells to the other cells is restricted. A honeycomb is an example of a closed cellular solid [5].

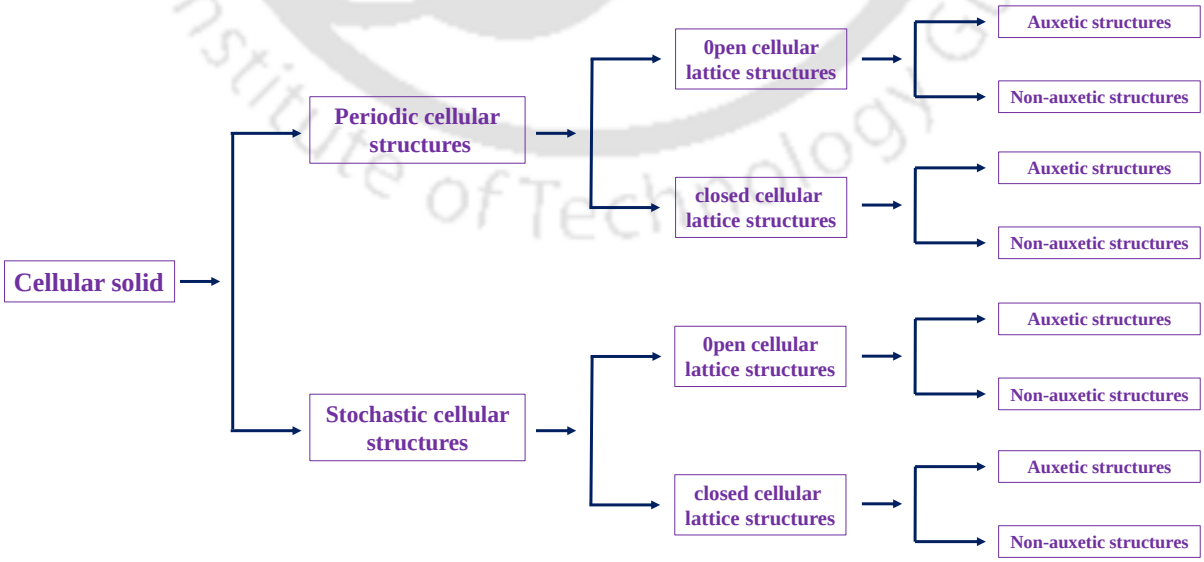

Fig. 1.1 Classification of cellular solids

Another way of classifying cellular solids is based on their Poisson's ratio. Cellular solids can be classified into two groups; Auxetic lattice structure and no-auxetic lattice structure. Auxetic structures are a class of cellular structures that exhibit lateral expansion under tension (conversely lateral contraction under compression) and hence show negative Poisson's ratio (NPR) [10], while non-auxetic structures show lateral compression under tension. Fig. 1.1 shows the classification of cellular solids.

1.2.2 Auxetic structure and it's properties

Auxetic metamaterials constitute a class of mechanical metamaterials that have negative Poisson's ratio (NPR) at the macro-scale due to their designed nano/micro-architecture [3]. Auxetic structures exhibit exceptional properties in comparison to conventional materials due to their unique architectural design; such as higher specific stiffness, higher compressive strength, higher specific energy absorption ability, higher impact resistance, enhanced indentation resistance, enhanced fracture toughness, etc. [11, 12]. Inspiration for the design of such structures often comes from naturally occurring materials such as cork and sponge; their design can be parametrically tailored to suit various engineering applications [8, 13]. In recent years, due to advancements in additive manufacturing processes, extensive studies have been carried out on auxetic structures for different applications.

1.2.2.1 Types of auxetic structure

Auxetic structures further can be classified as re-entrant honeycomb structure (RH), chiral, rotating rigid structure, origami-based, Kirigami-Based and perforated structures. Fig. 1.2(a) depicted pictorially classification and applications of the auxetic structures. Unlike conventional material, auxetic materials or structures shrink during compression and expand during tension (Fig. 1.2(b)).

Evans [10] used the term "auxetics" first time for those structures or materials, which show a negative Poisson's ratio (NPR). Almgren [14] first introduced a new type of auxetic structure called '2D re-entrant honeycomb structure' in 1985 by introducing a strut in the honeycomb structure. The structure exhibits a NPR under compression and it is very sensitive to the structural design and material being used. Basically, re-entrant structures are closed polygons that have at least one negative angle (internal angle more than 180°). Thereafter many re-entrant structures such as star re-entrant [15–17], hierarchical star re-entrant [18], double arrowhead [19–21], augmented re-entrant honeycomb (ARH) [22], graded re-entrant [23] and re-entrant chiral auxetic (RCA) [24] have been proposed. These structures exhibit NPR under

compression. The Poisson's ratio of auxetic materials is very sensitive to the architectural design and material being used.

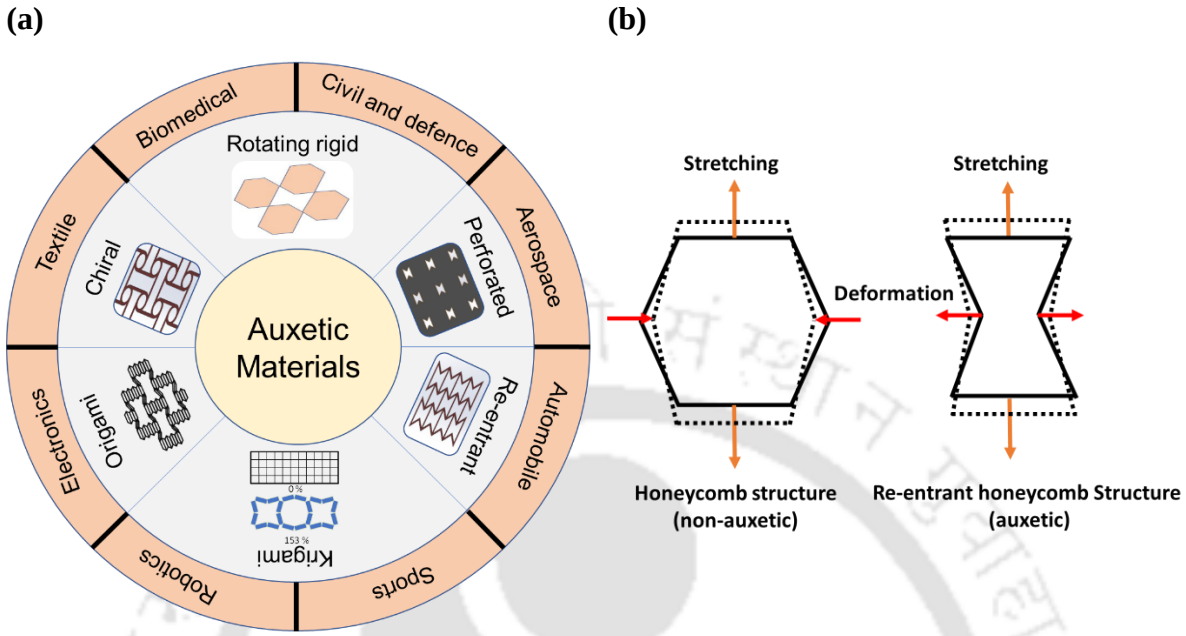

Fig. 1.2 (a) Classification and applications of auxetic structures and (b) effect of loading on auxetic and non-auxetic structures

In the recent years, as additive manufacturing technology has advanced, the fabrication and testing of 3D auxetic structures have become possible. There is a growing focus on examining the mechanical properties of these structures. Lu et al. [25] developed augmented re-entrant honeycomb structure from 2D auxetic re-entrant structures. 3D augmented re-entrant cellular structure (ARCS) made from two materials stiff and soft. Shengyu Duan et al. [26] used the 2D NPR unit cell and arranged in the out-of-plane direction in three-dimensional space to generate the 3D NPR structure. Gao et al. [27] conducted experiments to assess the crushing behavior of a 3D double-arrowhead lattice and subsequently investigated its crashworthiness.

1.2.2.2 Re-entrant honeycomb structure and it's mechanical behaviour

Basically, re-entrant structures are closed polygons that have at least one negative angle (internal angle more than 180°). Many researchers have explored the 3D printed 2D re-entrant structures and revealed their mechanical properties due to their simplicity and auxeticity [7, 11, 28–30]. In this section, particular attention is paid to the in-plane crushing response of RH structure and its mechanical behavior; specifically stiffness and energy absorption behavior; of Fused deposition modeling (FDM) printed where lattice structures are crushed quasi-statically (strain rates in the range of 10^{-5}~1 s^{-1}). The energy absorption capacity (in MJ/m^3) of any

lattice structure is determined by the area under the stress-strain curve starting from the beginning and covering up to the onset of densification.

Deformation mechanism:- The deformation mechanism unfolds what is happening to the different ligaments when it is subjected to compressive loading. The structures exhibit the elastic-plastic collapse behavior in three distinct stages— elastic regime, plateau regime and densification regime [5, 31, 32] at the macro-scale as shown in Fig. 1.3(a & b). The elastic regime is the first stage where the structures undergo linear-elastic deformation. During the linear elastic compression phase, inclined members experience axial, bending and shear loading [8, 33]. In the linear elastic stage, when a compressive load was applied, the cells of the RH structure deformed uniformly throughout the lattice and reached the maximum value. The cell walls which were parallel to the loading direction exhibited their behavior like an end-loaded column and buckled when the load exceeded Euler buckling load, while the other inclined cell walls bent (Fig. 1.3(a)). At the node where three walls meet, deformation was controlled by the rotational stiffness of the node. The inclined walls affected rotational stiffness greately as they determined the degree of constraint to rotation [8] and led to buckling and bending of the cell walls. Due to this, moments were generated and responsible for the sideways collapse of the cell. The stiffness and yield stress are always greater than those of the perpendicular loading condition.Further, as compression continues the stress in the inclined member reaches to its critical stress, and the cell collapses near the joint due to the formation of a plastic hinge [5, 34]. Elastic regime is mostly governed by the bending performance of the inclined members.

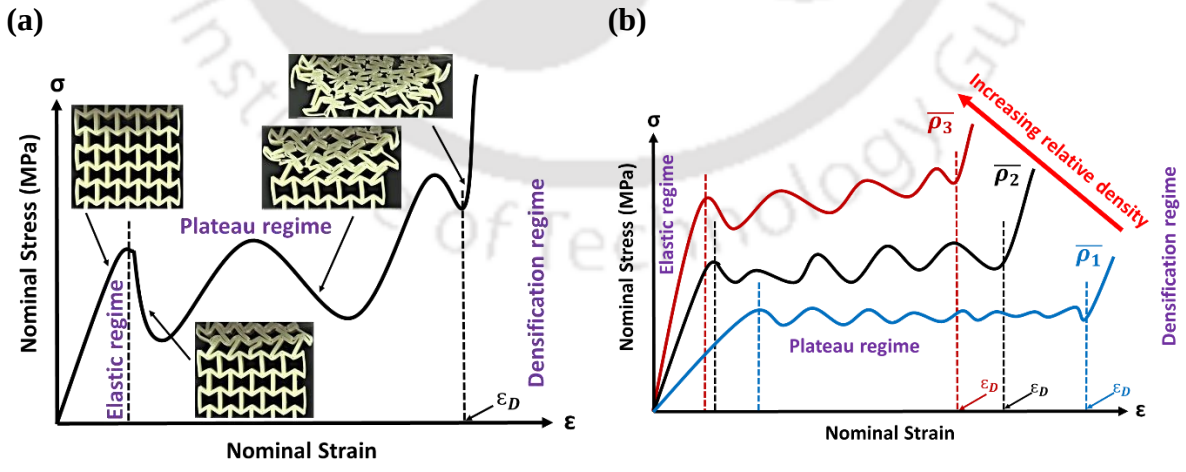

Fig. 1.3 Quasi-static compression response of re-entrant auxetic structures (a) Stress-strain response of re-entrant auxetic structures and (b) Effect of strut wall thickness on the stress-strain response of a re-entrant auxetic structure

In the second stage, viz. plateau regime (post-yielding), the structure starts deforming plastically resulting in a long plateau region. In this stage, the strut behaves like a perfectly-rigid plastic material, and the cell collapses either due to plastic hinge formation or due to the buckling, in case the load in the member exceeds Euler buckling load. Once all the cells present in a row of the structure collapse, the deformation waves move to the other row. This continues till whole structure collapses. During the plateau regime, stress peaks and valleys are formed. Peaks are formed when cells of the deforming row resist the loading before the start of collapse while valleys are formed when cells of the deforming rows completely collapse. Finally, in the densification regime, when all the rows of the structure collapse, there is a sharp increase in the stress due to the compaction of the cells (as within the compaction phase the performance is determined by the matrix material and not by the structure [35] and the stiffness of the matrix material is higher than the structure). In the compaction phase, the stress-strain behavior of the structure is totally controlled by the material of the structure. The failure of re-entrant honeycomb structure follows a bending-dominated mechanism [36].

Effect of wall thickness:- Fig. 1.3(b) shows the effect of strut wall thickness on the stress-strain response of a re-entrant auxetic structure. The increase in relative density is mainly due to an increase in the wall thickness of struts; the geometry of the structure remains unchanged. It was found that a thick-walled re-entrant honeycomb structure deformed differently than a thin-walled re-entrant honeycomb structure [37]. As the thickness of the lattice wall increases there is a sharp increase in the stiffness and yield stress, while the elastic regime reduces.

There is an impact of lattice wall thickness on the plateau regime also. Due to the increase in wall thickness, there is a change in the deformation patterns. For perpendicular loading conditions, it forms a vertical V-like deformation pattern during the early stage of compression as the cell at the top-mid part moves towards the interior-mid portion. As compression continues cell rupture starts along with cell wall movement, which is responsible for the change of the deformation pattern from vertical V mode to Y mode and finally to X mode. In the case of parallel loading conditions, due to an increase in the thickness of the cell wall of the structure, the distance between the walls reduces leading to early failure (due to early percolation of contacts between cell walls) [8]. This reduces the onset of densification which ultimately reduces the total energy absorption. The thicker wall of the cell results in early densification with higher plateau stress, and a reduction in energy absorption capacity. Hence, thicker walls are undesirable.

Ligament addition and geometric tailoring:- In this method, mechanical performance such as energy absorption and stiffness of the regular re-entrant structure is improved either by geometric tailoring or ligament addition or by combining both. A re-entrant structure with its geometrical parameter is shown in Fig. 1.4, where l, h, t and θ represent the length of inclined ligaments, the height of straight ligaments, the thickness of ligaments and the angle between the straight and inclined ligaments, respectively.

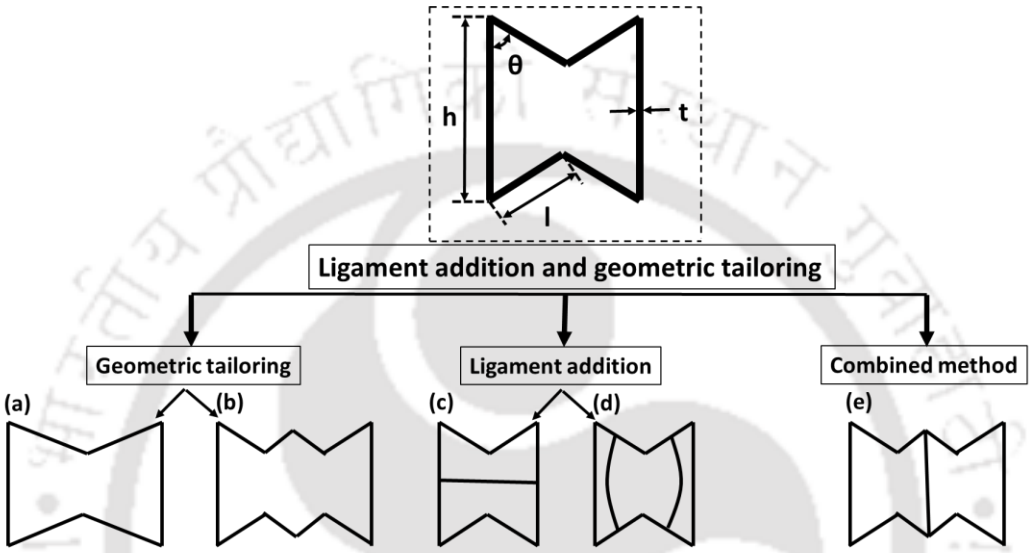

Fig. 1.4 Different design methodologies belong to ligament addition and geometric tailoring method: (a) geometric tailoring due to changes in the geometrical parameters, (b) geometric tailoring by splitting the ligaments, (c) ligament addition perpendicular to the straight ligament, (d) ligament addition parallel to the straight ligament and (e) combined method. In all cases, the loading direction is parallel to the straight ligament

In the geometric tailoring method, the structures are developed either by varying the geometric parameters (as shown in Fig. 1.4) or by introducing lower node connectivity by splitting the ligaments. It has been observed that the key factors for designing the new re-entrant structure by varying the geometric parameters are θ and h/l ratio designated by α. Fig. 1.5(a & b) shows the effect of re-entrant angle θ and α on the normalized Young's modulus. Normalized Young's modulus is the ratio of stiffness of the lattice structure E to that of base material E_s [38]. The normalization helps in comparing two designs of different materials. For loading parallel to the straight ligament, the influence of the re-entrant angle (identified by the slope of the curve) on the normalized Young's modulus is higher for a smaller re-entrant angle and it reduces as the re-entrant angle increases; it becomes less effective at high re-entrant angle (Fig. 1.5(a)) [38, 39]. For loading perpendicular to the straight ligament, the re-entrant angle has opposite trend for the normalized Young's modulus. For smaller re-entrant angles, it

is less dominant and becomes more dominating as re-entrant angles increase as can be seen in Fig. 1.5(b).

For both loading conditions, the effect of α on the normalized Young's modulus is higher at lower re-entrant angles and its effect reduces as re-entrant angles increased. Similar patterns are reported by the researchers who proposed new re-lattice designs by changing the design parameters [40–42]. For all the cases of small re-entrant angles, the normalized Young's modulus is the highest when the loading is parallel to the straight ligament. The re-entrant angle has a strong influence on the mechanical performance of the re-entrant lattice.

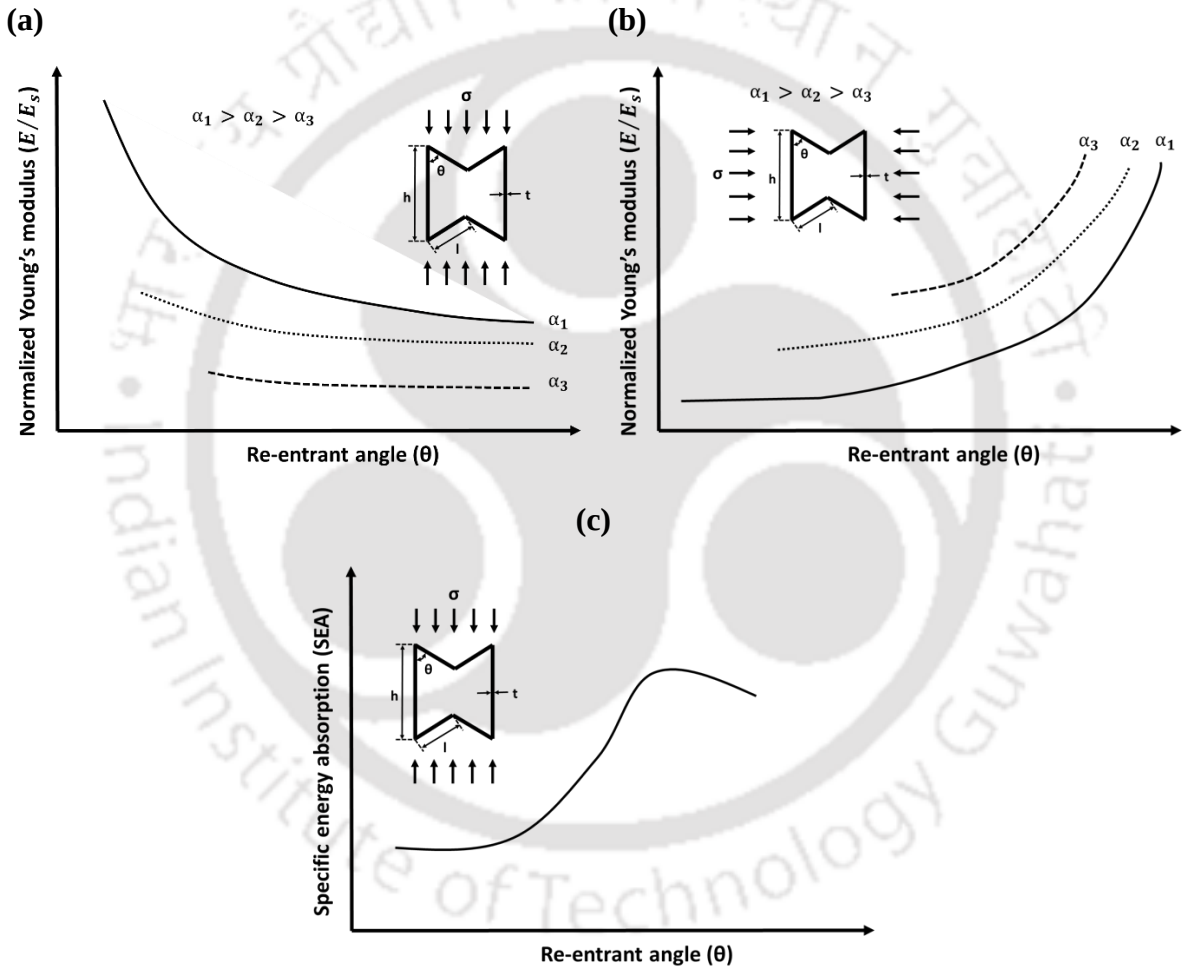

Fig. 1.5 Geometric tailoring: (a) effect of re-entrant angle (θ) & α on the normalized Young's modulus of the re-entrant lattices loaded parallel to the straight ligament, (b) effect of re-entrant angle (θ) & α on the normalized Young's modulus of the re-entrant lattices loaded perpendicular to the straight ligament and (c) effect of re-entrant angle (θ) on the SEA of the re-entrant lattices loaded parallel to the straight ligament

Fig. 1.5(c) shows a relation between the specific energy absorption of re-entrant lattices to the corresponding re-entrant angles for a given value of α and t. At a lower value of θ, the

cell of lattices collapsed very early due to easy contact of the opposite inclined members, leaving behind a porous deformed layer, leading to lower energy absorption with an early onset of densification strain. As the re-entrant angle increased, its specific energy absorption increased and became the maximum near the re-entrant angle of 60°; thereafter a drop in the specific energy absorption capacity of the lattices was observed.

Another way of developing higher energy absorption capacity re-entrant lattices is by introducing lower node connectivity joints. These lower node connectivity joints further improve the bending-dominated deformation mode leading to a higher energy absorption capacity of the developed re-entrant lattice. Higher node connectivity joints restrict the movement of inclined ligaments near the joints while lower node connectivity joints allow easy rotation near the joint due to the lower rotational stiffness of the joint. Local deformation takes place due to the presence of these lower node connectivity joints, which improves the onset of densification strain and hence the energy absorption capacity of the developed re-entrant lattices.

In the ligament addition method, straight, zigzag or curved ribs are added parallel or perpendicular to the straight ligaments [41, 43, 44] (Fig. 1.4(c) & Fig. 1.4(d)). The addition of ligaments strongly influences the stiffness of the re-entrant structure and can double it [45]. Ligament addition to the re-entrant structures generally changes the deformation pattern (bending dominated deformation pattern to stretching dominated deformation pattern) [46], and reduces the auxecity of the re-entrant structure. The added ligament restricts the lateral movement of the cell, and hence reduction in their transverse strain which leads to a reduction in auxecity of the structure. Structures show more stretching-dominated deformation behavior when ribs are added perpendicular to the straight ligaments than when they are added parallel to the straight ligaments. For the same relative density, the ligament addition improves the stiffness of the structure but reduces energy absorption capacity due to the formation of the soft post-yield response of the structure [47]. It can be concluded that due to ligament addition, there is an improvement in the stiffness of the re-entrant structure at the cost of auxecity and energy absorption capacity. The energy absorption capacity of the structure can be further improved by adding a lower wall thickness ligaments [25, 48]. These lower wall thickness ligaments introducing a local buckling effect which lead to higher energy absorption of the lattices [45, 49].

The combined method simultaneously improves the stiffness and energy absorption capability of the lattices. In this method, ligaments are added selectively, i.e. ligaments are

added at higher node connectivity joints at the direction of loading only while lower node connectivity joints keep it as it is. Due to the selective addition of ligaments, there is an enhancement in the stiffness and specific energy absorption (SEA) up to 3.55 and 1.65 times, respectively. Further improvement in stiffness and SEA (~4.5 and ~3.5 times, respectively) was achieved by increasing the thickness of the added ligaments marginally.

1.2.2.3 Auxetic cementitious Composite

In recent years, the overall performance of concrete is improved by reinforcing the different types of lattices in it. Researchers have explored usages of 3D printed reinforcement in concrete casting [50] and found that tunable surface roughness enabled by 3D printing process can lead to improved bonding between the reinforcement and the cementitious matrix. These lattice-reinforced cementitious composite (LRCC) has high-strength to weight ratio, high stiffness-to-weight ratio and superior energy absorption capacity than conventional concrete. Due to advancements in 3D printing technology, highly complex design is now feasible to fabricate [51] which leads research focus toward the LRCC materials [52][53]. Different lattices have been designed either by getting inspiration from nature or by self-realization to improve the mechanical performance of lattices. It has been observed that the properties of these lattices highly depend on the geometry of the lattice and can be tailored by tailoring its geometry [54][55][56]. Compared with metal printing, polymer printing is more accessible and economical with good print quality, leading to more research on polymeric printed reinforcement . Here, lattices are made from polymer is considered as reinforcement, while the concrete is considered a matrix. Due to reinforcement in concrete, the load-bearing capacity of concrete composite is increased by many folds. The performance of concrete composites under bending is improved due to the mitigation of concentrated loads and crack deflection.

1.3 Research gap and Motivation

Auxetic structures exhibit exceptional properties due to their unique architectural design; such as higher specific stiffness, higher compressive strength, higher specific energy absorption ability, higher impact resistance, enhanced indentation resistance, enhanced fracture toughness, etc.; and can be tailored by changing their design parameters to suit the required application. Numerous studies have attempted to improve the in-plane mechanical response of auxetic lattices specifically elastic modulus, compressive strength and energy absorption ability.

Nonetheless, a very few studies focused on simultaneous improvement of multiple mechanical properties. This gap set the stage for the present work. Design and fabrication of auxetic structures exhibiting high energy absorption, stiffness and compressive strength is a challenging task. Further, an in-depth analysis of design parameters is required and topology-properties correlation of the structure must be established. This requires a holistic design approach to fabricate novel auxetic structures that can fulfill the multi-functional requirement.

1.4 Objectives and scopes

The main objective of this research work is to understand and improve the stiffness and energy absorption characteristics of the auxetic structures used for engineering application. The major work modules involved are:

1. To investigate the energy absorption characteristics of existing auxetic re-entrant honeycomb structures influenced by geometrical parameters.
2. To design and 3D print new auxetic re-entrant structures exhibiting high energy absorption capability via geometry tailoring.
3. To study the influence of geometrical parameters and node connectivity on stiffness, strength, Poisson's ratio, and energy absorption properties.
4. To design and print new auxetic re-entrant structures exhibiting high energy absorption and stiffness.
5. To study the influence of tessellation on mechanical properties of auxetic re-entrant structures
6. To investigate the crushing performance of auxetic reinforced cementitious-polymer composites

The scope of the work is as follows:

1. The numerical model was developed and experimentally validated, and used for analysis of the results.
2. Theoretical models were also developed.
7. Additive manufacturing techniques (Fused Deposition Modelling) were used to fabricate auxetic re-entrant structure samples of desired shape and size for experimental purposes. However, a conventional manufacturing technique (casting) was used to fabricate the auxetic reinforced cementitious-polymer composites.

1.5 Thesis organization

This thesis consists of 7 chapters. Chapter 1 includes a general introduction and literature review about auxetic re-entrant structures under quasi-static loading condition, and discusses the objectives, scope, and organization of the thesis. While Chapter 2 discusses the materials and methods (experimental and numerical) used in this study. Chapter 3 introduces novel re-entrant structure exhibiting higher energy absorption than conventional re-entrant design. Chapter 4 introduces new auxetic structures exhibiting higher energy absorption and stiffness. Chapter 5 includes the study of tessellation influence on mechanical properties of the re-entrant structure through numerical modeling and experiments. In Chapter 6, crushing performance of auxetic reinforced cementitious composites is studied using the developed 3D printed auxetic structures. The final conclusion is presented in Chapter 7.

Chapter 2 Materials and methods

This chapter deals with materials that are used for the fabrication of 3D printed auxetic structures and lattice-reinforced concrete composites. It discusses the numerical modeling of auxetic structures and their mechanical testing methods. [1]

[1]A portion of this chapter has been published in:

1. Choudhry, N. K., Panda, B., & Kumar, S. (2022). In-plane energy absorption characteristics of a modified re-entrant auxetic structure fabricated via 3D printing. Composites Part B: Engineering, 228, 109437.

2. Nguyen-Van, V., Choudhry, N. K., Panda, B., Nguyen-Xuan, H., & Tran, P. (2022). Performance of concrete beam reinforced with 3D printed Bioinspired primitive scaffold subjected to three-point bending. Automation in Construction, 134, 104060.

3. Choudhry, N. K., Panda B, Kumar S. Enhanced energy absorption performance of 3D printed 2D auxetic lattices. Thin-Walled Struct 2023;186:110650. https://doi.org/10.1016/j.tws.2023.110650.

2.1 Introduction

This chapter provides a brief overview of material and experimental methods used in this study, which is divided into three categories: 1) raw materials required for both polymer lattice and cementitious material mix design 2) additive manufacturing method and casting process to produce lattice structure and auxetic reinforced concrete composite respectively and 3) list of experimental methods to obtain compressive characteristics. Detail regarding finite element based numerical modelling is presented in the last section of this chapter which includes model testing, validation and model derived mechanical properties.

2.2 Materials

All lattice structures are fabricated from commercially available acrylonitrile butadiene styrene (ABS) polymer through fused filament fabrication 3D printing method. Further, cementitious composites are formed by reinforcing the 3D printed auxetic lattice structures into the concrete. In this section, material behavior is evaluated.

2.2.1 Acrylonitrile butadiene styrene (ABS)

Commercially available acrylonitrile butadiene styrene (ABS) polymer filament was used to fabricate the lattice structures. The test samples were printed by using the same printing condition as that of the lattice structures through the fused filament fabrication 3D printing method.

Uniaxial tensile test was performed on 3 identical dogbone samples having a gauge length of 25mm, width 6mm and thickness 2mm on a Zwick-Roell UTM having 5kN load cell. Three samples were tested to get reliable and repeatable results. The dogbone samples were placed in the grip of the UTM and the tensile load was applied with a crosshead speed of 2mm/min till samples failed. Each test was recorded by using a high-definition digital camera. The stress-strain response of specimens was calculated from load-displacement data. Fig. 2.1(a) represents the average stress-strain response of 3D printed all three dogbone samples during tension. The elastic properties of ABS polymer are given in Table 2.1.

Three identical cuboidal samples having an edge length of 12.7mm and 25.4mm height were fabricated with ABS polymer. A quasi-static compression test was performed with a Zwick-Roell UTM having a 5kN load cell at the crosshead speed of 2 mm/min. The samples were loaded in between the top and bottom platens and the deformation maps were recorded using a high-definition digital camera. Crushing forces were recorded through a 5 kN load cell.

Fig. 2.1(b) represents the average stress-strain response of 3D printed all three cuboidal samples during compression.

Table 2.1 Elastic properties of 3D printed ABS specimen.

Material	Elastic modulus (MPa)	Yield stress (MPa)	Poisson's ratio	Density (g/cm^3)
ABS	2000	29	0.35	1.05

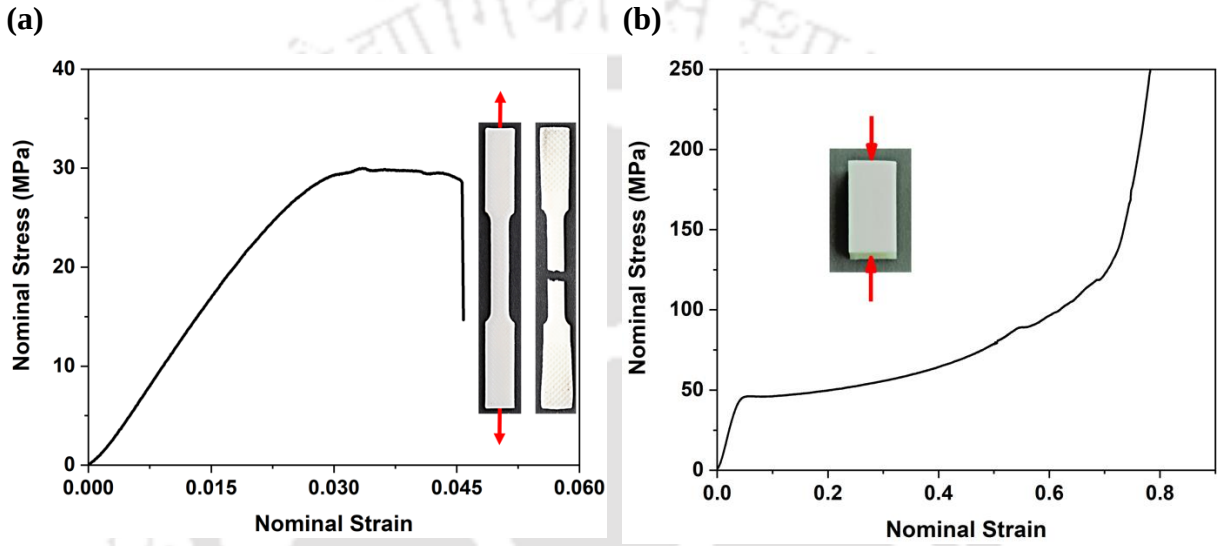

Fig. 2.1 Stress-strain representation of bulk specimen: (a) Tensile response of 3D printed dogbone sample and (b) Compressive response of 3D printed cuboidal sample.

2.2.2 Concrete properties

The properties of cementitious mortar were found by casting a homogeneous mortar within three identical cubical samples (50 mm × 50 mm × 50 mm). For preparing the mortar, Ordinary Portland Cement (OPC), class F fly ash and sand were taken in a given proportion (see Table 2.2) and dry mixed for 5 minutes in a Hobart planetary mixer. Polycarboxylate Ether (PCE) admixture was mixed with tap water, and added into the dry mix followed by high-speed mixing for 3 minutes to obtain a homogeneous cementitious mortar. The mortar was poured into the cubical mold. The mold was vibrated to ensure proper filling of mortar without any air bubbles. Cubical samples were demolded after 1 day of casting and cured for 28 days in a moist environment.

Table 2.2 Mix proportion of cementitious mortar

Materials	Mix Design in kg/m^3
Ordinary Portland Cement (OPC)	550
Fly ash Class F	650
Water	348
Sand	1200
PCE admixture	3.7

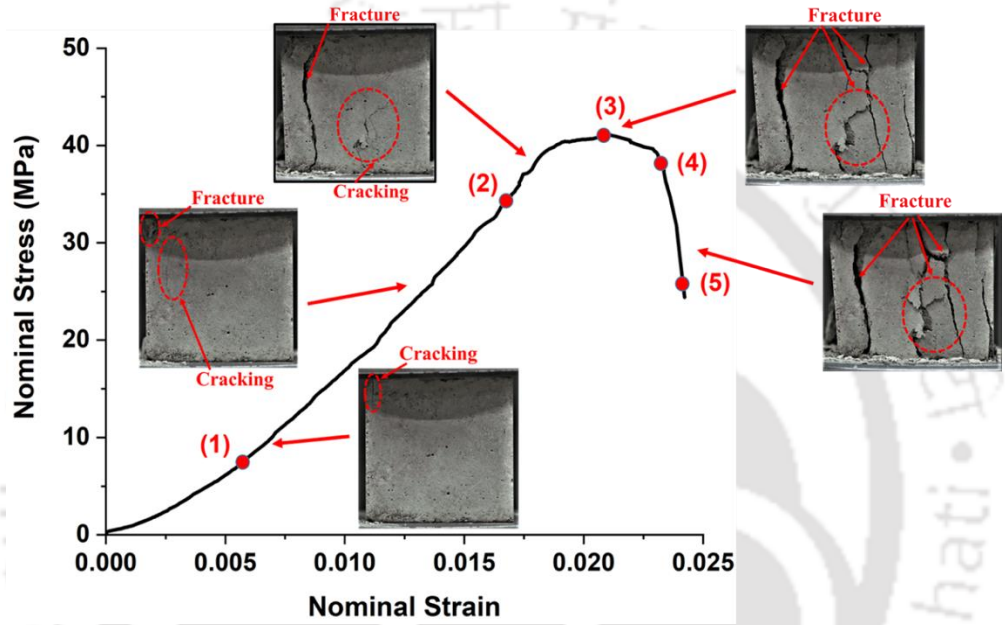

Fig. 2.2 Stress-strain response and failure patterns of a concrete sample under quasi-static compression

Table 2.3 Mechanical properties of mortar

Dimension (mm)	Compressive Strength (MPa)	Young's modulus, E (MPa)	Density, ρ (kg/m^3)	Poisson's Ratio, ν
50x50x50	41.26	1632.98	2080	0.2

A quasi-static compression test was conducted at room temperature by using the 250 kN UTM (MEDIAN 250). A constant displacement control method was used where the rate of displacement was 2mm/min. The samples were loaded in between the top and bottom platens and the deformation maps were recorded using a high-definition digital camera. Crushing forces were recorded through a 250 kN load cell. The average nominal stress-strain response of these concrete samples was calculated from the experimental load-displacement data and is

presented in Fig. 2.2 with a sequential deformation pattern. The mechanical properties of mortar are given in Table 2.3.

2.3 Additive manufacturing

The lattice structures were fabricated using a FDM printer (AEQON 400 V3 make of DIVIDE BY ZERO). ABS filament (1.75mm diameter) was extruded through a hot nozzle (240° extrusion temperature) having a diameter of 0.4mm to fabricate lattices by a layer-by-layer deposition technique. "X" and "Y" directions were chosen as printing directions while the "Z" direction was considered the build direction in this study to minimize the time required and material being used (no support material required) for printing the structure. Fig. 2.3 demonstrates a schematic representation of the FDM printing process, where different directions have been highlighted. The printing parameters used for the fabrication of lattices are given in Table 2.4.

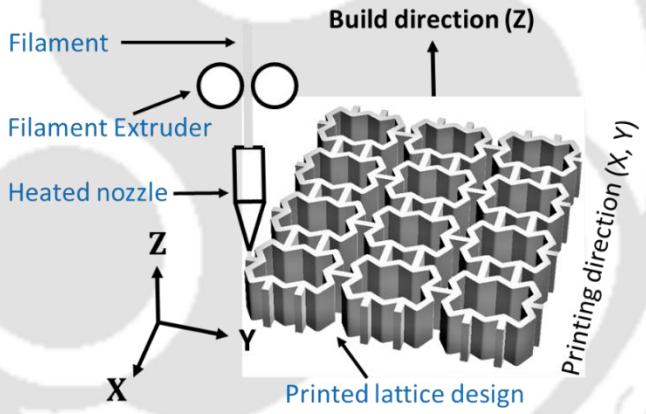

Fig. 2.3 Schematic representation of the FDM printing process

Table 2.4 Printing parameters used for the fabrication of lattices

Printing speed (mm/s)	Layer thickness (mm)	Infill density (%)	Raster angle (°)	Extruder temperature (°C)	Bed temperature (°C)
50	0.2	100	±45	240	90

2.4 Experimental methods

2.4.1 Uniaxial compression testing

In order to evaluate the mechanical response, quasi-static compression tests were performed at room temperature on the 3D-printed auxetic structures. The testing was carried

out using 250 kN UTM (MEDIAN 250) at the crosshead speed of 2 mm/min [57]. The 250 kN load cell has an accuracy of ≤ ±1% of its output reading. The samples were loaded in Y-direction and the deformation maps were recorded using a high-definition digital camera. Crushing forces were recorded via a sensor, attached to the loading plate. Load-displacement data, generated during the compression test were recorded and used for further analysis. Three samples for each model were tested to get reliable and repeatable results.

Fig. 2.4 shows the experimental setup used for quasi-static compression test. The components of 250 kN UTM (MEDIAN 250) are highlighted in Fig. 2.4. The top platen is connected to the load cell which is mounted on a crosshead. The crosshead is mounted on the column, and its position is fixed before the start of a compression test. Here top platen is fixed and movement is given to the bottom platen. Compression test is performed at room temperature and recorded using Sony NXCAM Video Camera. For any emergency condition, the emergency stop button can be used.

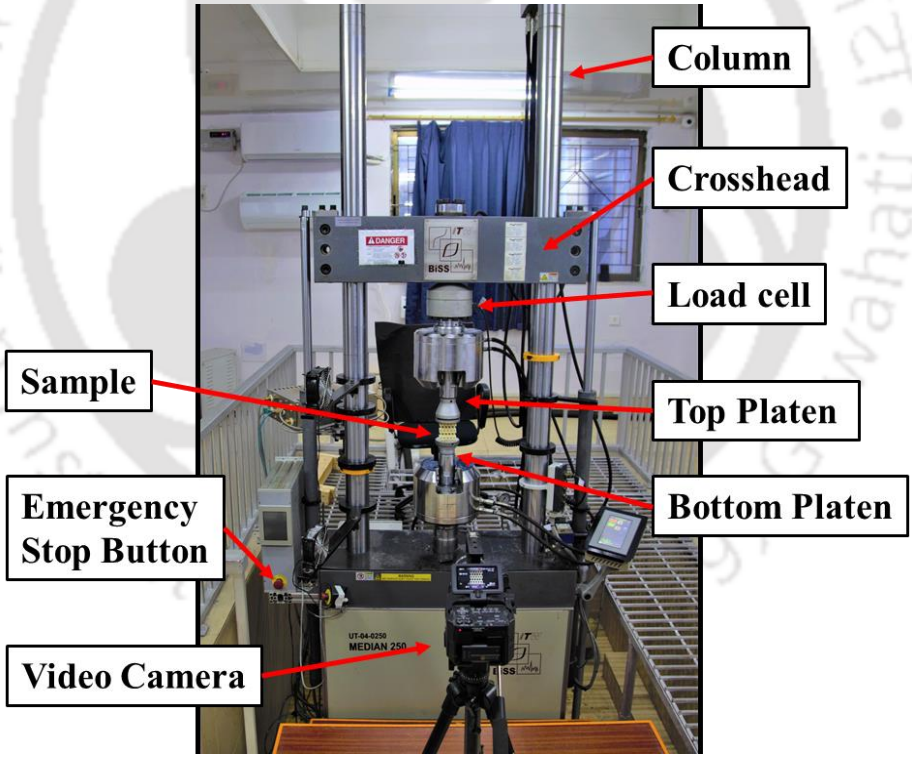

Fig. 2.4 Experimental setup for quasi-static compression test

2.4.2 Optical microscope

Optical images were taken from an optical microscope (make- Carl Zeiss) as shown in Fig. 2.5(a) with a 10x magnification at different locations of the FDM printed part. Samples have been prepared by polishing the 3D printed part on a variable speed single disc polishing

machine (make- Chennai Mecto) as shown in Fig. 2.5(b). First rough polishing was performed to remove the strings that is formed during the printing. Thereafter fine polishing was performed, and polished samples were used for getting the optical images. Emery paper with grades of 220 and 400 was used for rough and fine polishing respectively.

(a) **(b)**

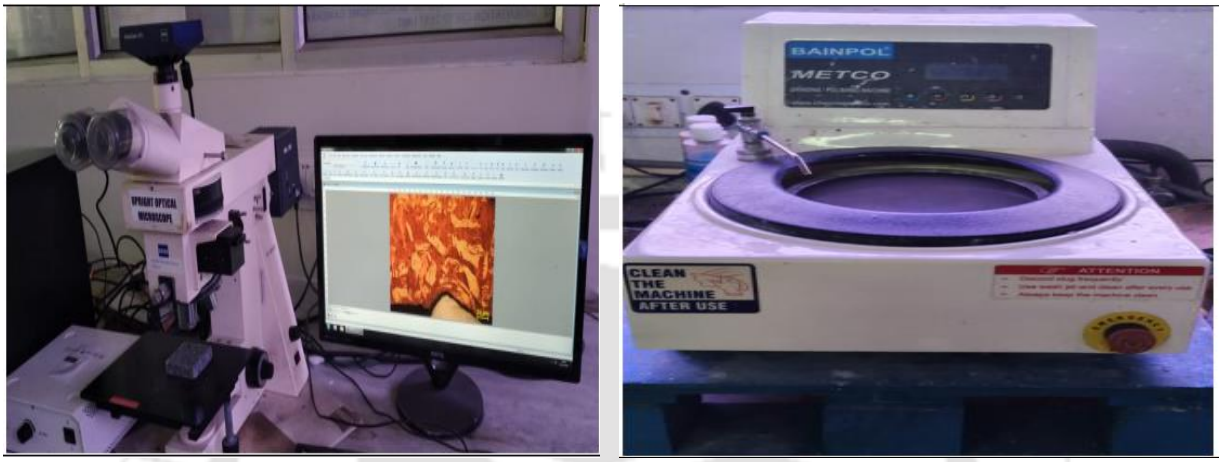

Fig. 2.5 (a) Optical microscope and (b) variable speed single disc polishing machine

2.5 Finite element (FE) analysis

For systematically analyzing the quasi-static compression response of 3D printed auxetic structures, FE analysis was conducted using a commercial FE package (ABAQUS) with a nonlinear explicit solver. Discrete rigid elements were assigned for top and bottom platens to simulate the moving and stationary platens, respectively. The top platen was given downward motion by allowing a single degree of freedom while all degrees of freedom for the bottom platen were constrained. Fig. 2.6 shows a typical FE mesh of the re-entrant honeycomb structure with appropriate loading and boundary conditions.

Acrylonitrile butadiene styrene (ABS) polymer exhibited significantly different yield behavior in tension and compression (section 2.1.1 (Fig. 2.1)), and hence a pressure-dependent plasticity model was used to model the material behavior. Isotropic elasticity was considered for modeling the elastic behavior while plastic behavior was modeled by using the Linear Drucker-Prager plasticity model. The ductile damage model was considered for modeling the material failure. “Explicit dynamic” analysis was performed considering geometric, material and contact non-linearities. The elastic properties of the ABS material used in the FE analysis are summarized in Table 2.1 while the plastic and failure behavior is provided in section 2.4.1.

All the calculations were performed in ABAQUS/Explicit with a sufficiently low displacement rate (500 mm/s) to eliminate inertial effects (refer to section 2.4.2) and ensure quasi-static deformation. Contact between rigid plates and the surfaces of models is defined as a 'general contact interaction' while 'self contact is considered in between the surfaces of the structure. Contact with a friction coefficient of 0.3 was set in the tangential direction and hard contact was considered in the normal direction [58]. An 8-node hexahedral (C3D8R) [59] element with a 0.3 mm mesh size (refer to section 2.4.3) was used for meshing the structures and a 4-node linear quadrilateral (R3D4) element with a 2 mm mesh size was used for the top & bottom rigid plates. The analysis was performed up to a nominal compressive strain of 80% (as in the experiments), and the obtained force vs displacement profiles are used to determine the stress vs strain responses as well as the energy absorption capacities of the structures.

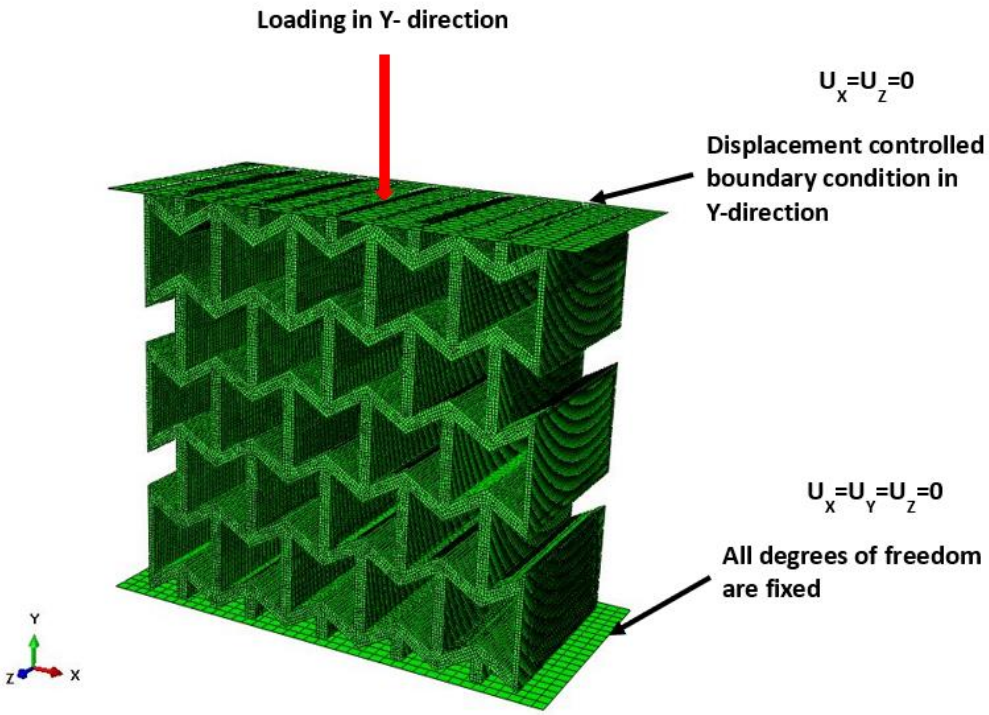

Fig. 2.6 FE model with boundary conditions of re-entrant honeycomb structure for quasi-static compression test

2.5.1 Constitutive models

ABS polymer exhibited significantly different yield behavior in tension and compression, and hence a pressure-dependent plasticity model was used to model the material behavior. Isotropic elasticity was considered for modeling the elastic behavior of ABS polymer while

plastic behavior was modeled by using the Linear Drucker-Prager plasticity model. The Ductile Damage Model was considered for modeling material failure.

The model decomposes the total strain rate into two parts one is elastic strain rate while the other is plastic strain rate as given below (equation 2.1)

$$\dot{\boldsymbol{\epsilon}} = \dot{\boldsymbol{\epsilon}}^e + \dot{\boldsymbol{\epsilon}}^p \tag{2.1}$$

Where $\dot{\boldsymbol{\epsilon}}$ is the total strain rate while $\dot{\boldsymbol{\epsilon}}^e$ and $\dot{\boldsymbol{\epsilon}}^p$ are the elastic and plastic components of the total strain rate respectively. The stress-strain relationship by employing scalar damage elasticity can be written as (equation 2.2)

$$\boldsymbol{\sigma} = \boldsymbol{D}^e : (\boldsymbol{\epsilon} - \boldsymbol{\epsilon}^p) \tag{2.2}$$

where $\boldsymbol{D}^e$ is degraded elastic stiffness tensor which relates with undegraded elastic stiffness $\boldsymbol{D}_0^e$ as (equation 2.3)

$$\boldsymbol{D}^e = (1 - d)\boldsymbol{D}_0^e \tag{2.3}$$

d is known as a scalar elastic damage variable having a value between 0 and 1. When $d = 0$, it means the material is undamaged while at $D = 1$, the material is completely ruptured (the load-carrying capacity of material has been lost). Considering the degradation of the material is due to the growth of microcracks and voids, and hence having reduced resistance area. So the effective stress can be represented as (equation 2.4)

$$\overline{\boldsymbol{\sigma}} = \frac{\boldsymbol{\sigma}}{(1-\mathrm{d})} = \boldsymbol{D}_0^e : (\boldsymbol{\epsilon} - \boldsymbol{\epsilon}^p) \tag{2.4}$$

Which is used for formulating the plasticity behavior.

Yield surface evolution is controlled by employing isotropic hardening variables in the form of equivalent plastic strains for both tension ($\tilde{\epsilon}_t^p$) and compression ($\tilde{\epsilon}_c^p$), and can be expressed in rate form as given in equation 2.5 which is derived from equation 2.6

$$\dot{\tilde{\boldsymbol{\epsilon}}}^p = \boldsymbol{h}(\overline{\boldsymbol{\sigma}}, \tilde{\boldsymbol{\epsilon}}^p).\dot{\boldsymbol{\epsilon}}^p \tag{2.5}$$

Where

$$\tilde{\boldsymbol{\epsilon}}^p = \begin{bmatrix} \tilde{\epsilon}_t^p \\ \tilde{\epsilon}_c^p \end{bmatrix} \tag{2.6}$$

The yield function for Drucker-Prager model is written as (equation 2.7)

$$F(\overline{\boldsymbol{\sigma}}, \tilde{\boldsymbol{\epsilon}}^p) \leq 0 \tag{2.7}$$

The non-associated flow rule can be given as (equation 2.8)

$$\dot{\boldsymbol{\epsilon}}^p = \dot{\lambda}\frac{\partial G(\overline{\boldsymbol{\sigma}})}{\partial \overline{\boldsymbol{\sigma}}} \tag{2.8}$$

where $\dot{\lambda}$ and $\frac{\partial G(\overline{\boldsymbol{\sigma}})}{\partial \overline{\boldsymbol{\sigma}}}$ are the non-negative plastic multiplier and the normal vector to the plastic flow potential surface $G(\overline{\boldsymbol{\sigma}})$ respectively. Table 2.5 shows the parameters used in

ABAQUS to apply the Linear Drucker-Prager plasticity model to capture the plastic behavior of ABS material and Table 2.6 for the capturing of failure of the material.

Table 2.5 Linear Drucker-Prager plasticity parameters with Isotropic hardening in uniaxial tension for ABS polymer

Angle of Friction (β)	Flow Stress Ratio	Dilation Angle (ψ)
12^0	0.8216	12^0

Table 2.6 Ductile Damage Model parameters for ABS polymer

Fracture Strain	Stress Triaxiality	Strain Rate (1/s)	Fracture Energy (N/mm)
0.625	- 0.33	0.00133	0.27
0.008	0.33	0.00133	0.27

2.5.2 Loading speed

The quasi-static compression test numerically requires a very large CPU time that can be reduced by using an increasing loading rate, but the inertia effect should be negligible. The test was performed with four different loading speed (as shown in Fig. 2.7) and kinetic energy (KE) and internal energy (IE) of the structure during compression was plotted. It's clear from Fig. 2.7 that at high speed (5000 mm/s) the effect of inertia is high and it reduces as we reduce loading speed and becomes insignificant at 500 mm/s. In this research, a velocity of 500 mm/s was used to reduce computational time with no inertia effect.

2.5.3 Mess sensitivity analysis

Fig. 2.8 represents a mesh convergence study where both the elastic and plastic behavior of the re-entrant honeycomb (RH) structure was considered. A load-displacement curve is drawn for different mesh element sizes. For a coarser mesh size, the prediction of structural performance was not appropriate, but as mesh element size is refined or reduced, the accuracy of results increases and becomes stable. It can be seen from Fig. 2.8 that a large mesh size (0.6 mm) system over predicted the result. As mesh size reduces, its accuracy increases, and after (0.4 mm) the size effect is vanishing. At mesh sizes of 0.4 mm and 0.3 mm, the results are the same. In this research, a mesh of 0.3 mm is used to nullify the mesh size effect.

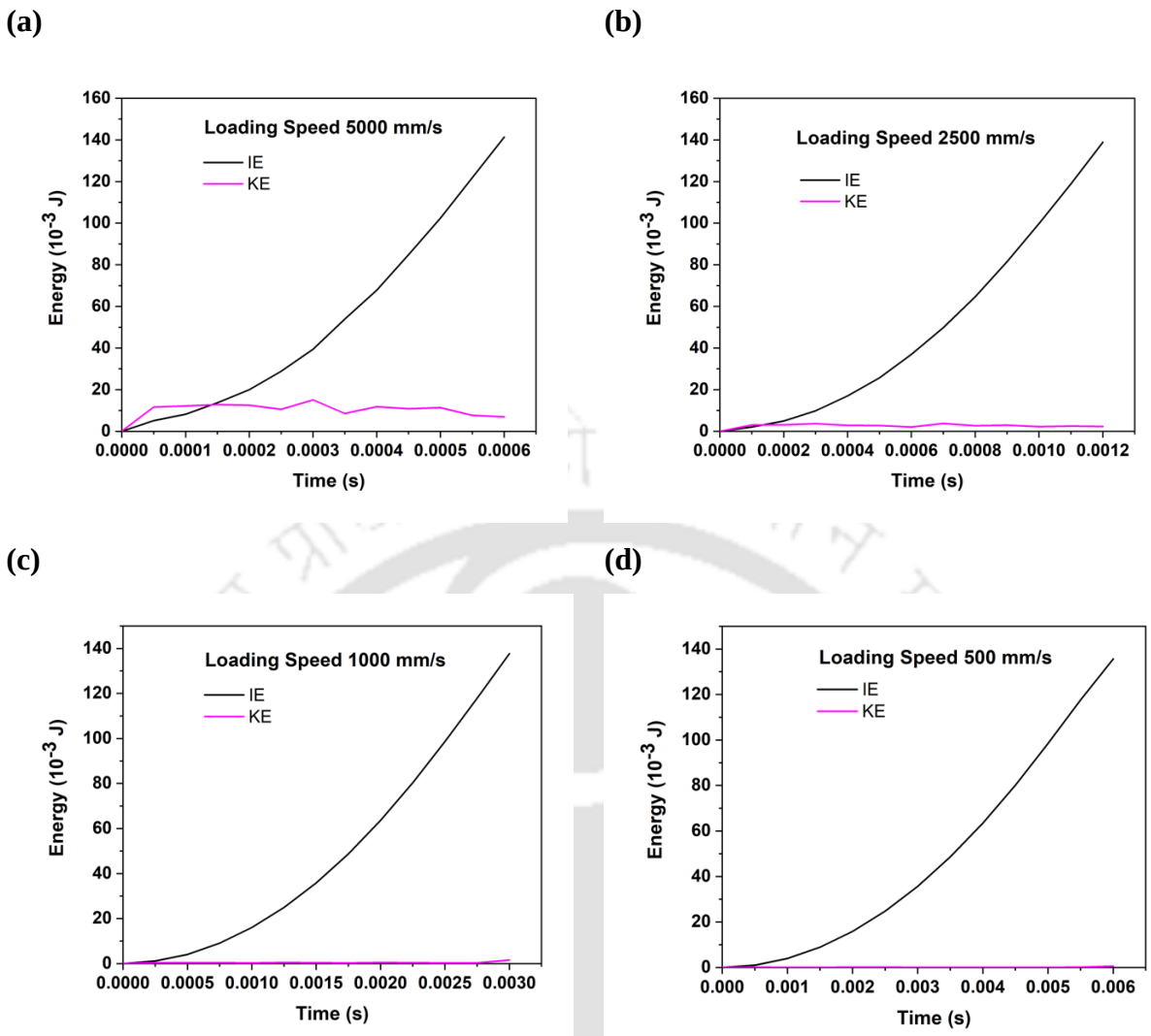

Fig. 2.7 Effect of loading speed on kinetic energy (KE) and internal energy (IE) of the structure during compression; (a) loading speed 5000 mm/s, (b) loading speed 2500 mm/s, (c) loading speed 1000 mm/s and (d) loading speed 500 mm/s

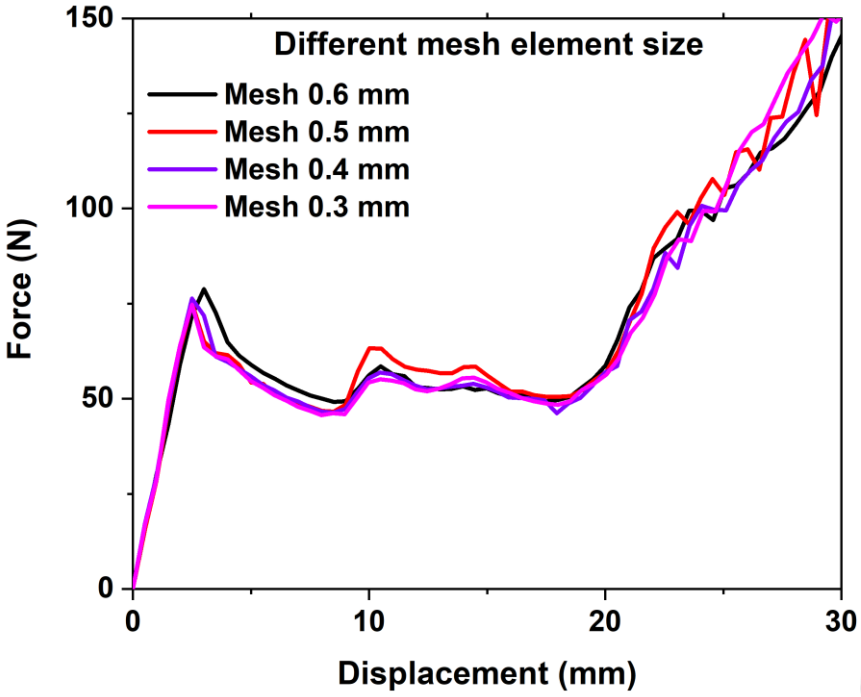

Fig. 2.8 Force-displacement curve at different mesh element sizes

2.5.4 Numerical model validation

The finite element model developed in this work was validated by comparing the FE predictions with the experimentally measured stress-strain response and their sequential deformation configuration during quasi-static compression for the optimal structure shown in Fig. 2.9. It is clear from the figure that the numerical model is capable of predicting both the elastic and plastic behavior (with three distinct stages) as discussed by many researchers [35, 60]. In the beginning, a linear elastic response is observed followed by a plateau regime and finally the densification regime. In summary, the FE prediction is in good agreement with the experimental results.

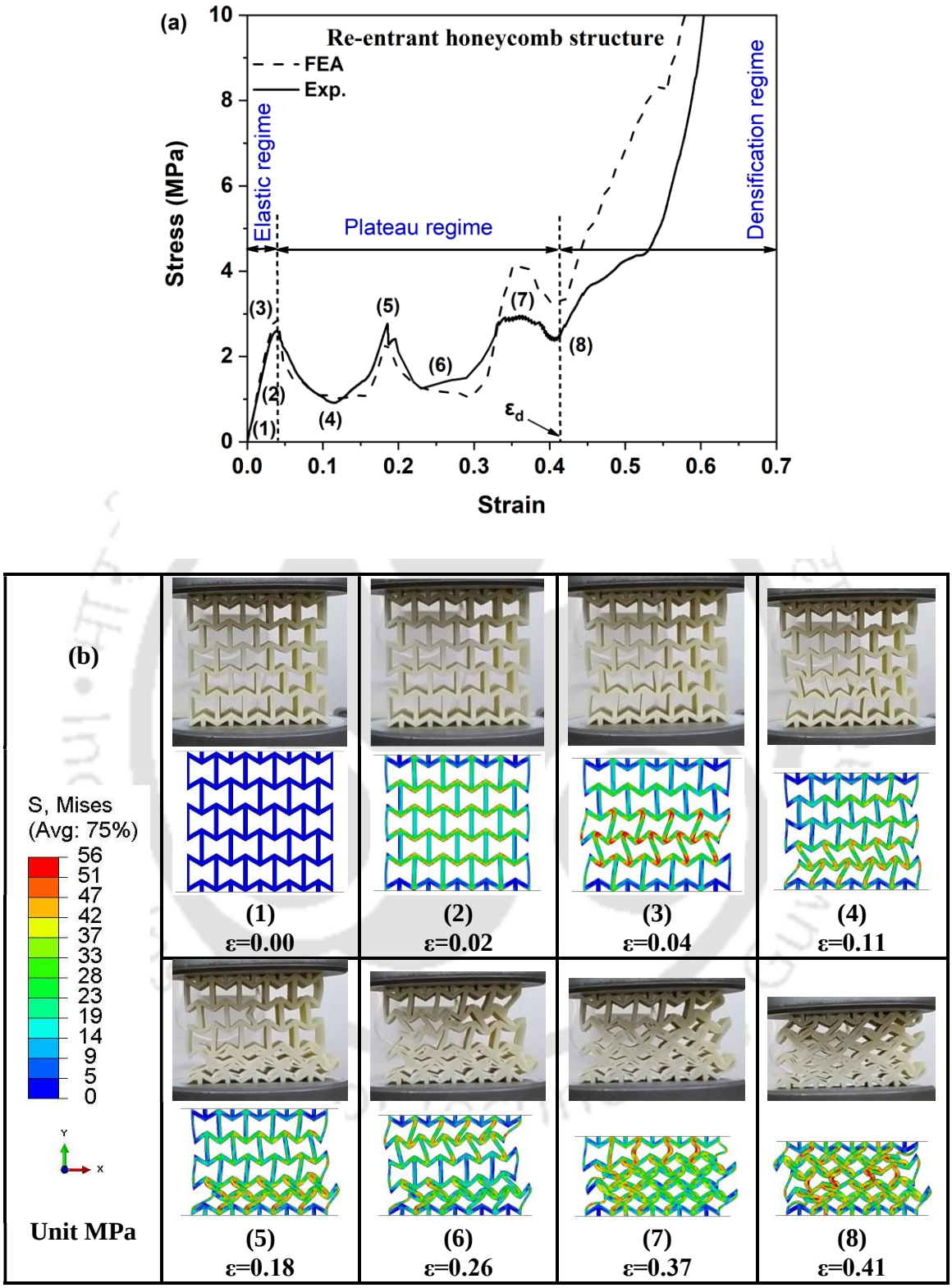

Fig. 2.9 Comparison of numerical and experimental result of re-entrant honeycomb (RH) structure; (a) stress-strain curve and (b) sequential deformation configuration during quasi-static compression at the corresponding points shown in the stress-strain curve

2.6 Lattice structure properties

In this section, different properties evaluation methods have been discussed. These properties are derived from the results obtained from the experiments.

2.6.1 Relative density

The theoretical relative density of an auxetic lattice structure is defined as the ratio of the area occupied by the cell wall of the unit cell to the area occupied by the unit cell [61]. The relative density of the fabricated cellular structures are obtained using equation 2.9.

$$\bar{\rho} = \left(\frac{\rho}{\rho_s}\right) \tag{2.9}$$

where ρ and ρ_s represent the density of the cellular structure and density of the base material respectively.

2.6.2 Nominal stress-strain

After performing the quasi-static compression test on auxetic lattice structures, the load-displacement response was generated and recorded. Three samples for each structure were tested, and their average load-displacement response was used for further analysis. The nominal stress (σ) and nominal strain (ε) were calculated from the load-displacement response using equation (2.10) and equation (2.11) respectively.

$$\sigma = \frac{F}{W \times L} \tag{2.10}$$

$$\varepsilon = \frac{\delta}{\mathrm{H}} \tag{2.11}$$

where δ is the displacement due to applied compressive load F ; H , W and L are the height, width and thickness (out of plane) of the structure respectively.

2.6.3 Young's modulus, yield strength and compressive strength

Young's modulus, yield stress and compressive strength are calculated from the nominal stress-strain curve. The slope of the nominal stress-strain curve within the elastic regime gives Young's modulus of the lattice structure while the peak of the elastic regime after which lattices start deforming plastically is identified as the yield strength of the lattice structure. Compressive strength determines the load-bearing capacity of a lattice structure, and it is the maximum stress a lattice structure can resist before reaching the onset of densification strain.

2.6.4 Energy absorption

The energy absorption capacity (in MJ/m^3) of any lattice structure is determined by the area under the stress-strain curve starting from the beginning and covering up to the onset of densification (equation 2.12).

$$Energy\ absorbed = \int_0^{\varepsilon_D} \sigma(\varepsilon) d\varepsilon \tag{2.12}$$

There are three different methods to identify the onset of densification (ε_D) [58] as presented in Fig. 2.10. The first method is used when there is a sharp rise in stress in stress-strain response while the second and third methods are used when there is no such sharp rise in stress in stress-strain response.

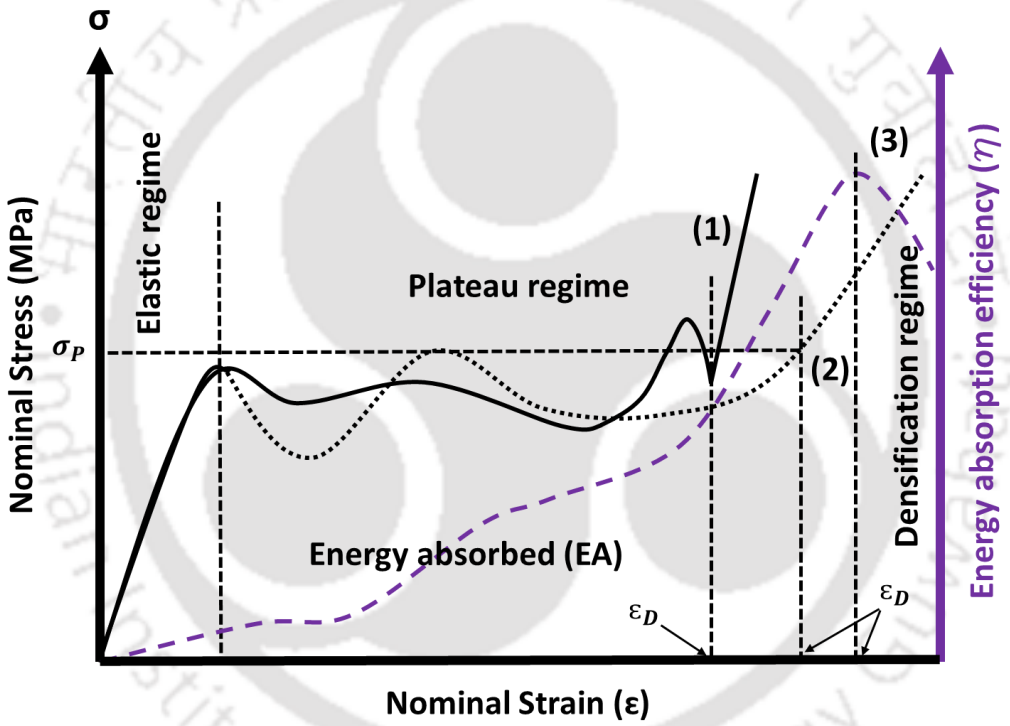

Fig. 2.10 different methods used to identify the onset of densification strain, and their corresponding energy absorption performance

In the first method, the onset of densification is identified by a point after which there is a sharp rise in stress value while in the second method, a line parallel to the strain axis is drawn from the peak stress (σ_P) which intersects the stress-strain curve, the corresponding intersecting strain is identified as the onset of densification. In the third method (efficiency method), energy absorption efficiency η is plotted against the strain, and the corresponding strain having the highest efficiency is identified as the onset of densification (equation 2.13).

The specific energy absorption (SEA), φ [34] and the energy absorption efficiency, η of the structures at the onset densification strain ε_D were calculated by using the equation (2.13) [62] and equation (2.14) [63] respectively.

$$\varphi = \frac{1}{\rho}\int_0^{\varepsilon_D} \sigma(\varepsilon)d\varepsilon \tag{2.13}$$

$$\eta = \frac{1}{\sigma_D}\int_0^{\varepsilon_D} \sigma(\varepsilon)d\varepsilon \tag{2.14}$$

Where σ represents the axial compressive stress of the structure experienced during quasi-static compression and ε is its work conjugate. ε_D and σ_D represents the densification strain and compressive strength (maximum stress a structure can resist before densification begins) of the structure respectively.

2.6.5 Poisson's ratio

Poisson's ratio (ν) deals with a material's distortion when it is subjected to a mechanical load. It is used to compare the structural performance of different materials (for both homogeneous and non-homogeneous) when they are elastically strained. It is the ratio of transverse (ε_t) to longitudinal strain (ε_l) (see, equation 2.15).

$$\nu = -\frac{\varepsilon_t}{\varepsilon_l} \tag{2.15}$$

However, a series of deformed images captured at different instants during loading were used to calculate the Poisson's ratio (ν) as a function of imposed strain (equation 3.16). A series of deformed images were taken for a given structure and an instantaneous change in displacement of traced nodes along the transverse and longitudinal direction was calculated. The longitudinal distance (Y) was the average distance of marked nodes between the top and bottom rows while the transverse distance (X) was the average distance of marked nodes between the left and right rows. The true longitudinal ($\varepsilon_{l\,true}$) and true transverse ($\varepsilon_{t\,true}$) strains were determined for the i^{th} image, where the preceding image $(i-1)^{th}$ was considered as reference. The Poisson's ratio (ν_{yx}) [64] for the loading direction Y was calculated from below equation-2.16.

$$\nu_{yx} = -\frac{\varepsilon_{t\,true}}{\varepsilon_{l\,true}} \tag{2.16}$$

Here, the method used for finding the true transverse ($\varepsilon_{t\,true}$) strain is demonstrated and a similar method can be used to find the true longitudinal ($\varepsilon_{l\,true}$) strain. Firstly, the average distance of marked nodes between the left and right rows for i^{th} image and preceding image (i-

1)th was calculated (equation 2.17 and equation 2.18 respectively) [65]. Fig. 2.11 shows a schematic representation of images for the calculation of average longitudinal and transverse distance.

$$X_i = \frac{AA_1+BB_1+CC_1+DD_1+EE_1+FF_1}{6} \tag{2.17}$$

$$X_{i-1} = \frac{AA_1+BB_1+CC_1+DD_1+EE_1+FF_1}{6} \tag{2.18}$$

Where, X_i and X_{i-1} are the average distance of marked nodes between the left and right rows for ith image and its preceding image (i-1)th respectively. The transverse displacement (ΔX) can find out by using equation 2.19, and finally the true transverse ($\varepsilon_{t\ true}$) strain was calculated by following equation 2.20 [64].

$$\Delta X = X_i - X_{i-1} \tag{2.19}$$

$$\varepsilon_{t\ true} = \frac{\Delta X}{X_{i-1}} \tag{2.20}$$

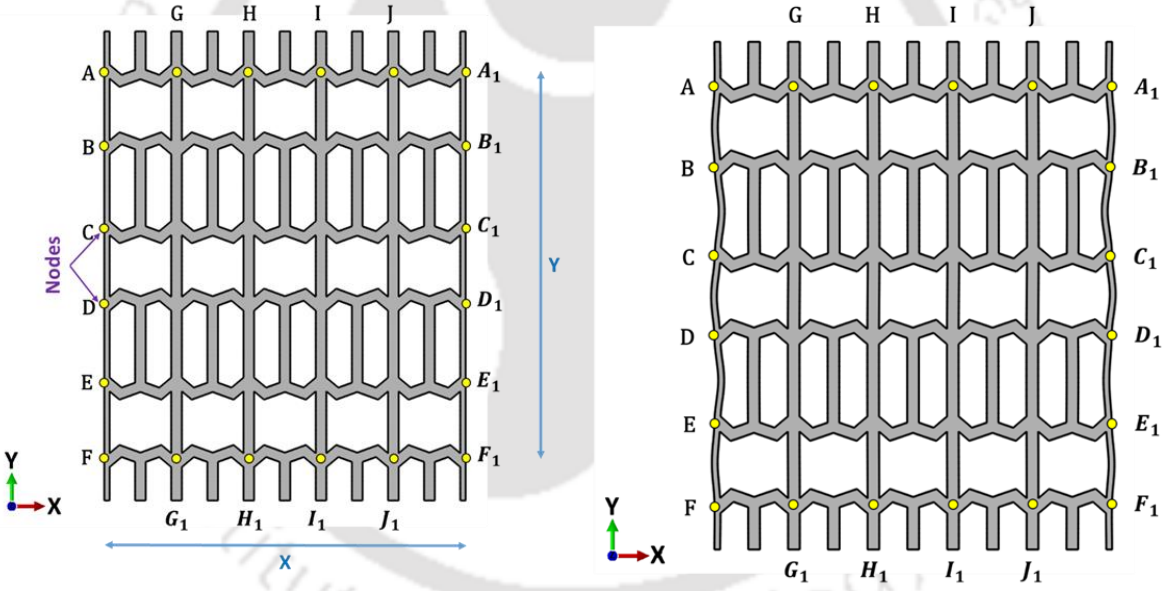

Preceding image (i-1)th Image ith

Fig. 2.11 Schematic representation of images for calculation of average longitudinal and transverse distance

Chapter 3 In-plane energy absorption characteristics of modified re-entrant auxetic structure fabricated via 3D printing

This chapter aims to enhance the energy absorption characteristics of a regular re-entrant honeycomb (RH) auxetic structure by means of introducing lower node connecting joints. The influence of geometrical parameters such as 'strut-length ratio' and 'joint angles' on the mechanical properties of the structure is studied through the response surface methodology (RSM) technique. Deformation mode, stress-strain curves and energy absorption characteristics of the optimized structure (Modified RH) are studied and compared with the RH structure. [1]

[1]A portion of this chapter has been published in:

Choudhry, N. K., Panda, B., & Kumar, S. (2022). In-plane energy absorption characteristics of a modified re-entrant auxetic structure fabricated via 3D printing. Composites Part B: Engineering, 228, 109437.

3.1 Introduction

Numerous studies have attempted to improve the in-plane mechanical response by designing new structures possessing enhanced energy absorption properties. Node connectivity (number of struts connected to a node/point) within the structure plays a key role in determining the deformation behavior and hence their mechanical response; the structures with higher node connectivity are more likely to deform in a stretch-dominated manner and therefore they are stiffer and weight efficient [66]. In this study, an auxetic lattice structure has been designed based on the node connectivity method for improved energy absorption properties. Here, modified re-entrant honeycomb structures were designed and realized via fused filament fabrication (FFF) additive manufacturing. The in-plane behavior of these structures was studied through quasi-static compression tests and results are further numerically analyzed and compared. The influence of geometrical parameters such as 'strut-length ratio' and 'joint-angles' on the mechanical properties of the structure is studied through the response surface methodology (RSM) technique. Numerical models were developed using ABAQUS/Explicit and benchmarked with the experimentally obtained results. Deformation mode, stress-strain curves and energy absorption characteristics of the optimized structure are studied and compared.

3.2 Auxetic structure design

A new design of the re-entrant auxetic structure is proposed in this study by modifying the regular re-entrant honeycomb geometry without changing the mass of the specimen. In order to enhance the energy absorption capacity through improved bend-dominated deformation, low rotational stiffness nodes are generated in the new design by splitting the inclined struts into two links in such a way that the sum of the link length is equal to the original inclined strut length. Fig. 3.1 shows the configuration of regular and modified re-entrant honeycomb structures.

The architectural parameters of the regular and modified re-entrant honeycomb structures are described as follows. In the re-entrant honeycomb structure, **h** represents vertical strut-length of 16mm while **l** represents inclined strut-length of 8 mm, **θ** represents the angle of an inclined strut to horizontal of 30^0 and **t** (2mm) represents the thickness of all struts. Similarly, in the modified structure, **h** represents vertical strut length, $\boldsymbol{\theta_1}$ indicates the inclination of strut

$\mathbf{l_1}$ to horizontal, $\mathbf{\theta_2}$ represents the angle between two inclined struts, **and t** indicates the thickness of all struts. $\mathbf{l_1}$ **and** $\mathbf{l_2}$ represent the lengths of two inclined struts.

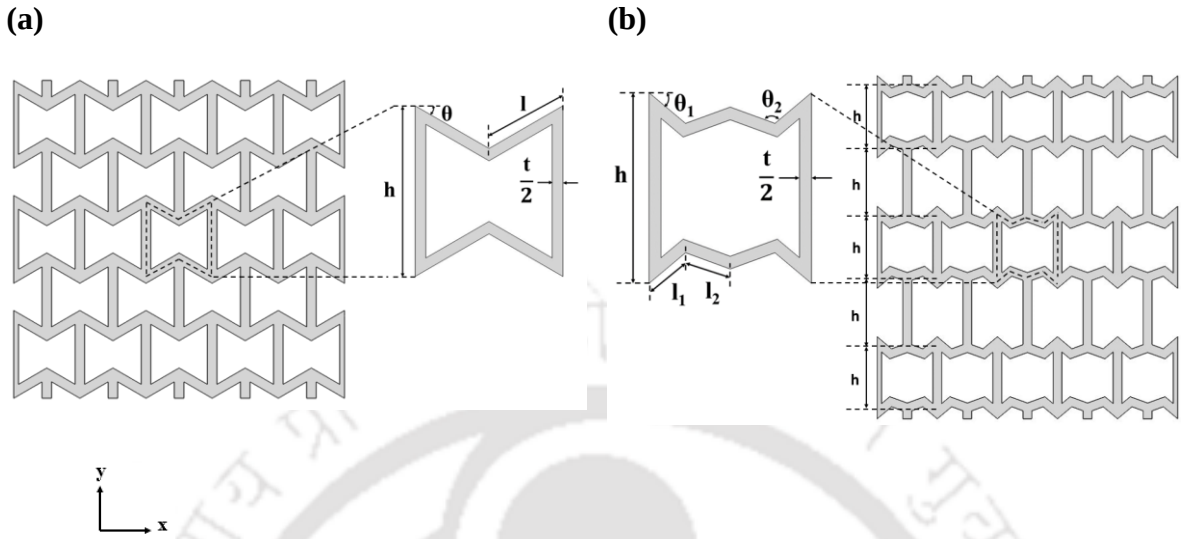

Fig. 3.1 CAD model with a representative unit cell of (a) regular re-entrant honeycomb structure and (b) Modified re-entrant honeycomb structure

For low relative densities, the relative density of both structures can be obtained from the geometry of the unit cell as follows:

The relative density of *regular re-entrant honeycomb* structure (equation 3.1)

$$\bar{\rho} = \frac{(2l+h)t}{2l\cos\theta\,(h-l\sin\theta)} \tag{3.1}$$

The relative density of *modified re-entrant honeycomb* structure (equation 3.2)

$$\bar{\rho} = \frac{2(l_1+l_2)+ht}{2\left[l_1^{\,2}\sin\theta_1\cos\theta_1 + l_2\cos(\theta_1+\theta_2)\{l_1\cos\theta_1\,(h-2l_1\sin\theta_1) + l_2\sin(\theta_1+\theta_2)\}\right]} \tag{3.2}$$

3.3 Geometrical tailoring and design of experiments

The geometrical tailoring of the modified re-entrant honeycomb structure is achieved by varying three variables namely, inclined strut-length ratio (l_1:l_2), θ_1 (deg.) and θ_2 (deg.) while maintaining constancy of mass of the structure. The maximum and minimum limits, as well as center points of these variables (Table 3.1), were chosen considering the design feasibility and printing limitations of the FFF 3D printer used in this study.

Table 3.1 Design variables with their levels

Variables	-1 (low)	0 (mid)	1 (high)
l_1:l_2	1	4	7
θ_1 (deg.)	30	40	50
θ_2 (deg.)	120	150	180

The details of experiments based on the Box–Behnken approach with three inputs and responses are summarized in Table 3.2. The mechanical responses measured from the analysis are Young's modulus, compressive strength and energy absorption capacity. The energy absorption efficiency of structures for different tailored designs is summarized in Table 3.2. Due to changes in geometrical parameters, volume and hence the density of the resulting unit-cell geometry changes, while the mass of the overall lattice structure was kept constant. The relative densities of the modified structures were also given in Table 3.2.

Table 3.2 Design matrix with input factors and responses

Factors			Responses			Other properties		
l_1:l_2 ratio (mm)	θ_1 (deg.)	θ_2 (deg.)	Young's modulus (MPa)	Compressive strength (MPa)	Energy absorbed (MJ/m^3)	Energy absorption efficiency (%)	Relative density $\bar{\rho}$	SEA (J/g)
4	30	120	90	1.5	1.768	48.65	0.33	5.33
4	40	150	106.3	3.4	1.968	31.86	0.39	5.02
7	40	120	111.2	2.7	1.271	30.40	0.40	3.16
7	50	150	175.14	3.45	1.137	24.75	0.51	2.2
4	40	150	100.65	3.25	1.810	34.83	0.39	4.61
1	40	120	87.32	3.58	2.986	54.97	0.31	9.58
7	40	180	138.05	4.85	1.992	29.35	0.44	4.5
4	40	150	108.65	3.05	1.756	33.45	0.39	4.48
4	30	180	86.86	3.25	2.351	39.84	0.36	6.5
1	30	150	73.73	2.37	2.526	52.41	0.30	8.38
4	50	120	145.17	4.01	1.972	23.80	0.45	4.36
4	50	180	193.93	3.1	0.983	22.53	0.55	1.78
1	50	150	106.45	3.05	1.773	32.74	0.40	4.41
1	40	180	122.75	3.5	1.524	23.67	0.44	3.45
7	30	150	74.50	2.4	1.678	41.05	0.34	4.91

3.3.1 Model development

The methodology model development and identification of an optimal design is shown in Fig. 3.2. The model was developed by using the Box–Behnken RSM technique which requires a smaller number of runs to generate accurate response surfaces than a normal factorial technique [67]. In Box–Behnken RSM technique the midpoints of the edges and center of the

cubical were considered as design points and hence twelve middle edge nodes and three center nodes were required to fit a polynomial.

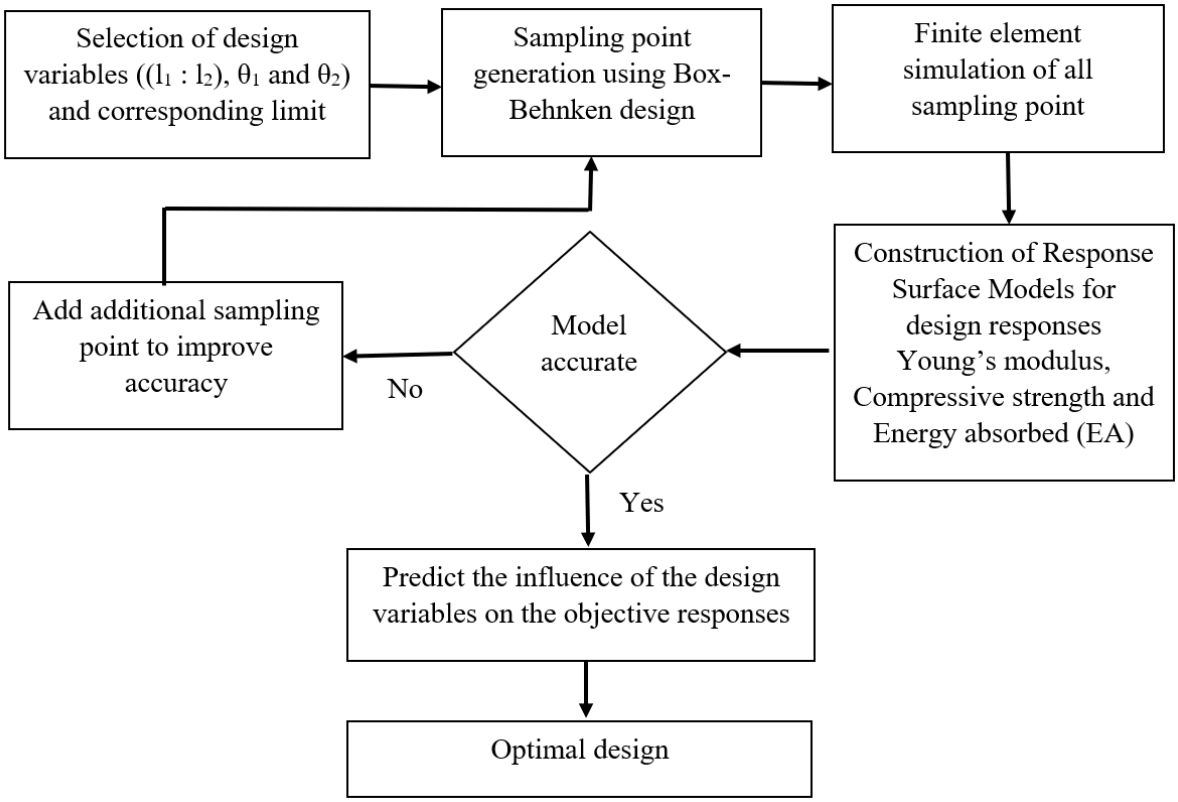

Fig. 3.2 Flow chart of the design optimization process

The variables,'length ratio (l_1: l_2)', 'θ_1' and 'θ_2' were chosen as input and three responses i.e., 'Young's modulus', 'compressive strength' and 'energy absorption capacity' were selected as output functions. Simulation data were fitted to generate mathematical models and then the models were used to study the influence of design variables on mechanical responses of the structure.

The best-fit indicators characterizing the accuracy of the models revealed that the energy absorbed (EA) by the structure can be characterized using quadratic models while Young's modulus (E), and compressive strength can be characterized through reduced quadratic models (backward) as listed in equations 4.3, 4.4 and 4.5 respectively.

$$\text{Energy absorbed (EA)} = - 0.376457 - 1.08269\ l_1{:}l_2 + 0.2721\ \theta_1 - 0.003458\ \theta_2 + 0.002083\ l_1{:}\ l_2\ \theta_1 + 0.005497\ l_1{:}\ l_2\ \theta_2 - 0.001078\ \theta_1\ \theta_2 + 0.003627(l_1{:}\ l_2)^2 - 0.001435\ \theta_1^2 + 0.000089\ \theta_2^2 \quad (3.3)$$

$$\text{Young's modulus (E)} = 757.66246 - 18.12379\ l_1{:}\ l_2 - 12.01085\ \theta_1 - 6.61854\ \theta_2 + 0.566050\ l_1{:}\ l_2\ \theta_1 + 0.04325\ \theta_1\ \theta_2 + 0.086926\ \theta_1^2 + 0.017796\ \theta_2^2 \quad (3.4)$$

$$\text{Compressive strength} = -9.47763 - 1.36794\, l_{1:}\, l_2 + 0.889121\, \theta_1 - 0.054632\, \theta_2 + 0.007917\, l_{1:}\, l_2\, \theta_2 - 0.002213\, \theta_1\, \theta_2 + 0.024023(l_{1:}\, l_2)^2 - 0.006325\, \theta_1^2 + 0.000403\, \theta_2^2 \quad (3.5)$$

As shown in Table 3.3, analysis of variance (ANOVA) was used to evaluate the accuracy of the model: probability (p-value), coefficient of determination R^2, Adjusted R^2, Predicted R^2, and adequate precision. All model terms show high R^2 (>0.75) value with excellent agreement between the predicted and adjusted R^2, indicating the trustworthiness of the model. It is evident from ANOVA analysis that all the models are significant and can be used to make valid predictions within the range listed in Table 3.1.

Table 3.3 Analysis of variance (ANOVA) of the developed models

Model	F-value	P-value	Statistical measurements			
			R^2	Adj- R^2	Pre- R^2	Adeq-precision
Energy absorbed (EA)	117.8	<0.0001	0.9837	0.9763	0.9427	41.6573
Young's modulus (E)	38.36	<0.0001	0.9746	0.9492	0.8224	20.7162
Compressive strength	28.27	<0.0003	0.9742	0.9397	0.7852	21.8009

Fig. 3.3 shows a comparative analysis between model prediction and finite element results, suggesting that the developed model (Equations (3.3)–(3.5)) can adequately capture the non-linear relationship between the input and output variables of the structure.

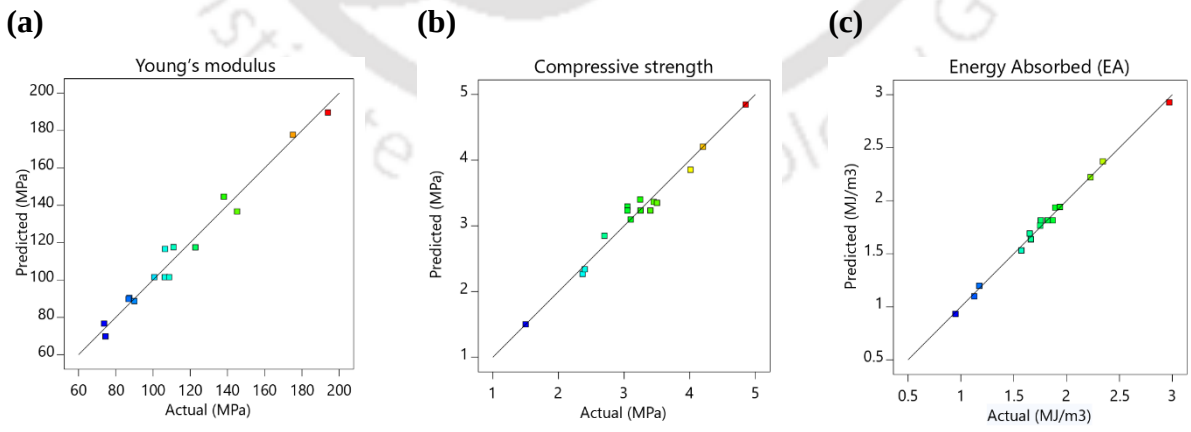

Fig. 3.3 Comparison of model predictions and finite element results for (a) Young's modulus, (b) compressive strength and (c) energy absorption of the structure

3.4 Result and discussion

3.4.1 Influence of design variables on energy absorption

Fig. 3.4 ((a), (b) and (c)) shows the effect of design variables on the energy absorption behavior of the structure. At a low value of θ_2 (120^0), the l_1:l_2 ratio has a higher influence on EA and the effect weakens as θ_2 increases from 120^0 to 180^0 (Fig. 3.4 ((a) and (b))). It can be seen from Fig. 3.4(a) that as the l_1: l_2 ratio increases from 1 to 7, EA ability of structure decreases significantly irrespective of θ_1 value. The RSM model predicted the highest (2.986 MJ/m^3) and lowest (0.983 MJ/m^3) EA value of the structure for l_1: l_2 ratio = 1 and 7 respectively.

In order to support these observations, deformation maps are presented in Fig. 3.5. The collapse mechanism of structure at a constant value of θ_2 (120^0) with a higher l_1: l_2 ratio and θ_1 (40^0) was found to be primarily due to bending with lower percolation of crush bands (Fig. 3.5(a)). But as the l_1: l_2 ratio decreases even with an increase of θ_1 (50^0) the structure deformation pattern changes; the structure first globally buckles from the center and then progressively deformed (Fig. 3.5(b)). Similar behavior was observed at θ_1 equals 30^0 (Fig. 3.5(c)). Structure with the least value of l_1: l_2 ratio (1) and θ_1 (30^0) showed higher global buckling with the highest percolation of crush bands (Fig. 3.5(d)). The perfolation of crush bands during compression affects the densification strain and hence the energy absorption of the structure. The percolation of crush bands depends on the rotational stiffness of the joints which is explained in section 3.4.5.

Fig. 3.4(c) shows that θ_1 has less effect on the EA property of the structure at the lower value of θ_2 and it becomes more significant with an increase in θ_2. At the highest value of θ_2 (i.e. 180^0) the structure response is analogous to that of the traditional regular re-entrant model and hence it is no more affected by the l_1: l_2 ratio. The lowest EA (0.983 MJ/m^3) value of the structure was found for θ_1 and θ_2 values at their highest levels (50^0, 180^0 respectively) as the deformation in such condition was not primarily due to bending, but it was due to stretching of inclined struts.

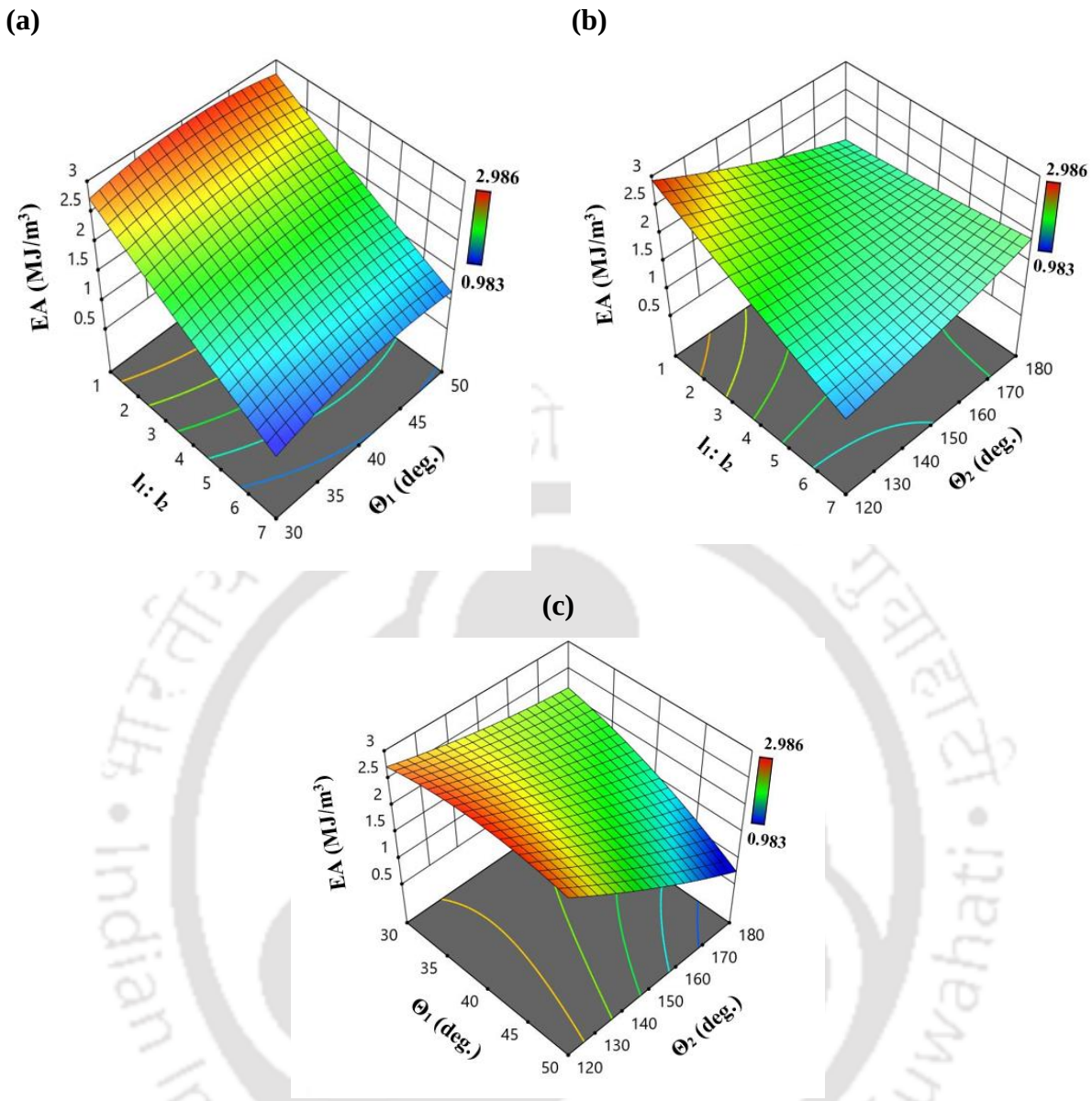

Fig. 3.4 Influence of geometrical parameters on energy absorption capacity (a) effect of l_1:l_2 and θ_1 when $\theta_2 = 120^0$, (b) effect of l_1:l_2 and θ_2 when $\theta_1 = 40^0$ and (c) effect of θ_1 and θ_2 when l_1:l_2 = 1

It can be concluded that the three design variables,l_1: l_2 ratio, θ_1 and θ_2 significantly influence EA behavior of the structure and the dependency of EA on the l_1: l_2 ratio was found to be linear while for θ_1 & θ_2, the relationship was quadratic. Accordingly, for improving the EA of the proposed structure, the most significant terms are in order of l_1: l_2 ratio followed by the joint angles (θ_2, θ_1).

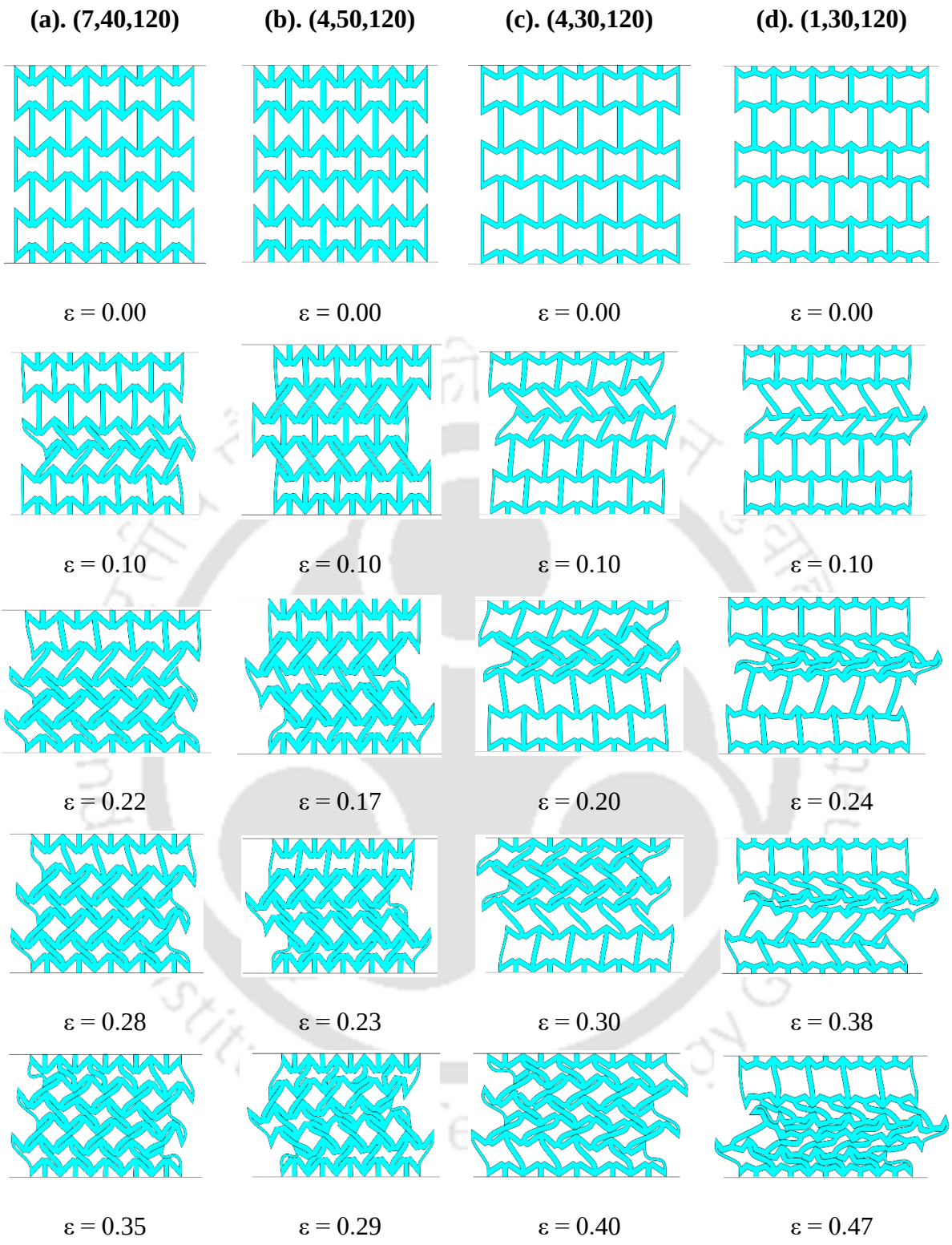

Fig. 3.5 Deformation sequences of different structures represented in terms of (l_1:l_2, θ_1, θ_2); (a) (7,40,120), (b) (4,50,120), (c) (4,30,120) and (d) (1,30,120)

3.4.2 Influence of design variables on compressive strength

Compressive strength determines the load-bearing capacity of a structure. The influence of design variables on the compressive strength of the proposed structure is shown in Fig. 3.6(a) and Fig. 3.6(b). It can be seen that the structure exhibits the highest compressive strength at a higher value of θ_1 and θ_2 (50^0, 180^0 respectively) and it continuously decreases with a decrease in joint angles while resulting in minimum strength at the lower value of θ_1=$30^0$and θ_2=120^0, respectively.

The model shows that θ_1 has the highest influence on compressive strength. The compressive strength increases quadratically with an increase in θ_1 from 30^0 to 50^0. θ_2 is the second most influential parameter with a linear relationship with compressive strength, while the l_1:l_2 ratio has the least effect on the strength.

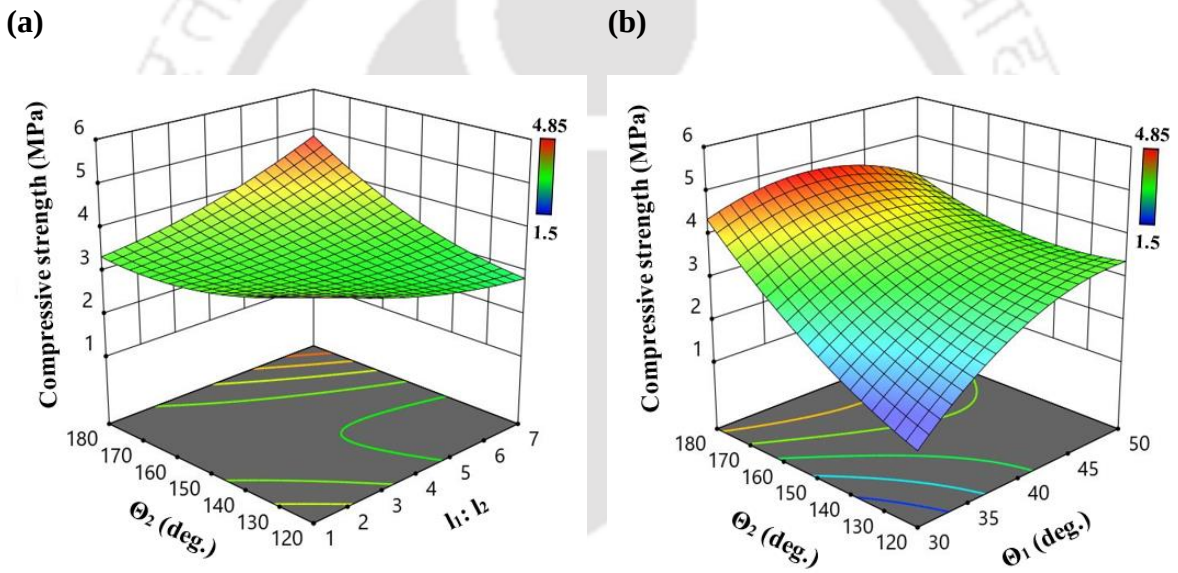

Fig. 3.6 Impact of geometrical variables on compressive strength (a) the effect of l_1:l_2 ratio and θ_2 when θ_1 is 40^0 and (b) the effect of θ_1 and θ_2 when l_1:l_2 ratio is 1

Fig. 3.7 shows the influence of design variables on the compressive strength of the modified re-entrant honeycomb structure. It can be clear from the below curves that θ_1 has the highest influence on compressive strength. θ_2 is the second most influential variable with a linear relationship with compressive strength, while the l_1:l_2 ratio has the least effect on the compressive strength. The influence of design variables can also be correlated with compressive strength by using a correlation factor. The correlation factor indicates the influence of design variables on the specific property. The higher the correlation factor, the

higher will be its influence on the property. It is also clear from the Correlation factor that θ_1 has the highest influence on compressive strength followed by θ_2 and l_1:l_2 ratio.

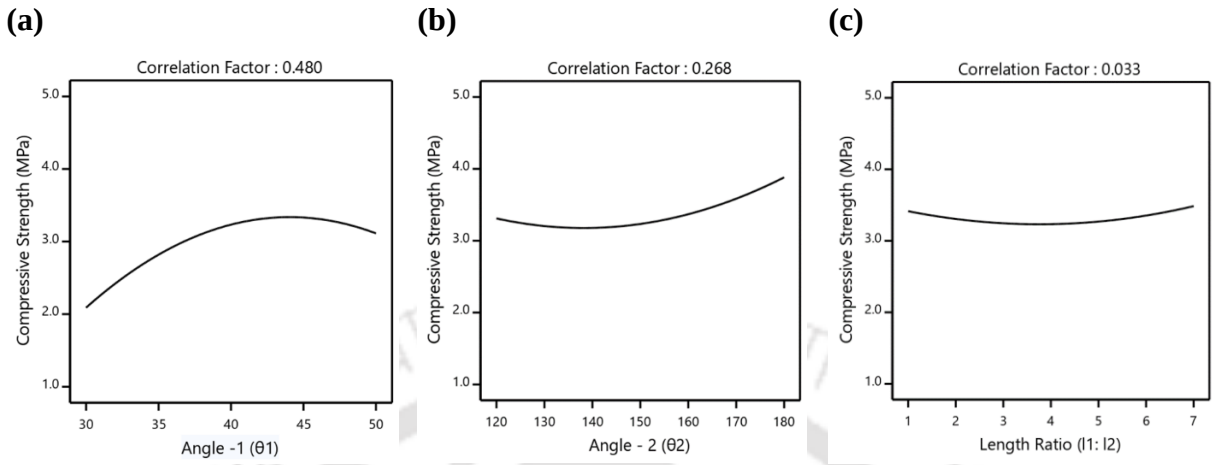

Fig. 3.7 Influence of design variables on compressive strength of modified re-entrant honeycomb structure (a). angle-1 (θ_1), (b). angle-1 (θ_1) and (c) length ratio (l_1: l_2)

3.4.3 Influence of design variables on Young's modulus

Fig. 3.8((a) and (b)) show the effect of design variables on Young's modulus of the structure. It is evident from Fig. 3.8(a) that the modulus is varying linearly with θ_1 and it has the highest influence on the response while θ_2 has the least contribution. The effect of the l_1:l_2 ratio is significant only at a higher value of θ_1 and it reduces with a decrease in the θ_1 value (Fig. 3.8(b)).

At higher values of l_1:l_2 ratio and θ_1, the model suggests a higher Young's modulus which is logical. This can be explained by analyzing the elastic collapse of the structure. Fig. 3.9 represents the Elastic collapse of the structure at the highest value of θ_2 (180^0). Due to quasi-static compression along the y-direction, the structure experiences a macroscopic compressive stress σ along the y-direction (Fig. 3.9(a)). Due to compressive load inclined walls bend. The free body diagram of one inclined wall is shown in Fig. 3.9(b). For equilibrium in inclined wall AB, the force component along the y-direction is zero.

(a) **(b)**

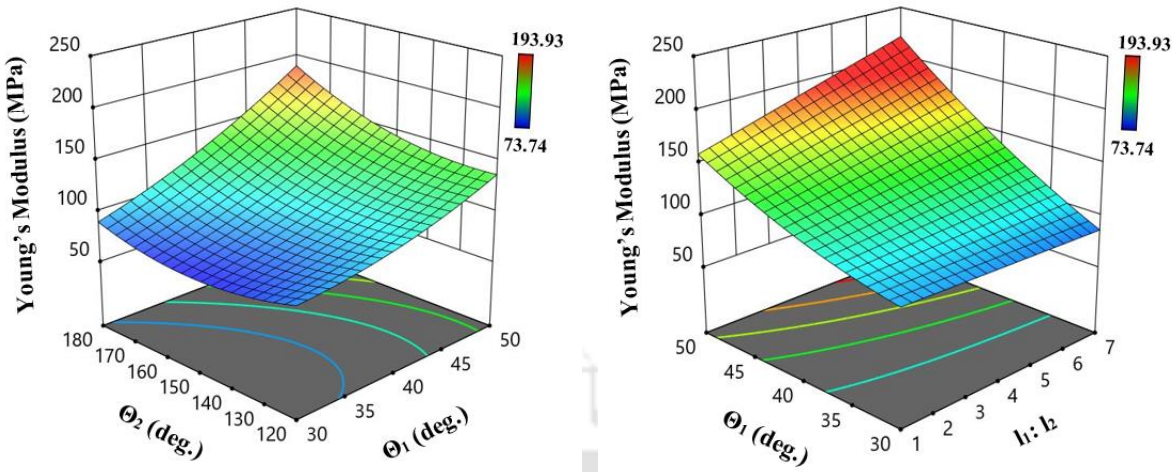

Fig. 3.8 Influence of geometrical variables on Young's modulus of the modified auxetic structure (a) the effect of θ_1 and θ_2 when l_1:l_2 ratio is 1 and (b) the effect of l_1:l_2 ratio and θ_1 when θ_2 is 120^0

The moment acting on the wall AB can be expressed as (equation 3.6)

$$M = \frac{Pl\cos\theta_1}{2} \tag{3.6}$$

where P is the force acting on the wall AB in the y-direction due to compressive stress (σ) which can be expressed as (equation 3.7)

$$P = \sigma bl\cos\theta_1 \tag{3.7}$$

where b is the width of the unit cell along the z-direction. The deflection (δ) of wall AB can be expressed as (equation 3.8)

$$\delta = \frac{Ml^2}{6E_s I} \tag{3.8}$$

where E_s is Young's modulus of basis material (ABS polymer) and I is the second moment of inertia ($\frac{bt^3}{12}$) of the inclined wall. Hence, strain along the y-direction can be written as (equation 3.9)

$$\epsilon = \frac{2\delta\cos\theta_1}{2(h - l\sin\theta_1)} \tag{3.9}$$

Young's modulus E of structure along the y-direction can be expressed as (equation 3.10)

$$E = \frac{\sigma}{\epsilon} \tag{3.10}$$

By plugging all equations (equations-(3.6-3.9)) in Young's modulus equation (equation 3.10) and rearranging, Young's modulus can be expressed as (equation 3.11)

$$E = \frac{E_s t^3(h - l\sin\theta_1)}{l^4\cos^3\theta_1} \tag{3.11}$$

From Young's modulus expression, it is clear that E varies as θ_1 changes (for all structures, all other parameters are constant when θ_2 is 180^0), and as θ_1 increases Young's modulus E also increases.

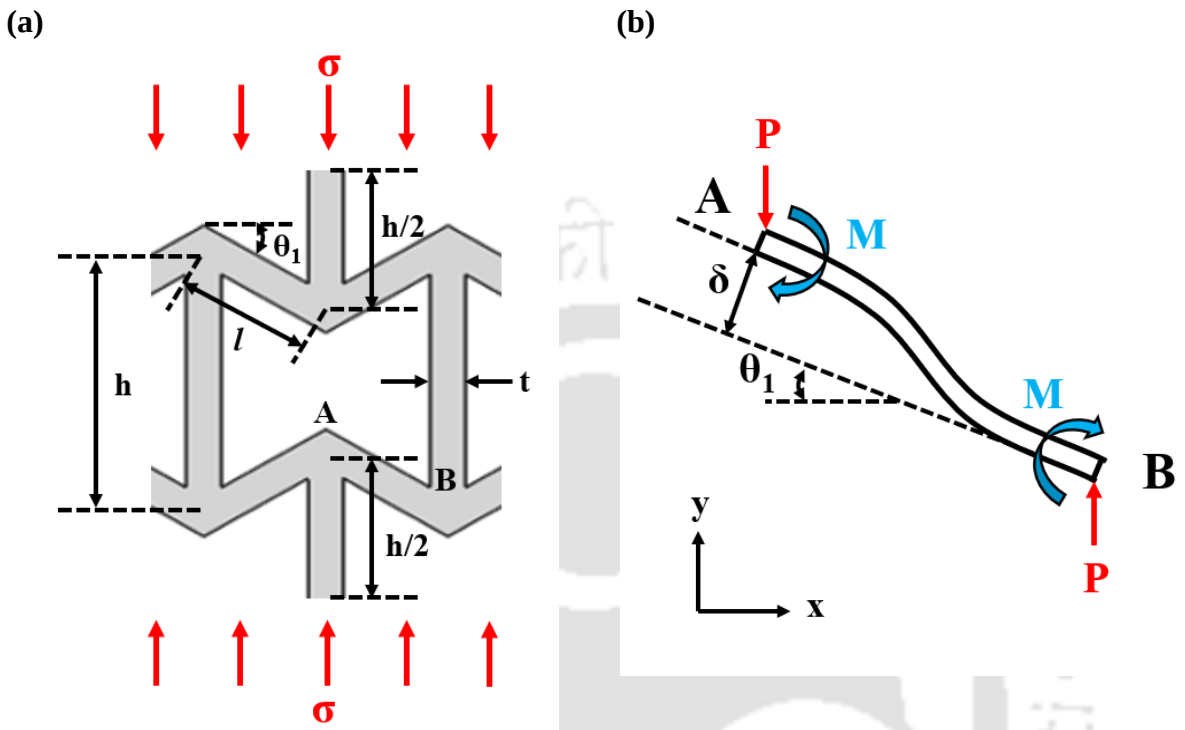

Fig. 3.9 Elastic collapse of structure at the highest value of θ_2 (180^0): (a) Unit cell with loading condition and (b) bending of the inclined link due to loading

Overall, it is clear from the above discussion that the relationship between the three variables (length ratio (l_1: l_2), θ_1 and θ_2) affects the mechanical and energy absorption properties of the proposed structure. In some cases, during the analysis, individual parameters effect was found to be dominating over their combined effect and vice-versa. It was observed that at higher levels of l_1:l_2 ratio, θ_1 and θ_2 (i.e. 7, 50^0, 180^0 respectively) the structure exhibits higher compressive strength and modulus but EA ability was low (as low plateau area due to lower failure strain). On the other hand, at the lower level of l_1:l_2 ratio, θ_1 and θ_2 (i.e.1,30^0,120^0 respectively) the structure shows a high value of EA (higher failure strain) with lower compressive strength and modulus respectively.

3.4.4 Optimal design parameters for energy absorption

After realizing the tunable mechanical properties of the modified structure, an optimal combination of design parameters for achieving the highest energy absorption is investigated

in this section. Therefore, single-objective optimization approach is used and the resulting optimization problem can be formulated as:

Maximize energy absorption (EA) = f (l.r., θ_1, θ_2) (3.12)

s.t. $1 \leq l.r \leq 7$

s.t. $30^0 \leq \theta_1 \leq 50^0$

s.t. $120^0 \leq \theta_2 \leq 180^0$

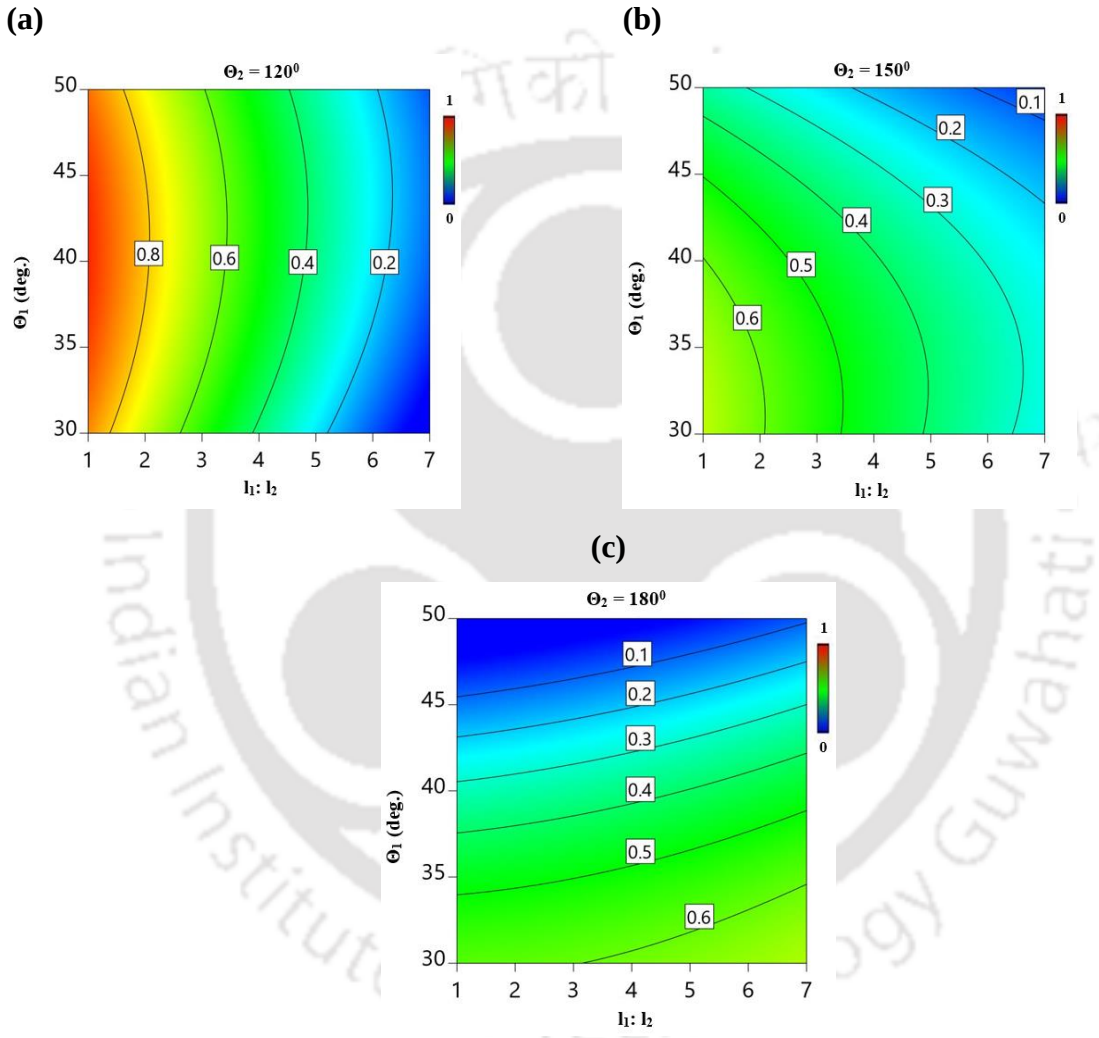

Fig. 3.10 Desirability plot of the optimum solution (a) effect of l_1:l_2 and θ_1 at $\theta_2 = 120^0$, (b) effect of l_1:l_2 and θ_1 at $\theta_2 = 150^0$ and (c) effect of l_1:l_2 and θ_1 at $\theta_2 = 180^0$

For optimization, each response must have a low and high value as represented by equation 3.12 and is solved using the desirability approach. Fig. 3.10((a)-(c)) shows the desirability plot of the optimum solution considering the three design variables as parameters. It appears that the optimal solution lies close to the lowest value of the l_1:l_2 ratio and θ_2 and at

a middle value of θ_1. Table 3.4 summarizes the optimal solution predicted by the model with the highest desirability (0.956).

Table 3.4 Optimal solution predicted by the model

l_1:l_2	θ_1	θ_2	Energy absorption
1	40^0	120^0	2.986 (MJ/m^3)

3.4.5 Crushing response of auxetic lattice structures

In order to compare the performance of the optimal modified structure with the regular re-entrant honeycomb lattice structure, the final design and regular re-entrant honeycomb lattice structure are 3D printed and experimentally tested. The 3D-printed regular re-entrant honeycomb (RH) and modified re-entrant (Modified RH) honeycomb are shown in Fig. 3.11. A regular re-entrant honeycomb with the same mass is considered for benchmarking.

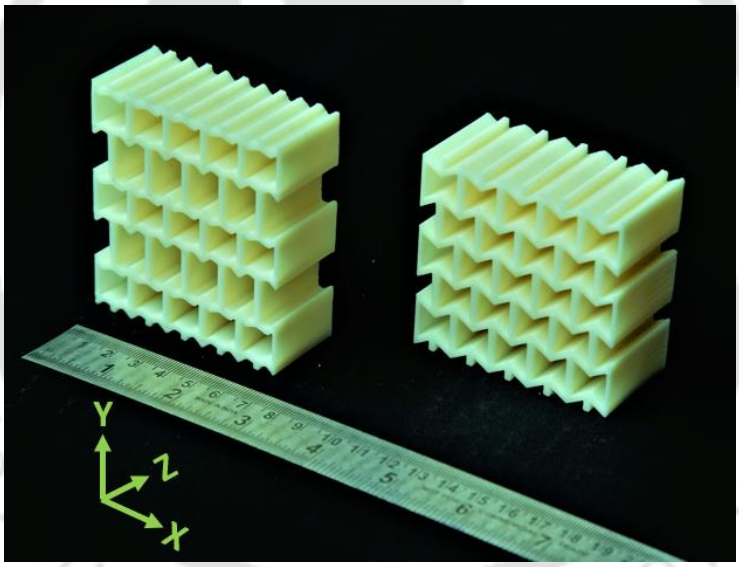

Fig. 3.11 FDM 3D printed Modified RH (left) and RH structure (right)

Fig. 3.12(a) shows a stress-strain curve of the Modified RH structure and RH structure. It is marked with numbers to signify its deformation behavior at different stages during compression.

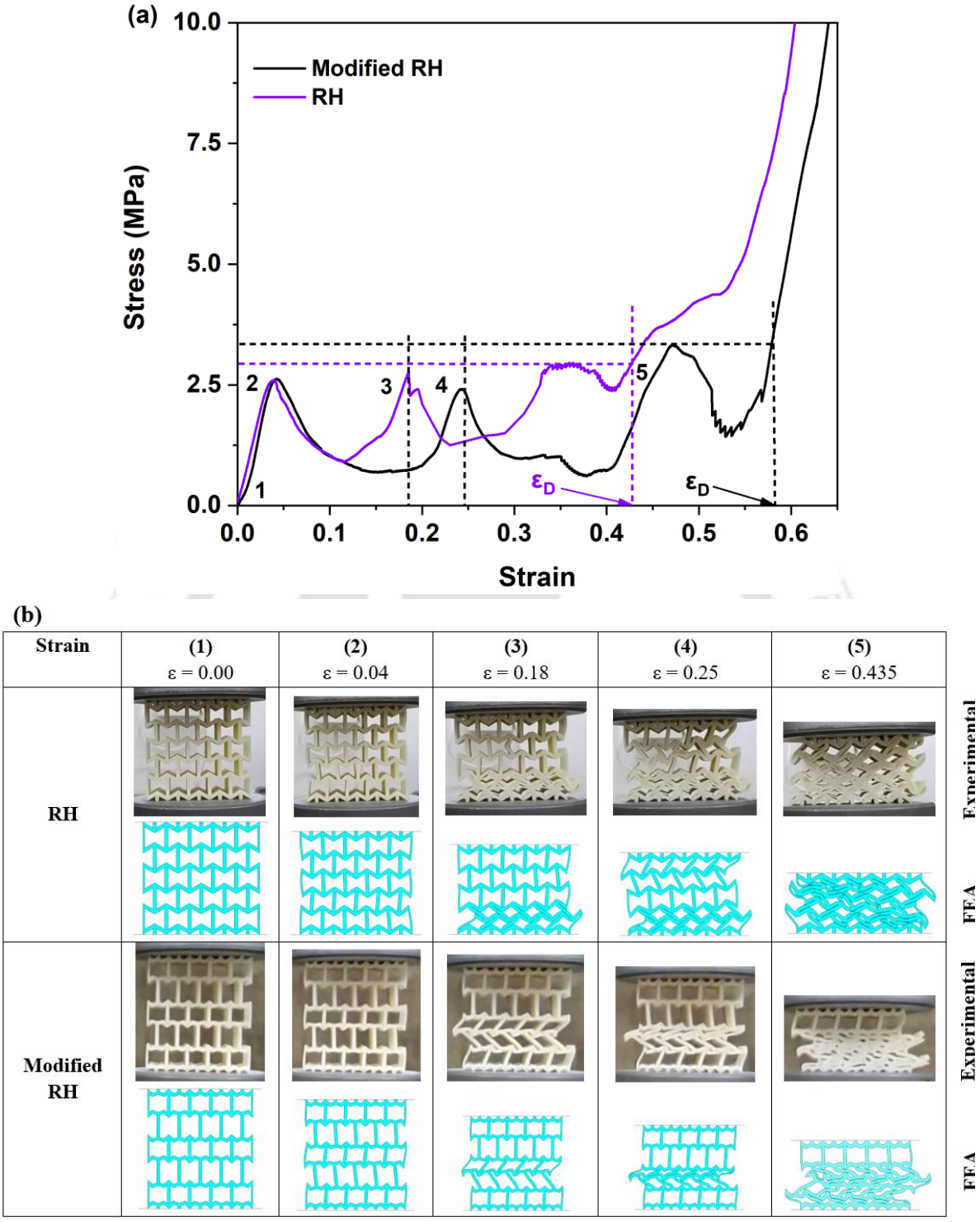

Fig. 3.12 Regular re-entrant honeycomb vs optimal structure: (a) stress-strain curve and (b) sequential deformation maps at different stages during quasi-static compression (see the corresponding points shown in the stress-strain curve)

Fig. 3.12(b) represents the sequential deformation maps during quasi-static compression at the corresponding points shown in the stress-strain curve. The optimal structure also shows three distinct stages as reported by several studies [8, 57]. In the beginning, a small region

known as the elastic regime was found where structures showed their linear elastic behavior, and after an initial peak, a large plateau was observed (plateau regime) while the densification regime starts when cell walls begin to come in contact with each other.

Results generated from the quasi-static compression test were used to calculate energy absorption characteristics of the structures and it is found that the Modified RH structure outperforms regular RH (+36.42%).

To further understand the energy absorption ability of Modified RH structure, sequences of deformed configurations (from optical images captured experimentally) at different strains are analyzed (Fig. 3.12(b)). From the experimental evidence (Fig. 3.12(b)), we observed that at the start of compression (elastic-regime) both structures show linear elastic behavior up to the yield point. There was a linear increase in stress, as the cells of the structures deform uniformly and reach a maximum value (Fig. 3.12(a)). As compression continues, further deformation behavior of the structure is influenced by the rotational stiffness of the nodes (joints). Rotational stiffness of the node (joint) is defined as the torque required per degree to rotate about the joints. The node with high rotational stiffness offers more resistance to rotation. The rotational stiffness of nodes is highly influenced by the number of inclined struts as they determine the degree of constraint to rotation [8].

In the case of regular re-entrant honeycomb, it can be seen from Fig. 3.13(a) that all the nodes (marked in blue) connected with 3 inclined links offer high resistance to rotation and hence during loading the cells collapsed due to buckling and bending. Such deformation propagates from one layer to other layers causing a progressive collapse of the structure. Cell collapse started from the bottom end and propagated towards the top of the structure (Fig. 3.12(b)). On the other hand, there are some nodes in the modified optimized structure, connected with only two inclined links called lower node connecting joints (marked in Red) (Fig. 3.13(b)), they offer less rotational stiffness compared with higher node connecting joints (marked in blue). Further, due to the low rotational stiffness offered by these nodes, the deformation was not able to propagate to the next layer until the complete layer collapsed, and therefore the low-stress plateau area increases which can be seen from the density of collapsed layer (higher in optimal structure as compared to regular re-entrant) (Fig. 3.12(b)). The stress values decrease as the first layer of the structure collapsed and then it again started to increase due to the densification of the collapsed cells. This behavior continues until all the rows are

collapsed. Finally, densification starts at the point when all the rows of the structures are collapsed (Fig. 3.12(a)).

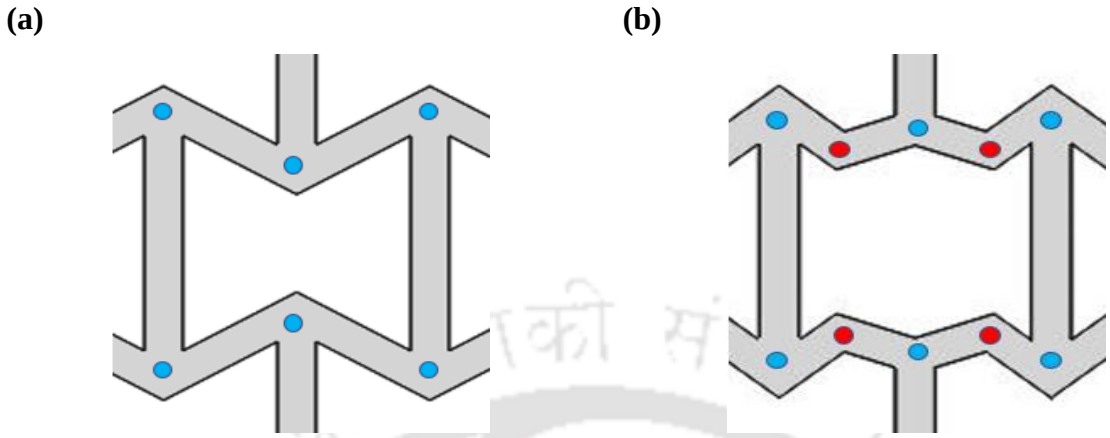

Fig. 3.13 Different types of node (joint) and their distribution in the unit cell of (a) RH structure and (b) Modified RH structure

Our analysis indicates that due to the introduction of more nodes with lower node connectivity, the onset of densification strain of the structure increases, resulting in improved EA of the Modified RH structure. After densification, the compaction of layers due to compression loading continues and hence the load value increases rapidly. It may be noted that within the compaction phase, the performance is determined by the base material and not by the structure [68], and the stiffness of the basic material is higher than the structure.

Table 3.5 shows the comparison of properties obtained experimentally for regular re-entrant honeycomb and our Modified RH structure. It is clear that the Modified RH structure outperforms regular re-entrant honeycomb (+36.42%) without much change in other properties.

Table 3.5 Performance of auxetic structures obtained experimentally

Properties	RH structure	Modified RH structure	Improve (%)
Young's modulus (MPa)	86.86	87.32	00.53
Compressive strength (MPa)	2.95	3.31	12.2
Energy absorbed (MJ/m^3)	2.161	2.948	36.42
SEA (J/Kg)	2064.56	2816.47	36.42

3.4.6 Poisson's ratio

Fig. 3.14 represents Poisson's ratio versus strain response of the regular re-entrant honeycomb structure and optimal structure. It is clear that both structures show a negative Poisson's ratio (NPR) and can be considered an auxetic structure. A similar variation in Poisson's ratio was observed for the lattice structures. In the early stages of loading, their NPR increases and becomes maximum, thereafter, further compression causes a decrease in the NPR.

The RH structure showed the highest auxeticity compared to that of the Modified RH structure with a Poisson's ratio of -1.502 and -1.324 respectively. As compression continues, lattices start deforming elastically, there is a sharp increase in NPR of regular re-entrant honeycomb structure while optimal structure showed a smooth increase in NPR. Both lattices showed the highest negative Poisson's ratio (NPR) near the end of the elastic regime. As lattices start deforming plastically there is a sharp drop in NPR is observed and gradually it moves toward the positive Poisson's ratio (PPR).

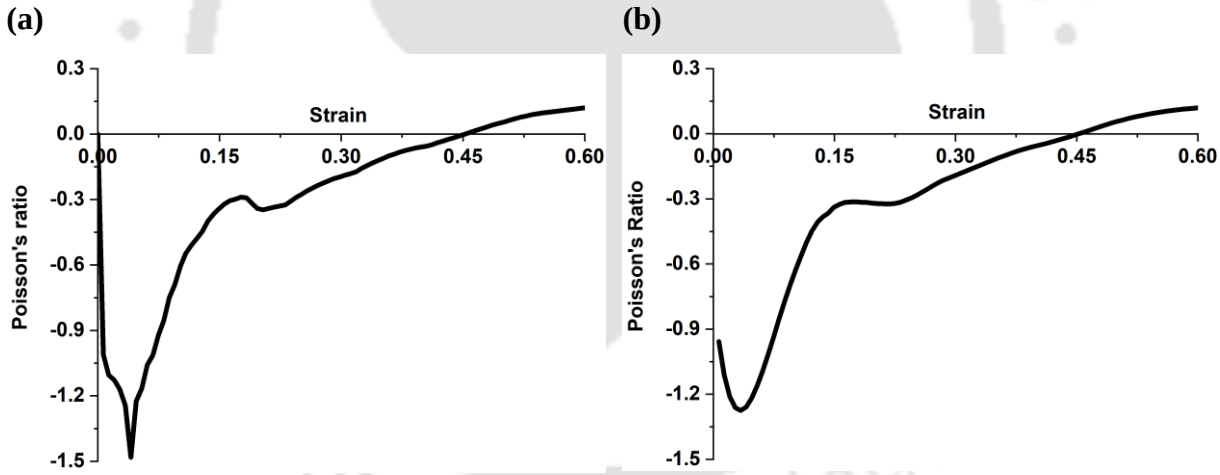

Fig. 3.14 Poisson's ratio versus strain response; (a) regular RH structure and (b) Modified RH structure

3.5 Summary

In this study, the in-plane energy absorption characteristics of modified re-entrant auxetic honeycombs realized via fused filament fabrication in conjunction with parametric analysis and geometry optimization. The influence and interaction effects of the geometrical parameters such as strut-length ratio and joint-angles on the stiffness, strength and energy absorption characteristics of modified re-entrant auxetic honeycombs were evaluated. Subsequently,

Finite Element results obtained using ABAQUS/Explicit were corroborated with measured data. Deformation mode, stress-strain response and energy absorption behavior of Modified RH were studied and compared with conventional RH structure. Our Modified RH structure reveals a 36% improvement in the specific energy absorption capacity. Our analysis indicates that due to the introduction of more nodes with low rotational stiffness, the failure strain of the Modified RH structure has increased resulting in improved energy absorption capacity.

Chapter 4 Enhanced energy absorption performance of 3D printed auxetic lattices

Auxetic lattices have unusual mechanical behavior and potential for an array of applications. However, a narrow window of stiffness realizable for a given cell topology limits their applications. This chapter aims to enhance the stiffness and energy absorption capabilities of the lattice structure simultaneously. A pair of novel re-entrant auxetic lattices capable of exhibiting enhanced stiffness and energy absorption is proposed by introducing vertical ligaments into Modified RH structures (previous work). The deformation patterns and the energy absorption characteristics of 3D printed auxetic lattices under quasi-static compression were investigated via both Finite Element (FE) simulations and experiments. The effective elastic stiffness of the proposed lattices was theoretically estimated based on Castigliano's second theorem. A parametric study has been done to study the effect of vertical strut thickness on strength, stiffness, and energy absorption capacity of the proposed lattice structure. [1]

[1]A portion of this chapter has been published in:

Choudhry, N. K., Panda B, Kumar S. Enhanced energy absorption performance of 3D printed 2D auxetic lattices. Thin-Walled Struct 2023;186:110650. https://doi.org/10.1016/j.tws.2023.110650.

4.1 Introduction

Auxetic lattices have attracted increasing attention due to their unusual mechanical behavior and potential for an array of applications. However, a narrow window of stiffness realizable for a given cell topology limits their applications. In this study, a pair of novel 2D re-entrant auxetic lattices capable of exhibiting enhanced stiffness and energy absorption is proposed by introducing vertical ligaments into Modified RH structures. The design modification includes selective addition of vertical ligaments to the Modified RH structure that resulted in enhanced stiffness and energy absorption without significantly altering relative density of the structure. These novel 2D re-entrant auxetic lattices were realized via fused deposition additive manufacturing. The deformation patterns and the energy absorption characteristics of 3D printed auxetic lattices under quasi-static compression were investigated via both Finite Element (FE) simulations and experiments. The effective elastic stiffness of the proposed lattices was theoretically estimated based on Castigliano's second theorem. The FE results corroborated by experiments, elucidate the role of different sub-cells on the effective mechanical properties of the proposed auxetic lattices. A parametric study has been done to study the effect of vertical strut thickness on strength, stiffness, and energy absorption capacity of the proposed lattice structure.

4.2 Novel auxetic lattices with vertical ligaments

Two new unit cells (Type-A and Type-B variants) were designed by adding vertical ligaments to the re-entrant honeycomb structure (Modified RH), described in the earlier work, as depicted in Fig. 4.1. The vertical ligaments are added to nodes or joints with higher node connectivity, while the lower node connecting joints remain unchanged. The presence of a low rotational stiffness joint allows easy rotation of inclined ligaments about the joint that enables higher compaction of deforming layers leading to an increase in onset of densification strain and therefore, the vertical ligament is added only at higher node connectivity joints (see Fig. 4.1(b)). The design parameters of Modified RH, Type-A and Type-B variants are summarised in Table 4.1. Table 4.2 shows the theoretical relative density of these two proposed structures obtained by unit cell analysis while neglecting the node size.

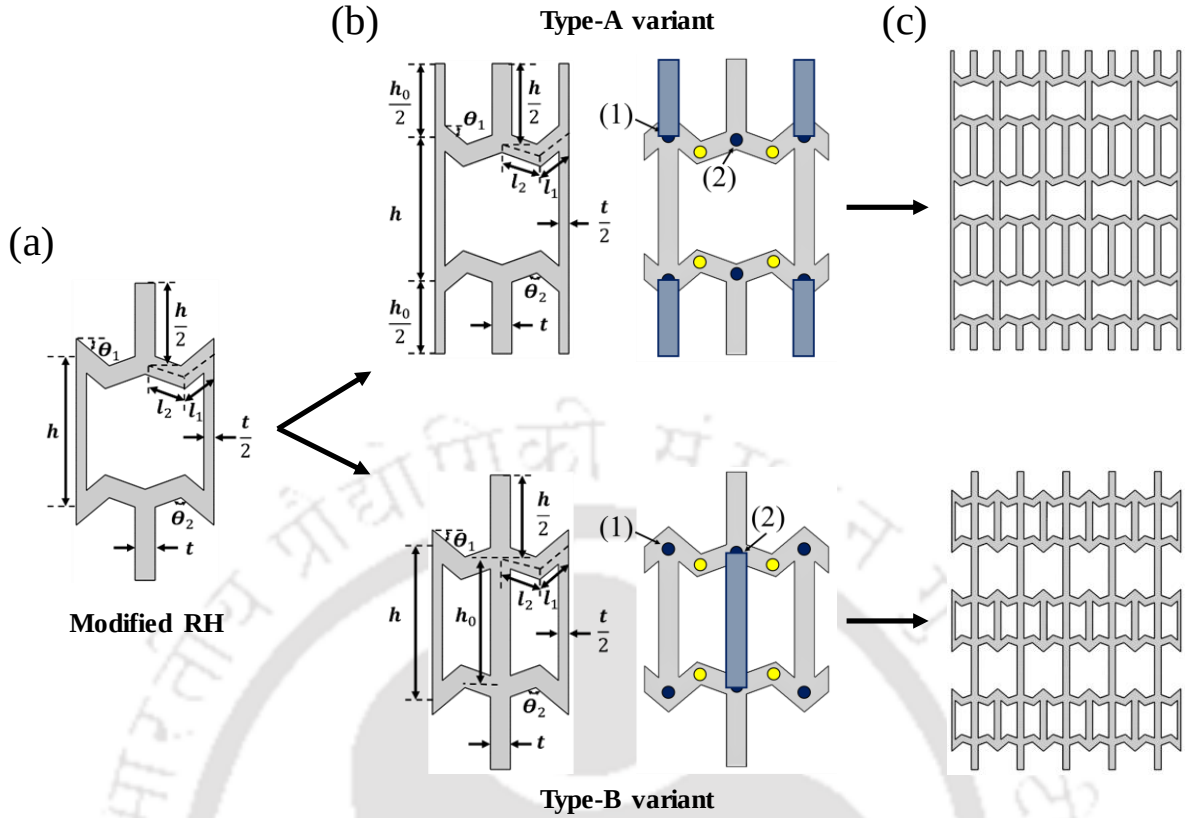

Fig. 4.1 (a) Unit cell topology of Modified RH lattice structure, (b) Type-A variant and Type-B variant unit cell topology (black dots represent nodes with higher connectivity; yellow dots represent nodes with lower connectivity; blue ligaments are added to the joints) and (c) 2D Type-A and Type-B lattices

Table 4.1 Architectural parameters of auxetic structures

Structure	h (mm)	h_0 (mm)	l_1 (mm)	l_2 (mm)	t (mm)	θ_1(°)	θ_2(°)	$\bar{\rho}$
Modified RH	16	-	4	4	2	40	120	0.310
Type-A Variant	16	10.98	4	4	2	40	120	0.349
Type-B Variant	16	13.59	4	4	2	40	120	0.346

Table 4.2 The relative density of Type-A and B auxetic structures

Auxetic structure	**Relative density ($\bar{\rho}$)**
Type-A Variant	$\bar{\rho} = \frac{\left(\left(\mathrm{h} + \frac{h_0}{2}\right) + 2(l_1 + l_2)\right)t}{(\mathrm{h} + h_0)(l_1 \cos\theta_1 - l_2 \cos(\theta_1 + \theta_2))}$
Type-B Variant	$\bar{\rho} = \frac{\left(\left(\mathrm{h} + \frac{h_0}{2}\right) + 2(l_1 + l_2)\right)t}{(\mathrm{h} + h_0)(l_1 \cos\theta_1 - l_2 \cos(\theta_1 + \theta_2))}$

4.3 Analytical prediction of effective Young's modulus

The energy method is employed to determine the elastic modulus of the auxetic lattices within the purview of linear elastostatics. To find out the expression for the average elastic modulus in the y direction (E_y), a compressive stress σ_y is applied to the structure as shown in Fig. 4.2(a). Note that vertical ligaments of the unit cell only experience the axial load. Fig. 4.2(b) represents the free-body diagram (FBD) of the unit cell, where F_1 and F_2 are the axial loads in the vertical member h and h_0 respectively. The sum of all forces in the Y direction for the whole unit cell must be equal to F (equation 4.1), i.e.

$$F_1 + F_2 = F \tag{4.1}$$

where F is the total force acting on the unit cell due to applied compressive stress σ_y. Out-of-plane thickness of the structure is assumed to be unity. Hence, the expression for F can be written as (equation 4.2)

$$F = 2\sigma_y(l_1 \cos\theta_1 - l_2 \cos(\theta_1 + \theta_2)) \tag{4.2}$$

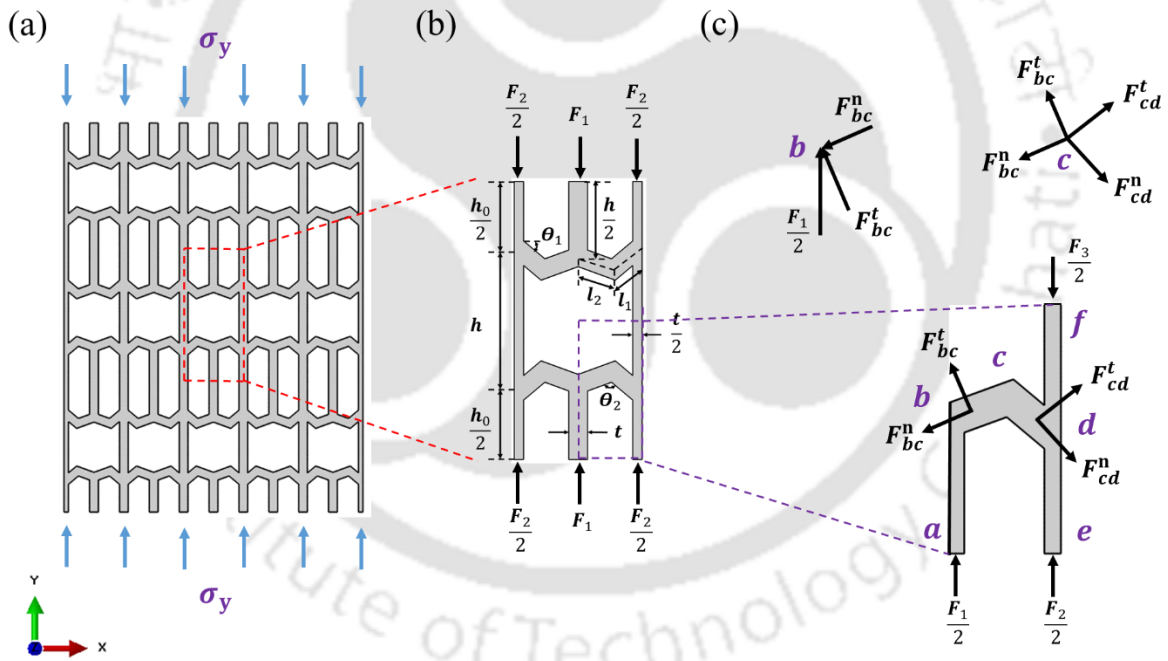

Fig. 4.2 Schematic representation of (a) 2D lattice structure of type-A variant under Y direction far-field compressive loading, (b) FBD of unit cell of type-A variant and (c) force experienced by different members of the unit cell and FBD of joints *b* and *c*

The analysis is further simplified by considering one-fourth of the unit cell i.e the part **abcde** (Fig. 4.2(c)). The inclined member **bc** and **cd** are subjected to both axial (F^n_{bc} and F^n_{cd} respectively) and transverse loads (F^t_{bc} and F^t_{cd} respectively) which are determined by

considering equilibrium of forces and method of joints (Fig. 4.2(c)). The expressions for axial and transverse loads (equation 4.3 to 4.6) are as follows

$$F_{bc}^{n} = \frac{F_1 \sin(\theta_1+\theta_2)}{2} \tag{4.3}$$

$$F_{bc}^{t} = \frac{F_1 \cos(\theta_1+\theta_2)}{2} \tag{4.4}$$

$$F_{cd}^{n} = \frac{F_1 \sin(\theta_1)}{2} \tag{4.5}$$

$$F_{bc}^{t} = \frac{F_1 \cos(\theta_1)}{2} \tag{4.6}$$

After computing the forces in different ligaments/members, the energy method is used to derive the expression for the stiffness of the lattice structure. Axial, bending and shear deformations are considered in the strain energy calculation, while strain energy due to torsion is ignored. The total strain energy stored in one-fourth of the unit cell is expressed as (equation 4.7):

$$U = \frac{1}{2}\int_0^{\frac{h}{2}} \frac{\left(\frac{F_1}{2}\right)^2}{\left(\frac{t}{2}\right)E_s} dx + \frac{1}{2}\int_0^{l_2} \frac{\left(\frac{F_1 \sin(\theta_1+\theta_2)}{2}\right)^2}{tE_s} dx + \frac{1}{2}\int_0^{l_2} \frac{\left(\frac{F_1 \cos(\theta_1+\theta_2)x}{2}\right)^2}{I_{bc}E_s} dx + \frac{1}{2}\int_0^{l_2} \frac{\left(\frac{F_1 \cos(\theta_1+\theta_2)}{2}\right)^2}{tkG_s} dx + \frac{1}{2}\int_0^{l_1} \frac{\left(\frac{F_1 \sin(\theta_1)}{2}\right)^2}{tE_s} dx + \frac{1}{2}\int_0^{l_1} \frac{\left(\frac{F_1 \cos(\theta_1)x}{2}\right)^2}{I_{cd}E_s} dx + \frac{1}{2}\int_0^{l_1} \frac{\left(\frac{F_1 \cos(\theta_1)}{2}\right)^2}{tkG_s} dx + \frac{1}{2}\int_0^{\frac{h_0}{2}} \frac{\left(\frac{F_2}{2}\right)^2}{\left(\frac{t}{2}\right)E_s} dx + \frac{1}{2}\int_0^{\frac{h}{2}} \frac{\left(\frac{F_3}{2}\right)^2}{\left(\frac{t}{2}\right)E_s} dx \tag{4.7}$$

where E_s is the elastic modulus and G_s is the shear modulus of the base material and k is the shear correction factor (a value of 0.83 is chosen for rectangular cross-section) which accounts for non-uniformity of shear strain within the ligament, [44]. I_{bc} and I_{cd} are moments of inertia of inclined member **bc** and **cd** respectively. As both inclined members have the same cross-sectional area, they have the same moment of inertia ($I_{bc} = I_{cd} = \frac{t^3}{12}$). Castigliano's second theorem is employed to find out the displacement of points. Hence total displacement (δ_y) of one-fourth part of the unit cell in the y direction with respect to **a** (considering $\delta_a = \frac{\partial U}{\partial\left(\frac{F_1}{2}\right)} = 0$) is expressed as (equation 4.8 & 4.9):

$$\delta_y = \delta_f - \delta_a \tag{4.8}$$

where δ_f and δ_a are the displacements of points **f** and **a** in the y direction respectively.

$$\delta_y = \frac{\partial U}{\partial\left(\frac{F_3}{2}\right)} = \frac{\left(4nh_0^2+4h(n+h_0)^2+h_0(n-h_0)^2\right)F}{8tE_s(n+h_0)^2} \tag{4.9}$$

where

$$n = \left(h + l_1 \sin^2 \theta_1 + 3.24 l_1 \cos^2 \theta_1 + \frac{4 {l_1}^3 \cos^2 \theta_1}{t^2} + l_2 \sin^2(\theta_1 + \theta_2) \right.$$

$$\left. + 3.24 l_2 \cos^2(\theta_1 + \theta_2) + \frac{4 {l_2}^3 \cos^2(\theta_1 + \theta_2)}{t^2} \right)$$

Now, average strain in y direction, ε_y is obtained as (equation 4.10):

$$\varepsilon_y = \frac{\delta_y}{\left(\frac{h+h_0}{2}\right)} \tag{4.10}$$

where, $\left(\frac{h+h_0}{2}\right)$ is the initial vertical distance between points **a** and **f**. Young's modulus for variant- A $\left(E_y^A\right)$ can be expressed as (equation 4.11):

$$E_y^A = \left(\frac{2t(h+h_0)(n+h_0)^2}{(l_1 \cos\theta_1 - l_2 \cos(\theta_1+\theta_2))(4nh_0^2 + 4h(n+h_0)^2 + h_0(n-h_0)^2)} \right) E_s \tag{4.11}$$

A similar approach is used to estimate Young's modulus of variant- B $\left(E_y^B\right)$, and can be expressed as (equation 4.12):

$$E_y^B = \left(\frac{2t(h+h_0)(n+h_0)^2}{(l_1 \cos\theta_1 - l_2 \cos(\theta_1+\theta_2))(nh_0^2 + 4h(n+h_0)^2 + h_0(2n+h_0)^2)} \right) E_s \tag{4.12}$$

4.4 Results and discussion

4.4.1 Effect of porosity on crushing performance

Fig. 4.3 shows stress-strain response of the structures obtained from FE analysis and experiment. A good agreement between FE and experimental results was found during elastic deformation. The discrepancy in post–yield response can be ascribed to the cracks (see Fig. 4.4) observed in 3D printed structures at some locations in the vertical struts during the early stages of deformation.

In the Type-A variant, deviation in the stress value was observed around 0.017 strain where the stress falls sharply due to cracking and it was confirmed by the deformation map (see Fig. 4.3(a)). It is clear from the FE deformation map that the high-stress concentration zones form near the joint at the deformed row corners (row at center) but fractures were not observed near any joints. However, in the experimental studies, micro pores were found in ligaments and one of the ligaments on the outermost right-hand side fractured (see Fig. 4.3(a)) and delaminated which leads to deviation in the results. Similar behavior was also observed for Type-B variant structure (Fig. 4.3(b)). Optical images captured at different locations within the structures are shown in Fig. 4.4. Similar issues associated with pores present in FDM printed

structures were reported in [69–71]. This process induced defects were not incorporated in this FE model. These defects could be minimized to some extent by optimizing the process parameters but to capture the localized failure of lattices accurately owing to localized triaxial stress-state, failure strain with respect to the stress triaxiality ought to be considered [72] and is left to a subsequent study. Nevertheless, due to similar deformation patterns obtained from experimental and FE studies, the FE model is used for further analysis.

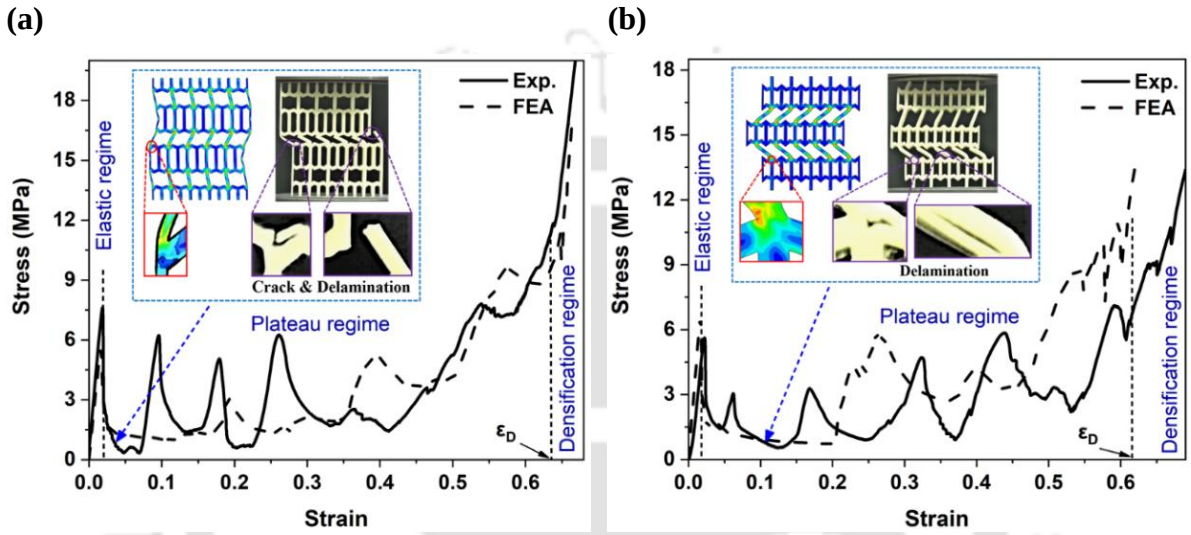

Fig. 4.3 Experimental vs predicted stress-strain response of (a) Type-A and (b) Type-B variant auxetic structures (arrow indicates onset strain of delamination)

Young's modulus and yield stress predicted by the FE model were also found to be consistent with experimental results. The maximum deviation between experimental and FE results for Young's modulus and yield stress was 6.14% and 7.26% respectively.

Optical images were taken from an optical microscope with a 10x magnification at different locations of the FDM printed part. Voids with different sizes were found at different cross-sections as shown in Fig. 4.4. It was observed that the vertical strut at some locations within the structures delaminated with an average gap of 0.2355 mm, while at some joints, material was partially filled leading to the formation of voids up to 0.571mm × 0.649mm. At the joints, the cross-section area is more than the ligaments, requiring more material to fill.

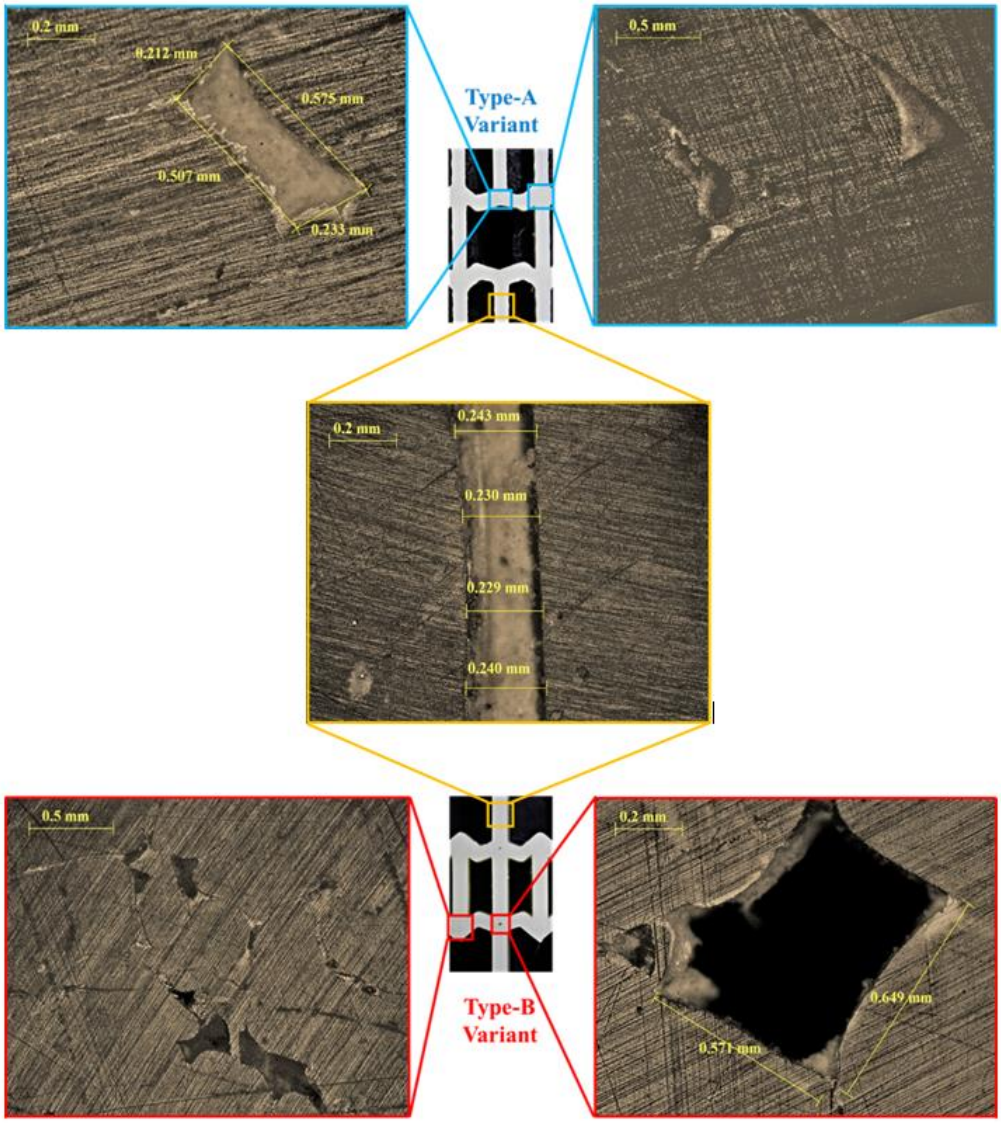

Fig. 4.4 Optical images of FDM printed parts at different cross-sections

4.4.2 Young's modulus, yield strength and compressive strength

The Young's modulus of Type A and B variants obtained by experimental testing, FEA, and theoretical models are summarized in Table 4.3. For both Type A and B variants, the theoretically predicted results were closer to the FE results. It was noted from experimental results (Table 4.3) that the Type-A variant showed the highest elastic modulus (384.73 MPa) followed by the Type-B variant (251.98 MPa). The 355% and 198% improvements in Young's modulus of Type-A and Type-B structures respectively in comparison to 'modified-RH' is due to their composite architecture with two sub-cells indicated as 'cell -1' and 'cell-2' (see Fig. 4.5). Like composite materials, the performance of lattice structure depends on their constitutive sub-cell properties and therefore, "rule of mixture" was used to estimate the overall stiffness of the structures (refer section 4.4.2.1). The rule of mixture is a theoretical model

widely used for the estimation of Young's modulus of the composite materials based on the volume fractions of constituent phases. In this study, the sub-cell properties were obtained using the theoretical expression (section 4.2). The predicted elastic moduli values using the volume fractions of sub-cells, show good agreement within the upper and lower bound curves of the composite rule of mixture (Table 4.5).

Table 4.3 Comparison of Young's modulus of the Type A and B Variant structures

Properties	Type-A Variant			Type-B Variant		
	FEA	Exp.	Theoretical	FEA	Exp.	Theoretical
Young's modulus (MPa)	362.53	384.73	379.74	266.73	251.98	272.59

4.4.2.1 Subcell effect on Young's modulus for Type A and B structures

The new type-A and B variant lattice structures are resulted due to addition of vertical ligament, which produces composite structures with different sub-cell properties (Fig. 4.5). The stiffness of these sub-cells can be compared and analyzed through Maxwell's stability factor (M) which highlights deformation mode of the sub-cells ($M \geq 0$, stretching dominated or $M < 0$, bending dominated). For all cases, Maxwell's stability factor (M) is less than zero and hence it has bending dominated deformation mode.

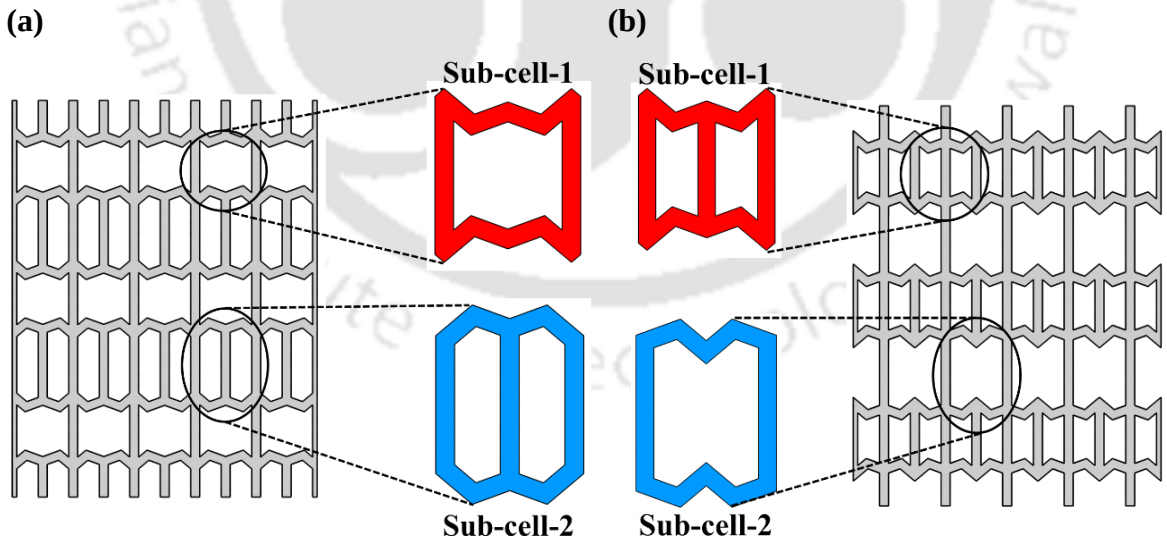

Fig. 4.5 Semi- regular binary edge to edge tessellation of structures highlighted with their sub cell (a) Type-A variant and (b) Type-B variant

The overall stiffness of the composite structures can be determined through the rule of mixture [73]. For this purpose, sub cell properties of Type A and B structures are first calculated

theoretically, and thereafter the rule of mixture has been used to get the upper and lower bound of Young's modulus. It is important to note that the sub-cells should be homogeneously dispersed throughout the structure. Fig. 4.5 shows the different sub-cells present within these structures.

The 'rule of mixture' for composite material was used to estimate the Young's modulus of Type A and B structures. The expressions used for the upper (equation 4.13) and lower bound (equation 4.14) of Young's modulus are as follows [74].

$$E(u) = E_A V_A + E_B V_B \tag{4.13}$$

$$E(l) = \frac{E_A E_B}{E_A V_B + E_B V_A} \tag{4.14}$$

Where $E(u)$ and $E(l)$ represent the upper and lower bound of Young's modulus for composite material respectively. V_A and V_B represent the volume fraction and E_A and E_B represent Young's modulus of constituent elements " A & B" respectively. Table 4.4 shows the properties of sub-cells, calculated using theoretical expression for stiffness (see section 4.3).

It was observed that for Type-A variant, sub cell 1 and 2 have Young's modulus of 437.24 MPa and 329.79 MPa, while Type-B have 464.38 MPa and 193.19 MPa respectively. Since these sub-cells have different volume fractions, mixture rule was applied to predict the final Young's modulus of Type A and B structures. The results are summarized in Table 4.5. It is clear from the results that the difference in Young's modulus of Type – A and B structures was mainly due to different sub cell properties and it's corresponding volume fractions.

Table 4.4 Properties of sub-cells derived theoretically

Sub-cell	Type-A variant			Type-B variant	
	V_i	E_{Ai} (MPa)	$\bar{\rho}_{Ai}$	E_{Bi} (MPa)	$\bar{\rho}_{Bi}$
Sub-cell-1	0.47	437.24	0.37	464.38	0.46
Sub-cell-2	0.53	329.79	0.33	193.19	0.25

Table 4.5 Comparison of a theoretical result of stiffness with "rule of mixture" prediction

Structure	Young's modulus (MPa)		
	$E(u)$	$E(l)$	Theoretical
Type-A Variant	380.2915	372.8549901	379.74
Type-B Variant	320.6493	266.275038	272.59

4.4.2.2 Scaling Law for Young's modulus and compressive strength

Fig. 4.6(a) and Fig. 4.6(b) show the scaling relation between macroscopic properties such as Young's modulus and compressive strength and the relative density for Type-A and Type-B variants. As per the Ashby model [8, 75], approximated relation for open-cell cellular structures for relative Young's modulus and relative compressive strength to relative lattice density are given by equation 4.15 and equation 4.16 respectively.

$$\frac{E}{E_S} = C_1 \left(\frac{\rho^*}{\rho}\right)^m \tag{4.15}$$

$$\frac{\sigma}{\sigma_S} = C_2 \left(\frac{\rho^*}{\rho}\right)^n \tag{4.16}$$

Where E and E_S are Young's moduli and σ and σ_S are the yield strengths of the cellular structure and its base material respectively, while ρ^* and ρ are the densities of cellular structure and its base material respectively. C_1 and C_2 are constants of proportionality and m and n are the exponents of the Ashby model.

Equation 4.15 is used to obtain the scaling relation between Young's modulus and the relative density for Type-A and Type-B variant structures, and the value of the geometric constant of proportionality C_1 and exponent m are obtained through curve fitting of relative modulus data obtained for various relative densities as discussed below and presented in Table 4.6.

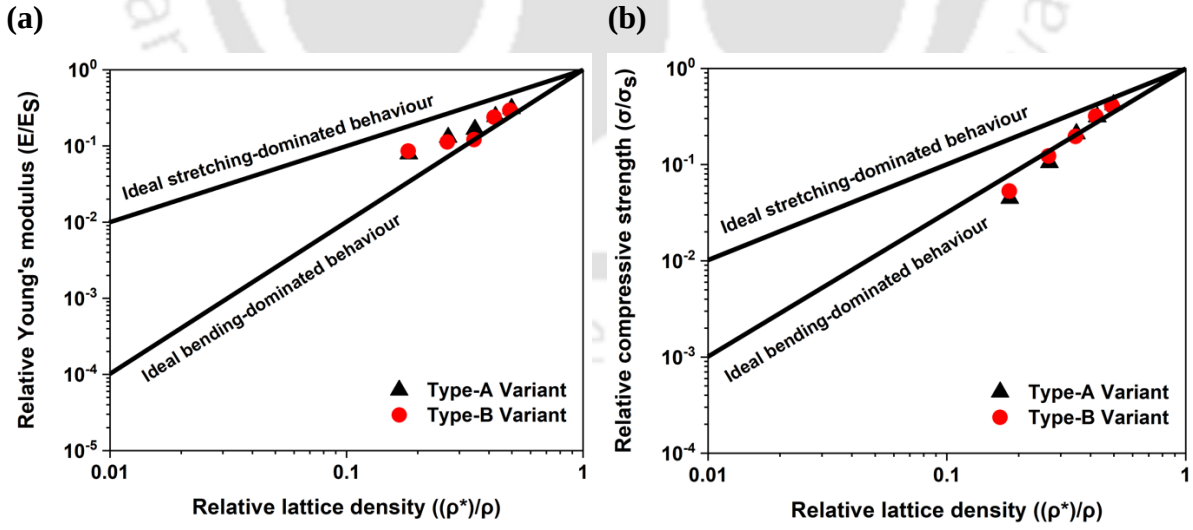

Fig. 4.6 Plot for (a) relative Young's modulus and (b) relative compressive strength (Solid lines represent ideal stretching and bending-dominated behavior)

The equation 4.17 used to understand the scaling relation between Young's modulus and the relative density for Type-A and Type-B variants.

$$\frac{E}{E_S} = C\left(\frac{\rho^*}{\rho}\right)^n \tag{4.17}$$

Where E and E_S are Young's modulus of cellular structure and its base material respectively, and ρ^* and ρ are the densities of cellular structure and its base material respectively while C and n are the geometric constants of proportionality and exponent respectively.

To get the value of "C and n" five data points were generated for each variant (Type-A and Type-B Variant) and Ln plots between relative Young's modulus and relative density are plotted (Fig. 4.7). Curves were fitted with 'linear fit' and 'intercept and slopes' of the curves are found which was further used to find the value of "C and n".

For getting the five data points of each variant (Type-A and Type-B Variant), the thickness of struts was varied from 1mm to 3mm in a step of 0.5mm while keeping all geometrical parameters constant. The FEA model was used to analyze, and numerical results were used to calculate the relative Young's modulus and relative densities for each setting.

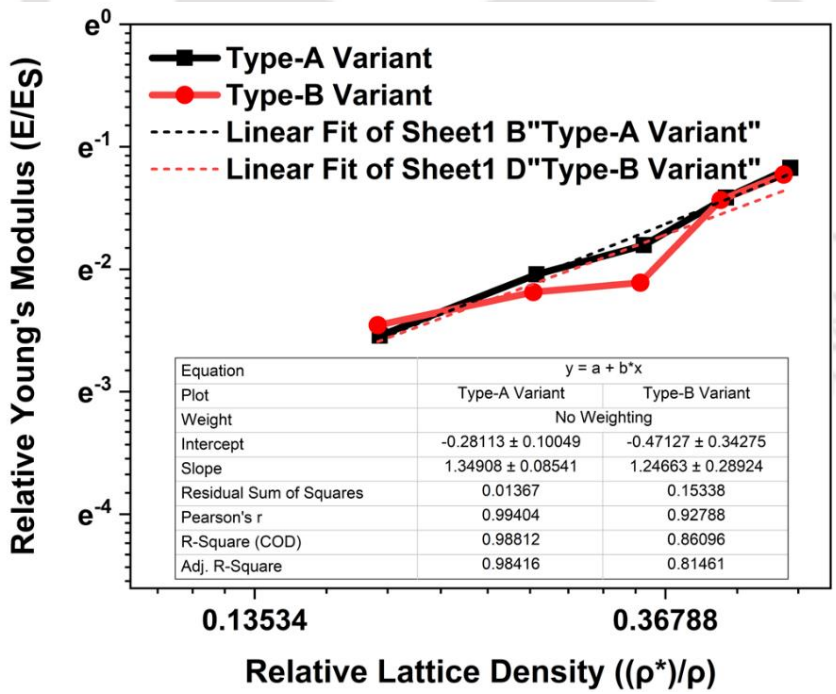

Equation	y = a + b*x	
Plot	Type-A Variant	Type-B Variant
Weight	No Weighting	
Intercept	-0.28113 ± 0.10049	-0.47127 ± 0.34275
Slope	1.34908 ± 0.08541	1.24663 ± 0.28924
Residual Sum of Squares	0.01367	0.15338
Pearson's r	0.99404	0.92788
R-Square (COD)	0.98812	0.86096
Adj. R-Square	0.98416	0.81461

Fig. 4.7 Ln plot between relative Young's modulus and relative lattice density of Type A and B Variants

The geometric constant of proportionality C_1 for the Type-A variant and Type-B variant structures is in the range of 0.683 to 0.835 and 0.443 to 0.879 respectively, while exponent m is in the range of 1.26 to 1.43 and 0.96 to 1.54 respectively. The value of C_2 and n were found using similar method. The geometric constant of proportionality C_2 for the Type-A

variant and Type-B variant structures are in the range of 0.683 to 0.835 and 0.443 to 0.879 respectively, while exponent n is in the range of 1.26 to 1.43 and 0.96 to 1.54 respectively. It can be concluded that both relations follow positive power law.

Table 4.6 Influence of thickness variation on Young's modulus and yield strength

t (mm)	Type-A variant			Type-B variant		
	$\bar{\rho}$	Young's modulus (MPa)	Yield strength (MPa)	$\bar{\rho}$	Young's modulus (MPa)	Yield strength (MPa)
1	0.18	173.08	1.38	0.18	188.72	1.64
1.5	0.27	285.66	3.25	0.27	247.13	3.79
2	0.35	362.53	6.48	0.35	266.73	6.06
2.5	0.43	534.51	9.70	0.42	524.21	9.88
3	0.50	680.63	12.97	0.49	644.82	12.65

As per the Gibson-Ashby model, the value of fitting exponent m (for Young's modulus) is 1 for stretch-dominated structures and 2 for bending-dominated structures, while fitting exponent n (for yield strength) is 1 and 1.5 for stretch-dominated and bending-dominated structures respectively [76, 77]. The fitting exponent m for both the structures are in the range of 1 and 2 (see Fig. 4.6(a)). It can be noted from Fig. 4.6(a) that at lower relative density, the deformation of the structure is bending-dominated and as relative density increases its degree is reduced. Further, Type-B variant has the largest m values for each relative density and hence shows more bending-dominated deformation behavior than that of Type-A. This confirms the enhanced stiffness is mainly attributed to the fact that the deformation mode is changing from more bending-dominated to less bending-dominated mode.

The compressive strength of a lattice structure is the maximum stress (σ_P) a structure can resist before densification. Fig. 4.6(b) shows the relative compressive strength as a function of relative density for all structures. The fitting exponent n for both variants is higher than 1.5. At low relative densities, the values of fitting exponent n reach a value of 2.347 and 2.13 for Type-A and Type-B variants respectively, and hence they exhibit bending–dominated deformation at lower relative density. As relative density increases, the influence of bending reduces. Type-B variant outperforms the Type-A variant in terms of compressive strength as it is highly anisotropic. It should be noted that isotropic structures deform and fail due to elastic buckling [75], which is responsible for lower stiffness and strength while anisotropic structures deform due to the presence of vertical pillars (parallel to loading direction) as these pillars directly

carry the compressive loads from top to bottom (entire length) of the structures leading to improved stiffness and strength of the structure.

Table 4.7 Comparison of Yield and compressive strengths of auxetic lattices

Structure	Yield strength (MPa)			Compressive strength (MPa)		
	Exp.	FEA	Error (%)	Exp.	FEA	Error (%)
RH	2.77	2.71	-2.21	2.85	2.92	2.39
Modified-RH	3.3	3.18	-3.77	3.27	3.46	5.49
Type-A Variant	7.62	6.48	-3.25	7.85	8.97	12.48
Type-B Variant	5.62	6.06	7.26	7.25	8.56	15.31

Table 4.7 presents the comparative analysis of yield strength and compressive strength of all structures with conventional RH structure.

4.4.3 Poisson's ratio

Fig. 4.8(a) shows Poisson's ratio versus strain relationship of specimens compressed quasi-statically along Y-direction. A similar variation in Poisson's ratio was observed for the RH, Type-A and Type-B variants. In the early stages of loading, their NPR increases and becomes maximum, thereafter, further compression causes a decrease in the NPR.

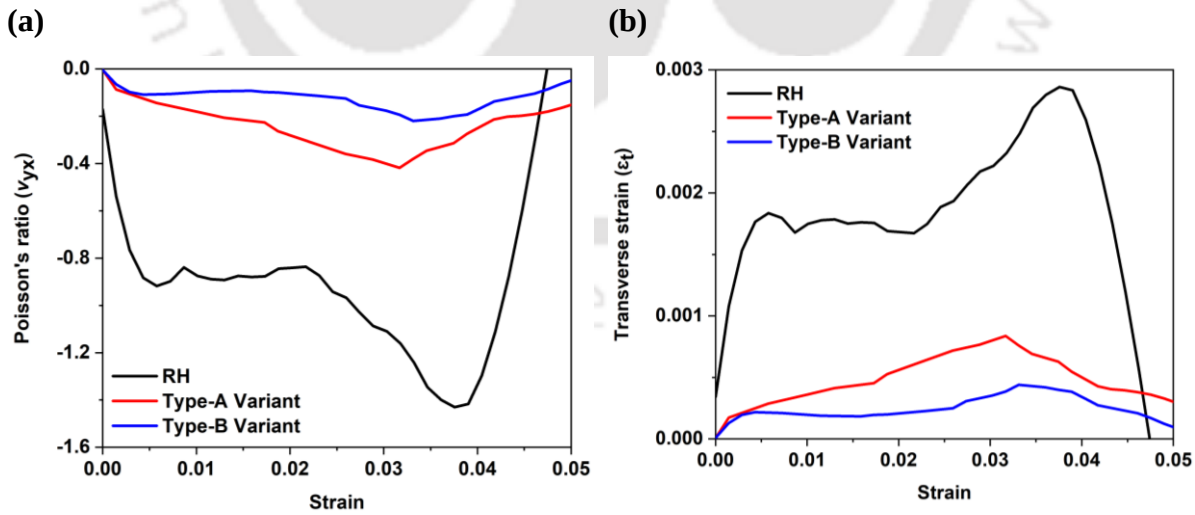

Fig. 4.8 (a) Poisson's ratio versus strain of test specimens and (b) corresponding transverse strain

The RH structure showed the highest auxeticity compared to that of the Type-A and Type-B variants with a Poisson's ratio of -1.324, -0.121 and -0.057 respectively as the inclined

wall of RH-structure moved easily inwards due to applied load leading to more transverse strain (Fig. 4.8(b)). However, due to the presence of vertical strut in Type-A and Type-B variants, the inward movement of inclined wall is restricted which lowers the transverse strain (Fig. 4.8(b)). The difference in auxeticity of RH-structure, Type-A and Type-B variants is mainly due to their geometry, as Poisson's ratio is geometry dependent parameter [78, 79]. The RH structure showed highest auxeticity compared to Type-A and Type-B variants and hence it is more compressible than Type-A and Type-B variants.

4.4.4 Energy absorption characteristics

4.4.4.1 Stress-strain response and deformation mechanism

Fig. 4.9 shows stress-strain curve and sequential deformation images of Type-A and B structures. Point-1 is taken within the elastic regime to observe the auxeticity of the structures. It can be seen from the deformation sequence (Fig. 4.9(b) and Fig. 4.9(d)) that both the structures contracted laterally resulting in NPR at point-1. Initially, the vertical walls of the structures only experienced axial loading, while inclined walls experienced both bending and axial loading due to which the inclined walls moved inward and the structure showed NPR.

For both the structures, initially, there is a linear increase in stress, as the cells of the structure deformed uniformly and elastically due to the instant stress distribution throughout the structure [80]. After reaching a maximum value, the stress dropped as plastic deformation started within the first layer of the structure and continuously decreases till the first layer completely collapsed. The point after which stress started dropping is marked as yield point (point-2) in both the structures. After the yield point, the deformation of structures was controlled by the sub-cell behaviour. Since the low relative density sub-cell is weaker than high relative density, initially the low relative density sub-cells were collapsed (point-3 & 4). The cells near the top and bottom plates encounter frictional resistance arising from contacting surfaces and leads to in-plane buckling of the structures (point-2). The sub-cell having lower relative density and away from the top and bottom plates is more unstable, deformed first (point-2 & 3). Thereafter, deformation moved to the other lower relative density cells, near to the top and bottom plates (as per their stability, point-4, Type-A variant). Once all the lower relative density sub-cells were deformed, the deformation wave moved to the higher relative density sub-cells (point-5 & 6) and continued till all the cells got collapsed.

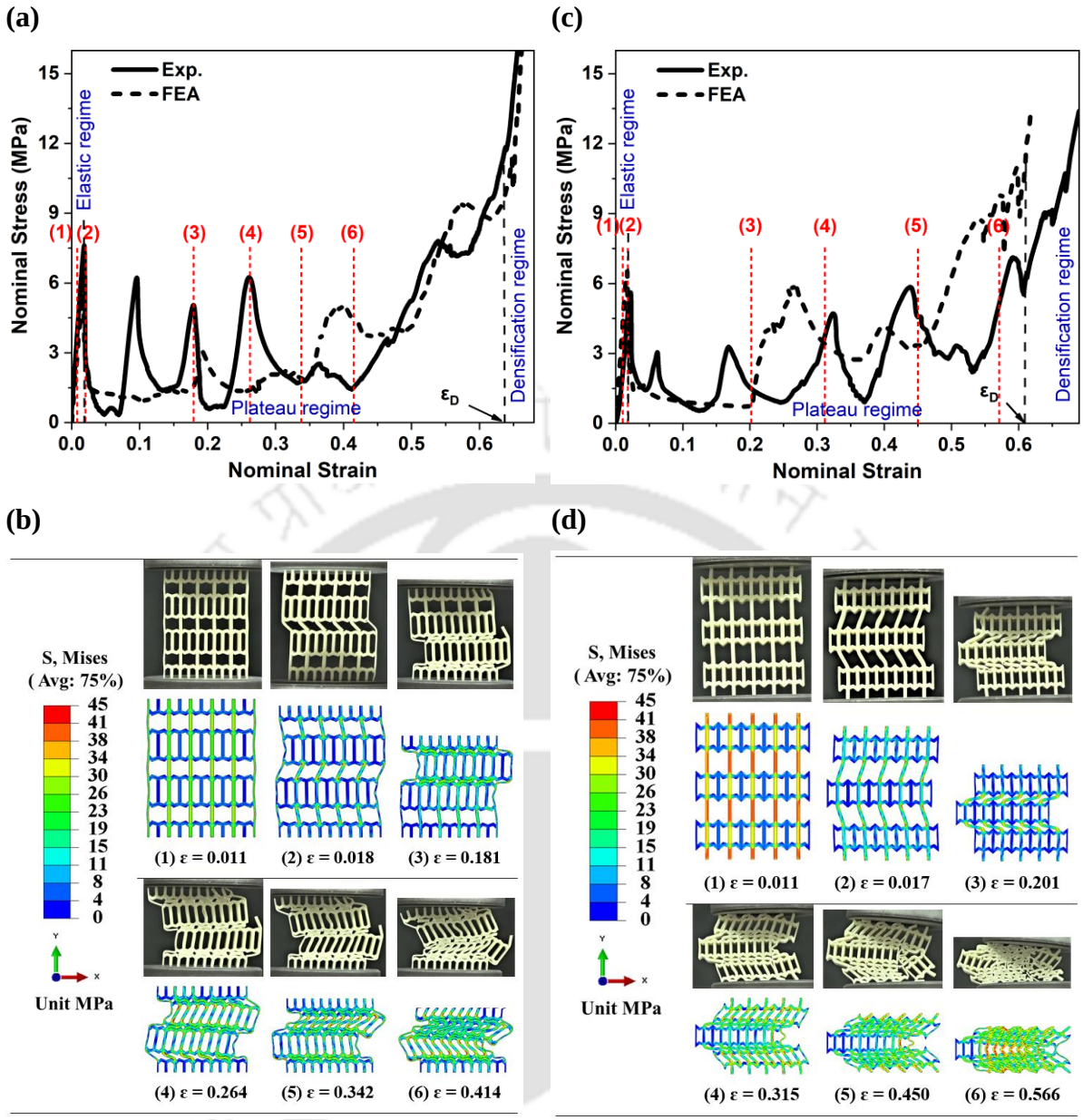

Fig. 4.9 Comparative analysis of auxetic structures: (a) stress-strain curve of Type-A variant (b) sequential deformation maps of Type-A variant (c) stress-strain curve of Type-B variant and (d) sequential deformation maps of Type-B variant

A fall in the stress was observed during the deformation of one unstable layer (sub cell), and it continued till complete layer deformed. Due to complete deformation of the layer, the stability of complete structure further increases, resisting more load (a sharp increase in stress) till another layer becomes unstable. This cyclic behavior of stress (increasing and decreasing) continues till all the rows were collapsed. Finally, densification started and after the densification, compaction of layers continues resulting rapid increase in the stress value.

4.4.4.2 Stress-strain response and deformation mechanism of subcells

Similarly, the difference in sub-cell properties can affect the energy absorption behavior of Type A and B structures. As shown in Fig. 4.10(a) there was a linear increase in stress, as both sub-cells of the structure deformed uniformly and elastically due to the instant stress distribution throughout the unit cell. This linear deformation continued till the unit cell is unstable, and stress drop was observed due to the collapse of the lower relative density sub-cell. After the yield point (end of the elastic regime), sub-cell-1 started deforming due to the buckling of vertical walls and continued till it completely deformed (up to $\varepsilon = 0.286$). Further compression causes rotation of the inclined strut about the lower node connecting joint which improves the stability of the unit cell, leading to a rise in stress value (up to $\varepsilon = 0.317$). Thereafter deformation of sub-cell-2 started and it collapsed due to bending. Finally, densification of the collapsed layer started as the lower node connecting joint allowed further rotation of the inclined strut, thus resulting denser deformed layer before the onset of densification (Fig. 4.10(a)).

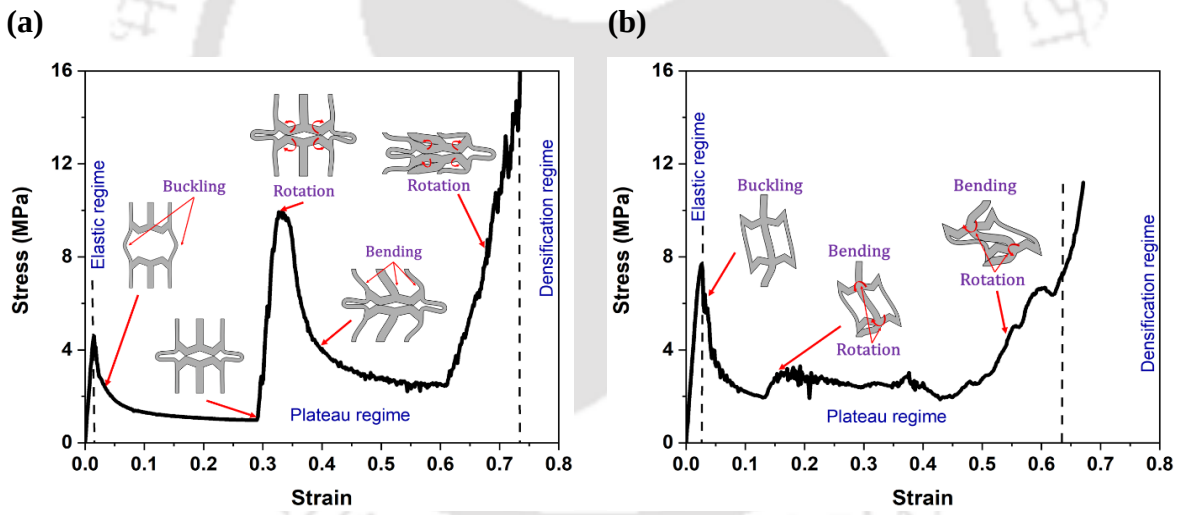

Fig. 4.10 Influence of sub-cell sequential deformation on the performance of the unit cell under quasi-static compression; (a) Type-A variant and (b) Type-B variant

On the other hand, sub-cell 2 of the Type B structure has a lower relative density than subcell-1. From Fig. 4.10(b) it is clear that after the yield point, sub-cell 2 started deforming due to the buckling of vertical walls and continued till complete collapse of the subcell (up to $\varepsilon = 0.135$). Further deformation causes rotation of sub-cell-1 about the joint which improves the stability of the unit cell, leading to increase in stress value (up to $\varepsilon = 0.175$). Thereafter deformation of sub-cell-1 started, where the sub-cell collapsed due to rotation and bending. It is clear from the unit cell deformation that after 0.2 strain, there is an abrupt increase in energy

absorption of the structure due to the deformation of higher relative density sub-cells, thus improving the overall energy absorption of the lattice structure.

Please note that these deformation modes are observed only with one unit cell in the model whereas the experiment and rest of the simulations were conducted for "m x n" number of cells because the number of cells are chosen such that we avoid the edge effect as detailed in the section 4.4.5.

4.4.4.3 Energy absorption

The energy absorption capacities of the structures are indicated by the hatched area under the stress-strain curve in Fig. 4.11 and it is clear that the energy absorption efficiency (red colour) of the structures increases with strain and attains maximum at densification strain. Despite having same relative density, energy absorption efficiencies of Type-A and Type-B variants are higher than RH structure by 41.12% and 13.93% respectively. Type-A variant has the highest energy absorption efficiency (43.27%) among all the four designs.

The specific energy absorption (SEA) was used to compare the structural performance. It is clear from Table 4.8 that the SEA of Type-A variant is the highest (6079.84 J/kg) among all the structures. The SEA of Type-B variant, modified-RH and RH are found to be 5870.23 J/kg, 2816.47 J/kg and 2179.25 J/kg respectively. The highest improvement in SEA was seen for Type-A variant (178.98%) followed by Type-B variant (169.37%) when compared with RH structure. Similarly, with respect to modified-RH, Type-A and Type-B variants have 115.87% and 108.42% higher SEA capability respectively.

Table 4.8 Energy absorption response of structures

Structure	Energy absorption capacity (MJ/ m^3)			Specific energy absorption (J/kg)			Energy absorption efficiency (%)		
	Exp.	FEA	Error (%)	Exp.	FEA	Error (%)	Exp.	FEA	Error (%)
RH	0.701	0.739	5.142	2179.25	2332.06	7.01	28.98	30.66	5.79
Modified-RH	0.912	0.962	5.497	2816.47	2994.23	6.311	37.45	39.85	6.41
Type-A Variant	2.217	2.412	8.784	6079.84	6651.97	9.41	40.27	43.27	7.45
Type-B Variant	2.057	2.263	10.01	5870.23	6395.85	8.95	31.95	34.93	9.99

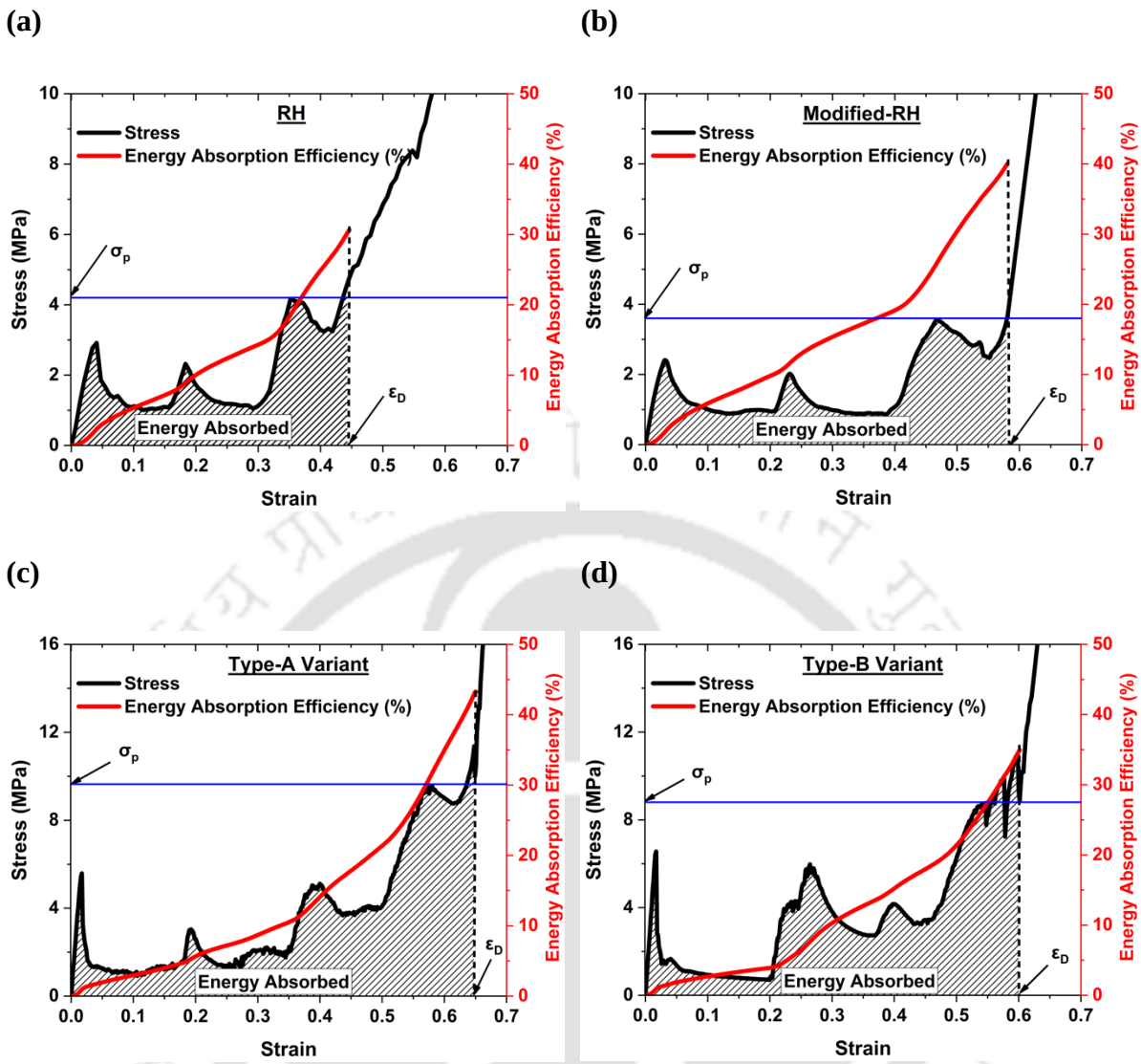

Fig. 4.11 Stress-strain response and energy absorption efficiency variation with strain: (a) RH, (b) Modified-RH, (c) Type-A variant and Type-B variant

The comparisons of energy absorption capacities of RH, Modified-RH, Type-A and Type-B variant structures under quasi-static compression are presented in Fig. 4.12(a). Initially, for all the structures, the EA curves coincide and vary linearly with lower slope up to strain value 0.2, which suggests low energy absorption capacity of the structures at lower strain. Type-A structure has slightly improved energy absorption at 0.2 strain. Further increase in strain leads to higher energy absorption of the structures with different rates. The energy absorption of the Type-A variant is the highest among all four structures. Table 4.8 shows a comparison of energy absorption capacity and energy absorption efficiency of all structures obtained both from experiments and FEA.

The normalized cumulative energy absorption versus peak stress plots for all lattice structures is presented in Fig. 4.12(b), following Gibson and Ashby et al. approach. Normalization of cumulative energy absorption and peak stress was done by dividing Young's modulus of the ABS material. Envelop is drawn at the best choice for a given maximum allowable stress (σ_P) of each structure, which relates energy absorption capacity (W_E) to the maximum allowable stress (σ_P).

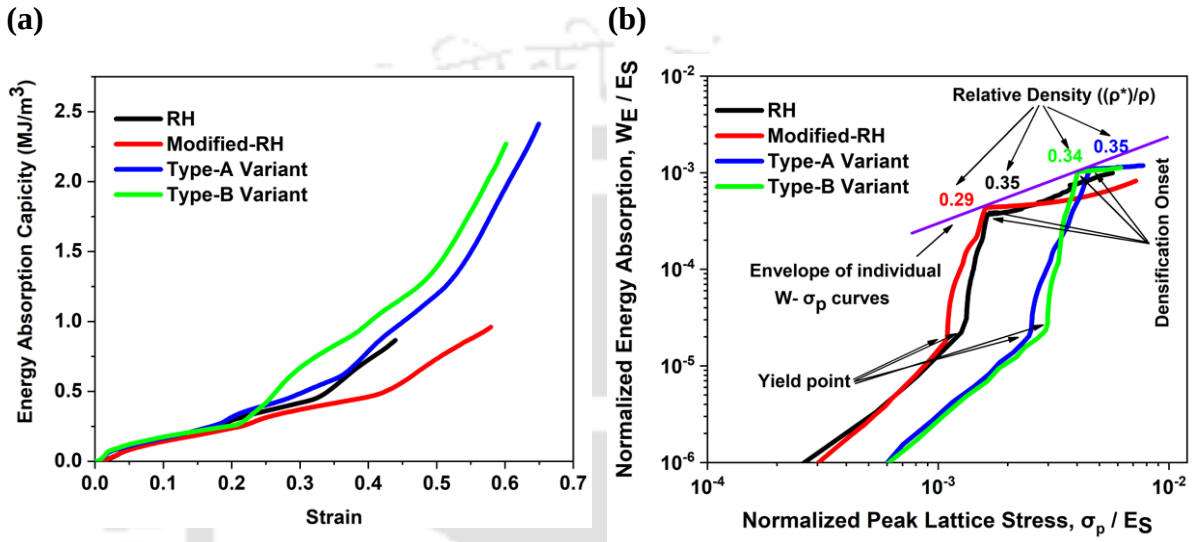

Fig. 4.12 Mechanical properties of RH, Modified-RH, Type-A variant and Type-B variant structures under quasi-static compression: (a) energy absorption capacity (b) normalized energy absorption plot, showing the envelope curve, the plastic yielding and densification onset points corresponding to the plateau region in the stress-strain curve

At normalized peak lattice stress smaller than 0.003, the Type-A and Type-B variant structures undergo deformation within the elastic regime, while RH and modified-RH structures exhibit inelastic deformation and hence have higher normalized energy absorption than Type-A and Type-B variants. Since inelastic regimes of the Type-A and Type-B variants are much higher than those of the RH and modified-RH structures, therefore they exhibit better performance in terms of total energy absorption.

4.4.5 Edge effect

In order to study the effect of no. of unit cells on the mechanical response of the structures, a series of numerical simulations were conducted on "m x n" unit cells structures, where 'm' and 'n' represents the number of unit cells in the row and column respectively. Fig.

4.13(a) represents the stress-strain response of "m x n" unit cells structure during compression. A more stable plateau region was observed with a single layer of structure and its stability decreased with an increase in the number of layers.

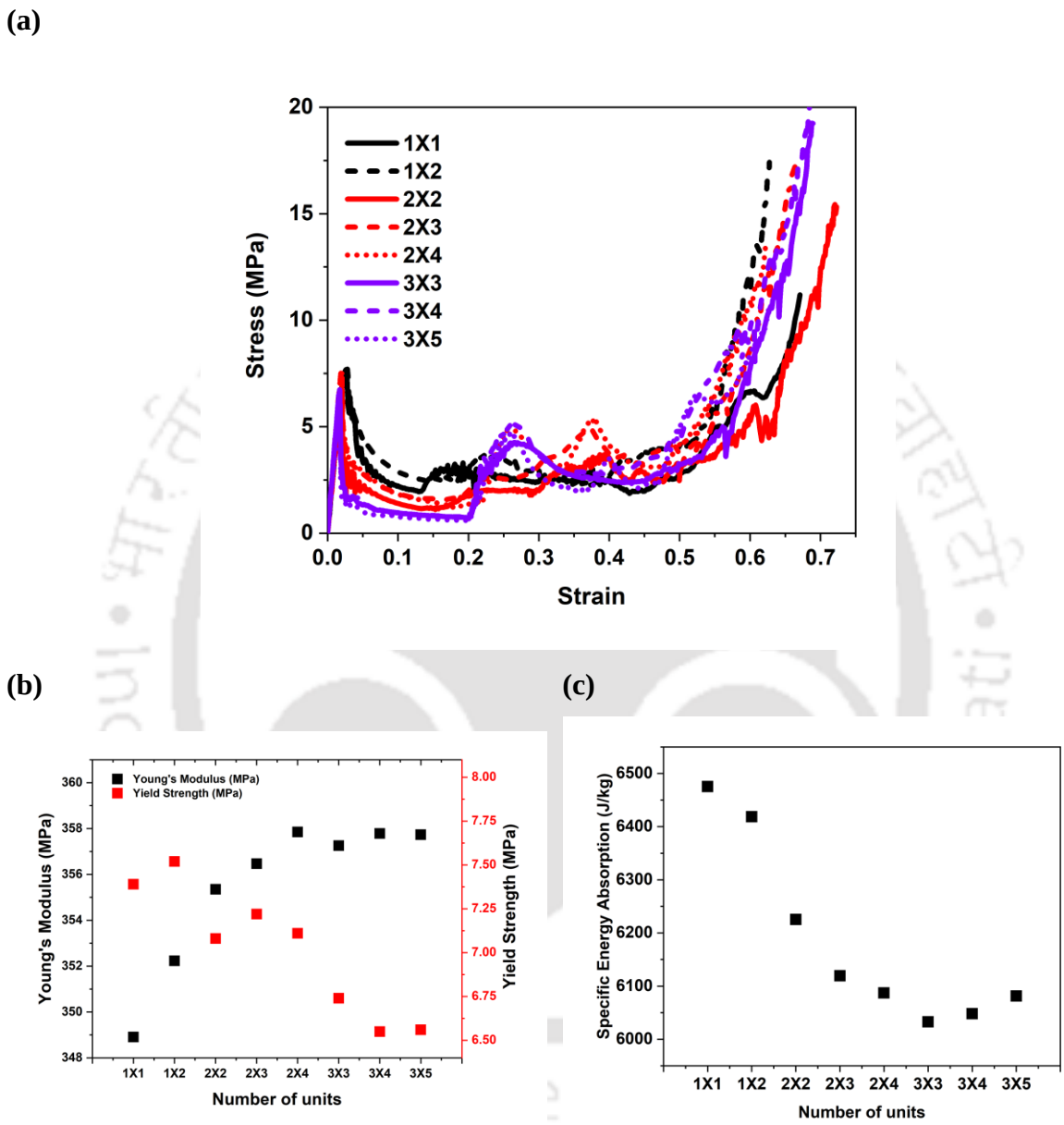

Fig. 4.13 Finite element modeling of Type-B variant lattices (a) stress-strain plots of all combinations of unit cells (b) Young's modulus and yield strength vs no. of unit cells plot and (c) specific energy absorption vs no. of unit cells plot

It was noted that in a single-layered structure, the stress was uniformly distributed over the load-bearing members (Table 4.9- 1x1) which leads to a stable plateau region while in the multi-stacked structure, the stress distribution over the load-bearing members was uneven. It

is clear from Table 4.9 that the deformation sequences at different strains differ due to changes in the number of layers as the number of layers affects the unit cell's boundary conditions. As compression continued, in the multi-stacked structure there was a random change in a load-bearing position (not found in a single-layered structure) which leads to stress fluctuations within the plateau region (Table 4.9- 2x2, 3x3). In addition, it is also found that there is a small improvement in densification strain due to an increase in layers within the structure. It is also noted that as more unit cells increased in a layer its average plateau stress increased with a decrease in densification strain.

It is noted that the elastic modulus increased quadratically as the no. of layers increased while yield strength reduced linearly with an increase in the no. of layers. The constraints applied at boundaries in the single-layered structure to large extent restricted movement perpendicular to loading direction and hence high yield strength while as the number of layers increased in the structures the effect of boundary constraints is not experienced by the intermediate layer and hence reduced yield strength. Further, as more unit cells were added in a layer, the fluctuation in Young's modulus and yield strength reduced and became stable after the third layer (Fig. 4.13(b)).

Table 4.9 Deformation sequences of "m x n" lattice structures with Von Mises stress distribution diagram

Strain	ε = 0.02	ε = 0.10	ε = 0.25	ε = 0.35	ε = 0.50	
1X1	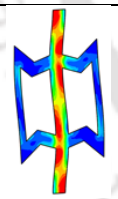	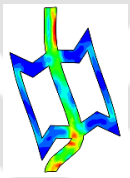	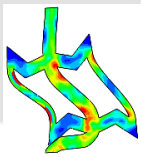	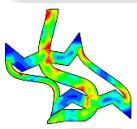	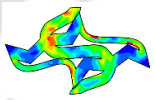	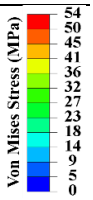
2X2	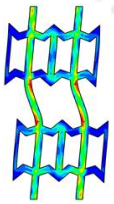	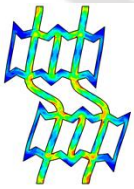	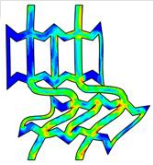	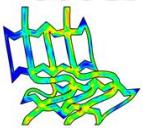	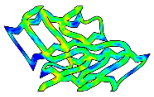	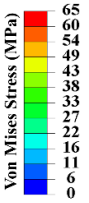
3X3	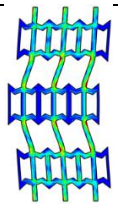	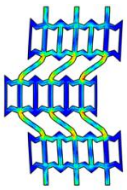	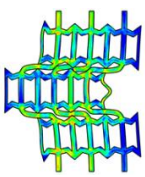	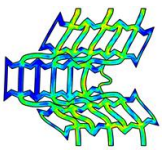	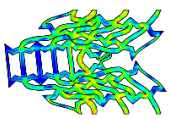	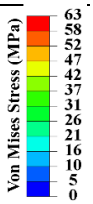

The specific energy absorption (SEA) of a structure is highly affected due to the edge effect. It can be seen from Fig. 4.13(c) that the structure having only one-unit cell showed the highest SEA (6475.45 J/kg), and SEA of the structure value decreased when more no. of unit cells were added, and finally, after adding more than 8 unit cells it becomes stable. For a single unit cell structure, both sides of the unit cell are free, and hence when compression continued they freely rotated about the center (Table 4.9, ε at 0.35 & 0.5) and showed higher densification strain due to well-known edge effects. As more no. of unit cells were added in a row, the rotational movement of the structure was restricted and hence earlier densification occurred which can be supported by the stress-strain curve (Fig. 4.13(a)).

4.4.6 Parametric analysis: The effect of vertical strut thickness

In this section, the effect of wall thickness variation of the added vertical strut on the performance of Type-A variant lattice structure was studied. The numerical model was used to study the influence of thickness, t, which varies from 1mm to 4mm on the mechanical response of the structure. Despite slight mismatch between experimental and numerical results post-yield, it is expected that the parametric investigation can provide useful information for designing optimal lattice structures.

4.4.6.1 Young's modulus and yield strength

The cell collapse behaviour of classical re-entrant honeycomb structure having variation in thickness of the walls is highly influenced by the weaker wall [5][34] and therefore, it was observed that the Type-A variants starts deforming plastically at the end of elastic regime. The behaviour of the elastic regime is governed by the weaker wall of the cell as shown in Fig. 4.14(a).

Fig. 4.14(b) shows the variation of Young's modulus and yield strength of Type-A variants with respect to different strut thickness 't'. For 1 mm strut thickness, the structure showed very low value of Young's modulus (292.5 MPa) and yield strength (4.11 MPa) as the cell collapsed due to buckling of thinner vertical strut (Fig. 4.14(c)-(1)). Further increase in thickness to 1.5mm, the collapse criteria changed from buckling to bending of the vertical members (Fig. 4.14(c)-(2)), and hence improvement was observed in both Young's modulus (347 MPa) and yield strength (6.15 MPa). The abrupt increase in the stiffness was observed when thickness increased from 2 mm to 2.5mm. Before the bending occurs, axial component

of the forces in the vertical wall contributes via axial yielding due to the short and squat wall [5].

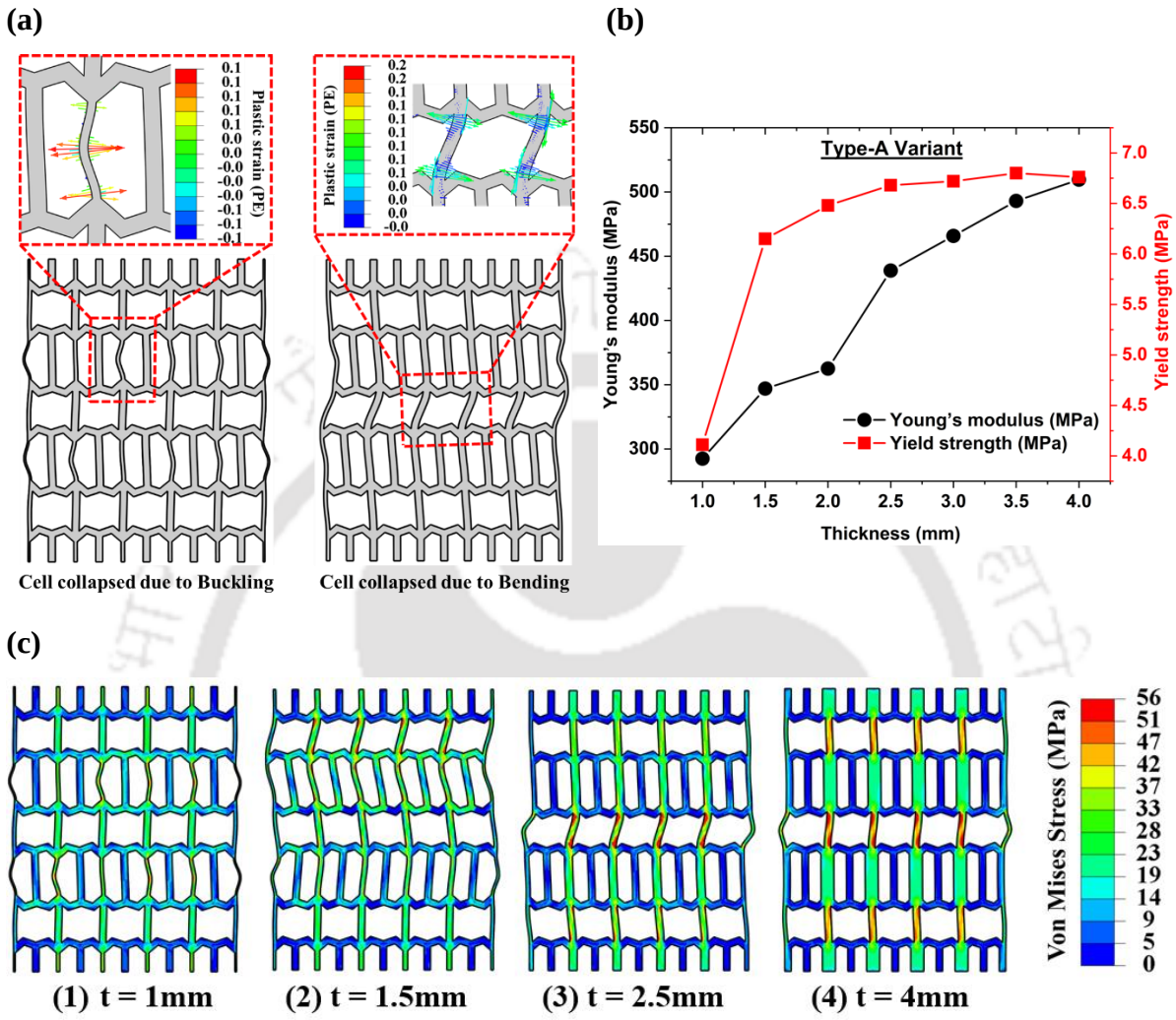

Fig. 4.14 Effect of vertical strut thickness on (a) cell collapse mechanism, (b) Young's modulus and yield strength and (c) deformation maps with Von Mises stress distribution at yield strain

Table 4.10 Mechanical properties of Type-A Variant

Properties	Thickness 't' (mm)						
	1	1.5	2	2.5	3	3.5	4
Young's modulus (MPa)	292.5	347	362.53	438.8	465.8	493	509.6
Yield strength (MPa)	4.11	6.15	6.48	6.68	6.72	6.80	6.76
$\bar{\rho}$	0.32	0.33	0.35	0.37	0.38	0.40	0.42

This contribution results in higher stiffness which can be visualised by stress-bearing capacity of the elastically deforming vertical wall before plastic collapse (Fig. 4.14(c)-(3)). Further increase in thickness (to 4mm) resulted in marginal improvement in Young's modulus and yield strength values. Table 4.10 presents the mechanical properties of Type-A variants in relation to varied thickness (t) and relative density ($\bar{\rho}$).

4.4.6.2 Stress-strain response and energy absorption characteristics

Fig. 4.15(a) shows stress-strain response of the Type-A variant lattice structure for different strut thickness. Despite different peak stress intensities, the pattern of peak and valley formation within the plateau regime was found to be similar as thickness increased from 1mm to 4mm. Fig. 4.15(a) is marked with numbers 1 to 4 to understand the localized deformation behavior of the structure in different rows of unit cells as the failure of lattice structure is localized and the crush bands percolate throughout the lattice with increase in strain. The point-1 represents the end of elastic regime and after point-1, the cells deform plastically giving a long plateau before reaching the densification. The difference in deformation pattern can be seen for thickness of 1mm, 2mm and 2.5mm and but after 2.5mm, the deformation patterns are found to be similar (Fig. 4.15(b)).

Cell collapse occurred either due to the formation of plastic hinge at the location of the maximum moment within the strut or due to the buckling of the strut when the load increased to its critical buckling load (Euler buckling load). When the thickness of added vertical strut is 1mm the elastic behavior of the Type-A variant was determined by buckling of the thinner vertical strut (Fig. 4.15(b)-point-1), while the plastic behavior within the localized band was determined by both types of failure mode (buckling and bending) as can be seen in Fig. 4.15(b)-point-2 to 4. Load resistance in buckling is lower than that of bending and both are dependent on $\frac{t}{l}$ ratio of deforming strut. Since at t = 1mm the load resistance during deformation by different vertical members was lower and hence lower stress response was obtained, which can be mapped with the Von Mises stress distribution within the deformed cells. An increase in thickness (to 2mm) changes the cell collapse behavior and was completely dominated by failure due to bending (formation of a plastic hinge) (Fig. 4.15(b)). Further increase in thickness (2.5mm to 4mm) adds an axial component of load with bending in the vertical strut which improves its load resisting capacity (Fig. 4.15(b)-point-3 and 4).

(a)

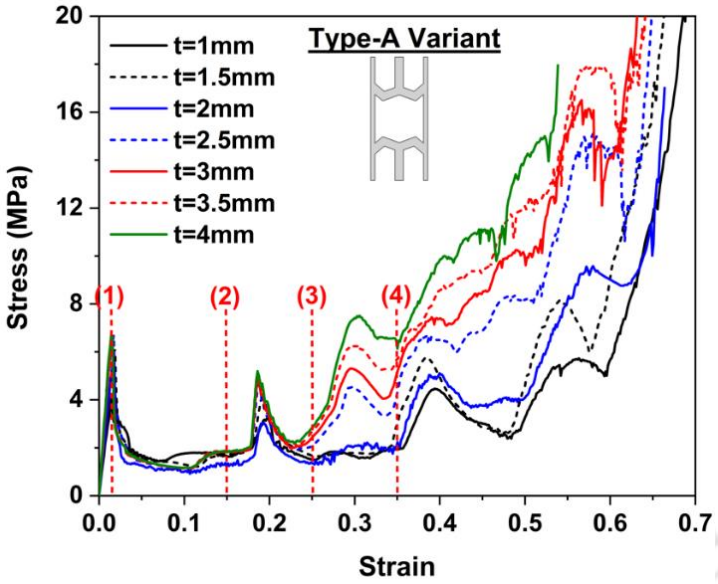

(b)

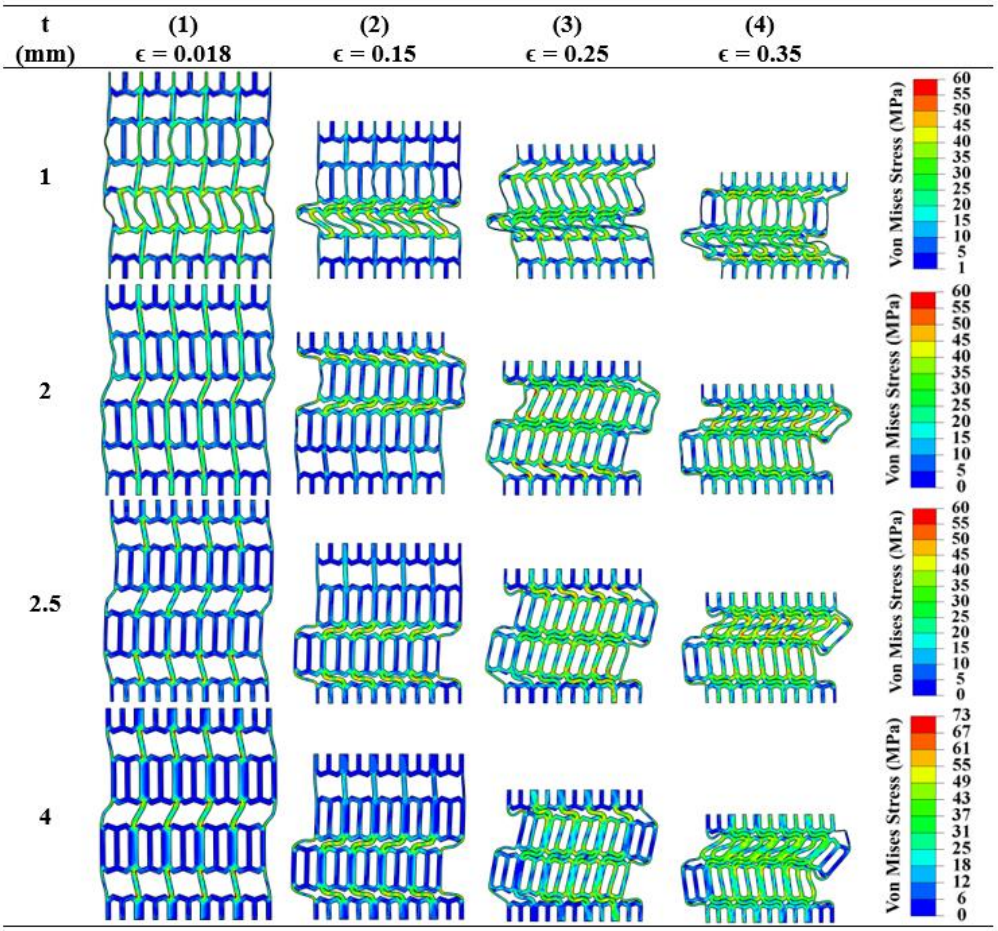

Fig. 4.15 Effect of added vertical strut thickness (t) for Type-A variant on (a) stress-strain response during quasi-static compression and (b) deformation sequences at different strains are correspondingly highlighted in the stress-strain curve

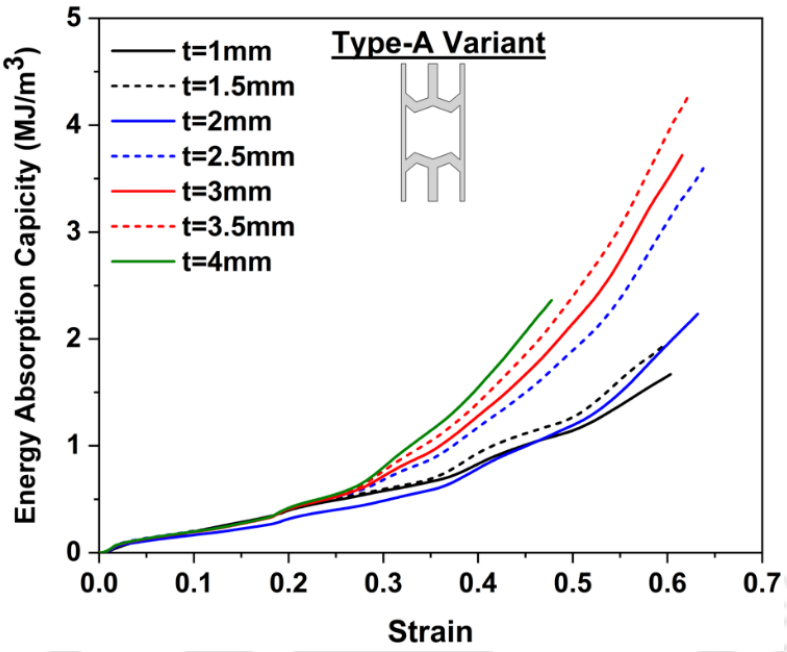

Fig. 4.16 Effect of variation of added vertical strut thickness (t) for Type-A variant structure on energy absorption capacity

Fig. 4.16 shows the variation of energy absorption capacity with strain. Initially, for strain up to 0.25, the energy absorption varies linearly with strain, and the influence of added vertical strut thickness was negligible. As the strain increases, the energy absorption capacity increases exponentially since the deformation of lattices was controlled by sub-cell-2 which is highly influenced by thickness variation of the vertical strut. As thickness changes the total energy absorption capacity of the Type-A variant structure increases and reaches a maximum value for t = 3.5mm. Further increase in thickness (i.e.4mm) leads to early cell collapse and is responsible for low energy absorption (Fig. 4.15(a)). Due to increase in the thickness, the distance between the walls becomes lesser which leads to early failure (due to early percolation of contacts between cell walls) and hence reducing the onset of densification which ultimately reduces the total energy absorption.

Table 4.11 summarizes the energy absorption characteristics of the Type-A variant. It can be noted that the energy absorption capacity of the structure increased from 1.67 MJ/ m^3 to 4.29 MJ/ m^3 as thickness was increased from 1mm to 3.5mm and reduced to 2.36 MJ/ m^3 for a thickness of 4mm. The maximum energy absorption capacity of the Type-A variant was observed for a thickness of 3.5mm. Similar behavior was observed with the SEA of the structure. The SEA increased from 4975.47 J/kg to 10230.02 J/kg as thickness increased from 1mm to 3.5mm and reduced to 5403.13 J/kg for a thickness of 4mm. The influence of added

vertical strut thickness on energy absorption efficiency is negligible and is between 30.73% to 33.99% for thickness of 1mm to 3.5mm except at 2.5mm which showed the highest efficiency (43.27%). It is thus clear that the thickness of vertical strut highly influences the mechanical behavior of Type-A lattice structure. However, orientation of the struts with respect to loading also affects it's loading capacity.

Table 4.11 Energy absorption characteristics of Type-A Variant structure

Properties	Thickness 't' (mm)						
	1	1.5	2	2.5	3	3.5	4
EA (MJ/ m^3)	1.67	1.94	2.41	3.60	3.72	4.29	2.36
SEA (J/kg)	4975.47	5534.63	6651.97	9366.27	9269.42	10230.02	5403.13
η (%)	33.37	32.38	43.27	33.99	30.73	31.75	24.11
ε_D	0.60	0.60	0.63	0.64	0.62	0.62	0.48
$\bar{\rho}$	0.32	0.33	0.35	0.37	0.38	0.40	0.42

4.5 Summary

In this study, a pair of novel 2D re-entrant auxetic lattices capable of exhibiting enhanced stiffness and energy absorption is proposed by introducing vertical ligaments into the Modified RH structure. These novel 2D re-entrant auxetic lattices were realized via fused deposition additive manufacturing. The deformation patterns and the energy absorption characteristics of 3D printed auxetic lattices under quasi-static compression were investigated via both Finite Element (FE) simulations and experiments. The effective elastic stiffness of the proposed lattices was theoretically estimated. The FE results corroborated by experiments, elucidate the role of different sub-cells on the effective mechanical properties of the proposed auxetic lattices. The results indicate that the proposed structures - Type A and B variants, exhibit enhanced stiffness (+355%) and superior energy absorption (+165%) in comparison to conventional 2D re-entrant lattices of the same mass. These structures outperformed among some of the recent state-of-the-art auxetic structures made up of ABS, PA12, PA6, PLA, TPU and CFRTPC polymers in terms of energy absorption capacity (Fig. 4.17). Furthermore, the findings of the study suggest that the strength, stiffness, energy absorption capacity and Poisson's ratio of 2D auxetic lattices can be tailored by tuning the sub-cell properties and cell wall thickness.

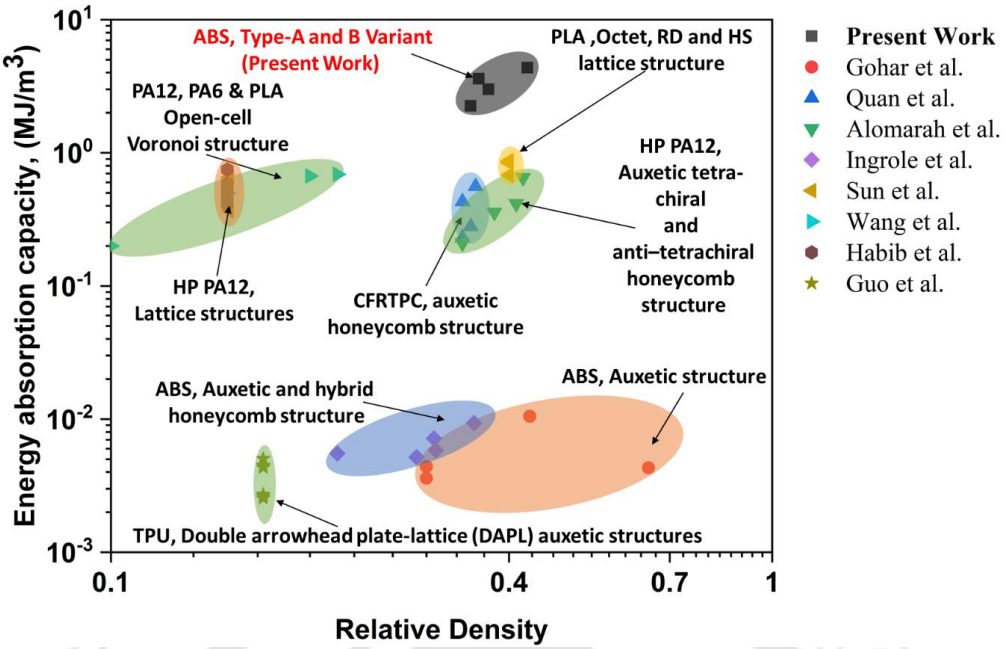

Fig. 4.17 Comparison of energy absorption performance of our developed auxetic re-entrant honeycomb structure with various polymeric foams available in literature [36, 57, 81–87]

Chapter 5 Tessellation controlled mechanical properties of 3D printed auxetic structures

This chapter discusses the effect of tessellation on the functional and mechanical properties of cellular structures. The Type-A variant (previous work) is considered as the base unit cell and various tessellation strategies are applied. The crushing performance of different tessellated lattice structures is studied through the numerical method and experiments. The effect of tessellation on the strength, stiffness, energy absorption capacity and Poisson's ratio are studied. [1]

[1]A portion of this chapter is submitted as:

Choudhry, N. K., Panda, B., Kumar, A & Kumar, S. Tessellation controlled mechanical properties of additively manufactured 2D lattice. Additive Manufacturing

5.1 Introduction

Tessellation is an arrangement of morphology; single or multiple; within the design space. It is derived from the Latin word ‘tessellare’, meaning ‘to pave’. It can be classified into three groups as periodic tessellation, stochastic tessellation and hierarchical tessellation [88][89]. In periodic tessellation, the unit cell of a lattice is translated in a given direction and shows repeatability while in stochastic tessellation the design space is filled randomly with the unit lattice cell/cells. On the other hand, in hierarchical tessellation, the design space is filled by recursive decomposition.

Periodic tessellation can be further classified into subgroups as; ‘edge-to-edge tessellation’, ‘non-edge-to-edge tessellation’ and ‘overlapping tessellation’. The edge-to-edge tessellation is capable of transferring uniform load from one side of the lattice structure to the other side due to the complete share of the edges of the unit cell of the lattice [88]. This leads to a wide application of edge-to-edge tessellation. In nature, there are many examples of 2D tessellation where edge-to-edge tessellation is exhibited such as the nest of a honeybee which is used for storage purposes [90], endoskeleton of ray fishes or sharks for protection purposes [91], etc. On the other hand, in non-edge-to-edge tessellation, there is a partial sharing of edges of the unit cell of a lattice structure is exhibited which leads to a non-uniform transferring of loads from one side of the lattice structure to the other side, and are capable of inducing different mechanical and functional properties. Some examples of 2D non-edge-to-edge tessellation are Bouligand structures [92], cuticles of beetles [93], etc. In overlapping tessellation, the edge of the unit cell of the lattices overlapped, and is seen in nature such as in the scales of the fish, peacock’s feathers, etc.

Though tessellation highly impacted the mechanical and functional properties of the lattice structures but still very little research has been done. A numerical model has been used to study the auxetic behavior of 3D non-edge-to-edge tessellated structures called ‘bucklicrystals’ by Babaee et al. [94] which was later extended by Yuan et al. [95] by using TPU as a base material. Bhat et al. [96] studied the effect of atomic tessellation on additively manufactured PA-12 lattice structures in terms of mechanical and structural behavior of the lattices.

In other words, there is a need to study different tessellation strategies such as ‘edge-to-edge’ ‘non-edge-to-edge’ and ‘overlapping’ tessellation and its impact on structural and functional properties that can address a wide area of engineering applications. Hence in this work, the same unit cell has been taken and a comparative study was performed between ‘edge-

to-edge' 'non-edge-to-edge' and 'overlapping' tessellation in terms of mechanical performance. Inspiration is drawn from nature where the same lattice has arranged to achieve different functionalities.

5.2 Design details of periodic tessellation

A unit cell is the basic building block of cellular structures which is an interconnected network of surfaces or struts. The required functional and mechanical properties of the cellular structures are dependent on the morphology of the unit cell. Type-A variant is considered as base unit cell as this unit cell has been designed for better structural and energy absorption properties. The main objective of the current study is to observe the effect of tessellation on the structural and functional properties of cellular structures. For this purpose, various tessellation strategies were designed in Solid work by importing the unit cell. Fig. 5.1 shows the classification and design details of periodic tessellation based on connectivity.

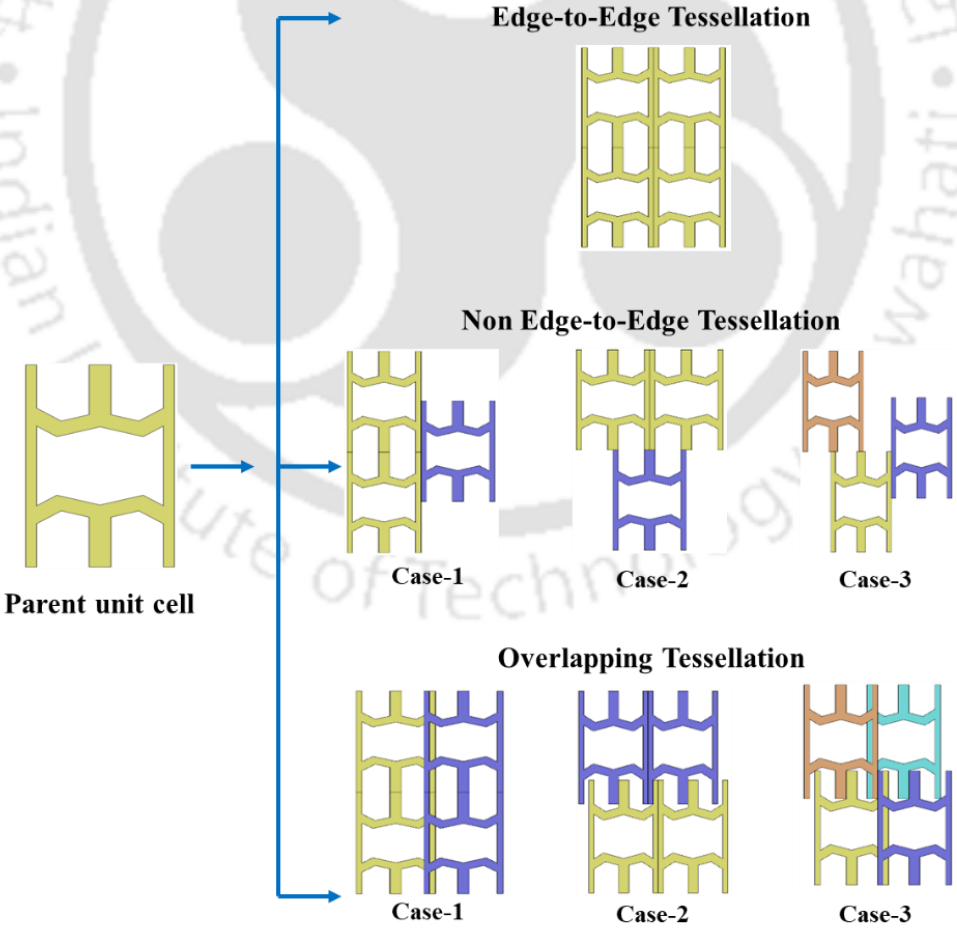

Fig. 5.1 Classification and design details of periodic tessellation based on connectivity

5.3 Result and discussion

5.3.1 Stress-strain response and deformation mechanism

Fig. 5.2 shows a stress-strain curve of all different tessellated lattice structures. On the right-hand side of Fig. 5.2 comparison between the FE predictions with the experimentally measured stress-strain response for one tessellated structure from each group is shown. For all tessellated lattice structures deformation stages are the same; in the beginning, a linear elastic response is observed followed by a plateau regime and finally the densification regime. To understand the crushing performance of the tessellated lattices, the stress-strain curve of tessellated lattice structures (right-hand side of Fig. 5.2) is marked with numbers to signify its deformation behavior at different stages during compression. Table 5.1 represents the sequential deformation maps during quasi-static compression at the corresponding points shown in the stress-strain curve.

Elastic deformation- For all the tessellated lattice structures, initially, there is a linear increase in stress, as the cells of the structure deformed uniformly and elastically due to the instant stress distribution throughout the structure (as an absence of instabilities like larger bending or buckling) [80]. As stress increase to its maximum value (at the end of the elastic regime), within the tessellated lattice structures, there is a point that starts deforming plastically first (it is different for different cases of tessellation), and finally the layer having this first plastically deformed point starts deforming plastically. After entering into the plastic deformation zone, all lattices start deforming differently which is explained separately in the upcoming paragraphs.

Plastic deformation of Edge-to-Edge tessellation- The point after which stress started dropping is marked as the yield point (point-1). After the yield point, the deformation of structures was controlled by the sub-cell behaviour. Since the low relative density sub-cell is weaker than high relative density, initially the low relative density sub-cells were collapsed (point-3 & 4). The cells near the top and bottom plates encounter frictional resistance arising from contacting surfaces and leads to in-plane buckling of the structures (point-1). The sub-cell having lower relative density and away from the top and bottom plates is more unstable, deformed first. Thereafter, deformation moved to the other lower relative density cells, near to the top and bottom plates (as per their stability. Once all the lower relative density sub-cells were deformed, the deformation wave moved to the higher relative density sub-cells and continued till all the cells got collapsed.

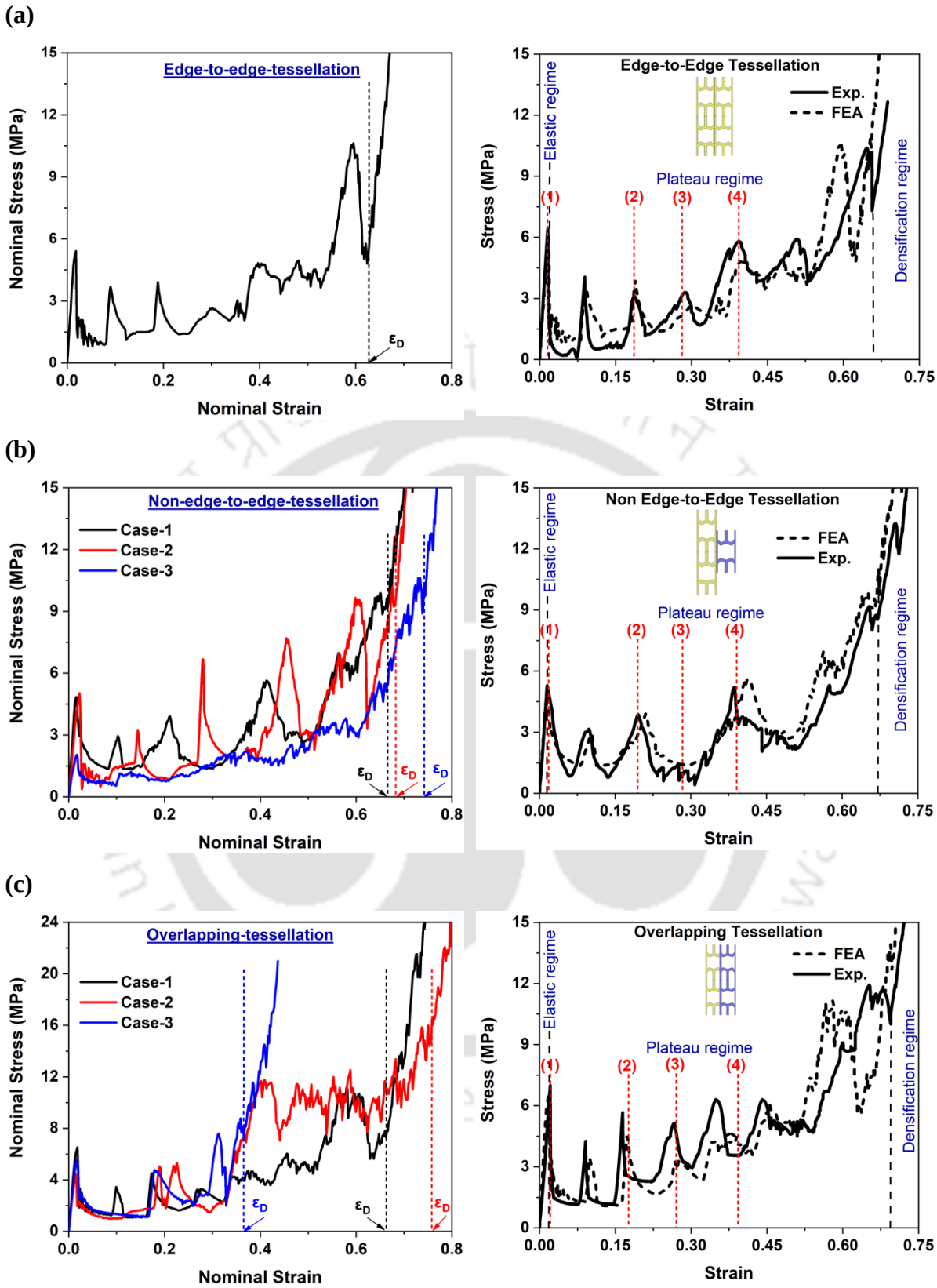

Fig. 5.2 Comparative analysis of tessellated structures; stress-strain curves and sequential deformation maps; (a) Edge-to-Edge tessellation, (b) Non Edge-to-Edge tessellation and (c) Overlapping tessellation

A fall in the stress was observed during the deformation of one unstable layer (sub cell), and it continued till complete layer deformed. Due to complete deformation of the layer, the stability of complete structure further increases which resisting more load (a sharp increase in stress) till another layer becomes unstable. This cyclic behavior of stress (increasing and decreasing) continues till all the rows got collapsed. Edge-to-Edge tessellation showed layer-wise deformation of the lattice structure which is the ideal requirement for the bending dominated lattice structure (Table 5.1). Finally, densification started at the point when all the rows of the structures got collapsed. After densification, compaction of layers due to compression loading continues and hence the stress values increase rapidly. It may be noted that within the compaction phase the performance is determined by the parent material and not by the structure [35].

Plastic deformation of Non Edge-to-Edge tessellation- there is three different arrangement of the unit cell lattice in Non edge-to-edge tessellation. These three Non edge-to-edge tessellated lattice structures are termed as Case-1, Case-2 and Case-3. As only partial shearing of edges or surfaces takes place within the Non edge-to-edge tessellated lattice structures, the distribution of forces and deformation wave depends on how these unit cells are partially connected. The stress-strain response of all three Non edge-to-edge tessellated lattice structures is shown in Fig. 5.2(b).

Table 5.1 Deformation sequential maps of different Tessellated structures

(1) ε = 0.018	**(2) ε = 0.17**	**(3) ε = 0.27**	**(4) ε = 0.40**	
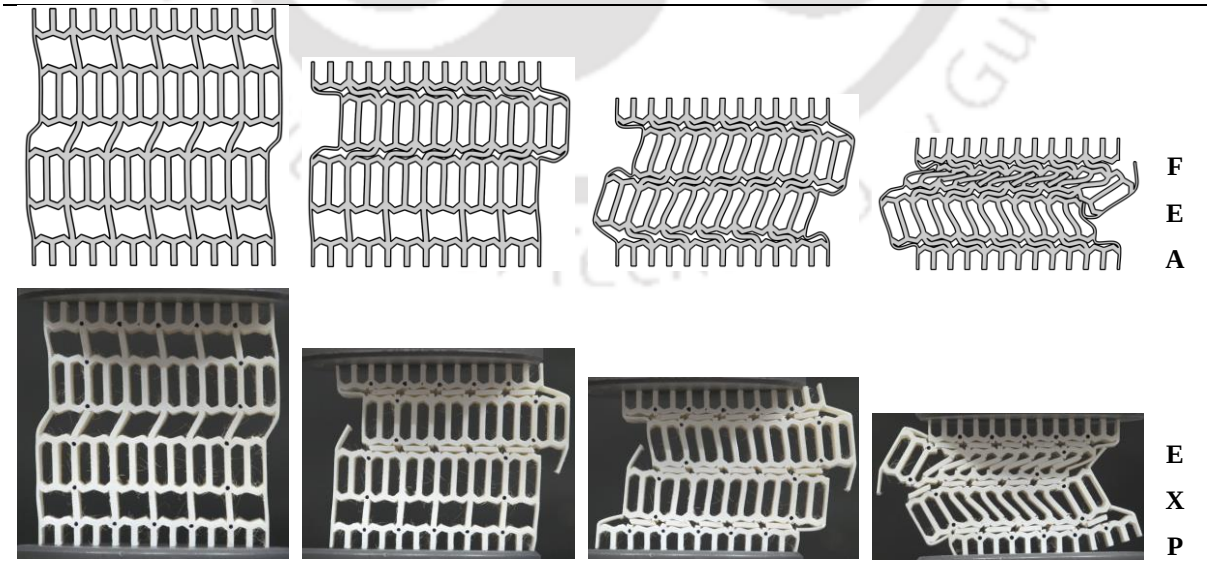				**FEA**
				EXP

Edge-to-Edge Tessellation

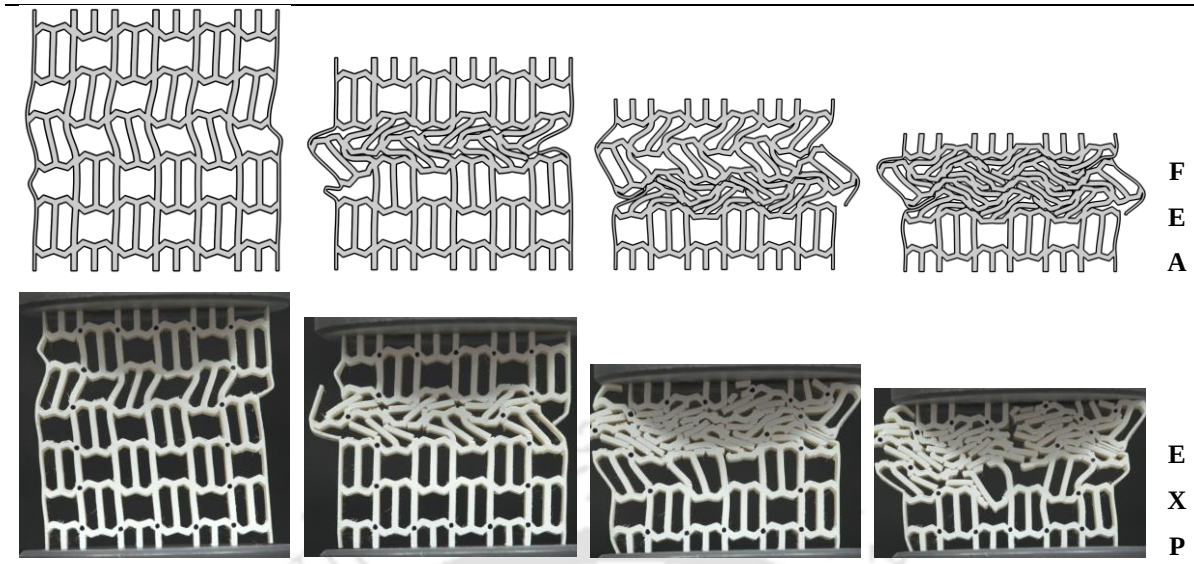

Non Edge-to-Edge Tessellation

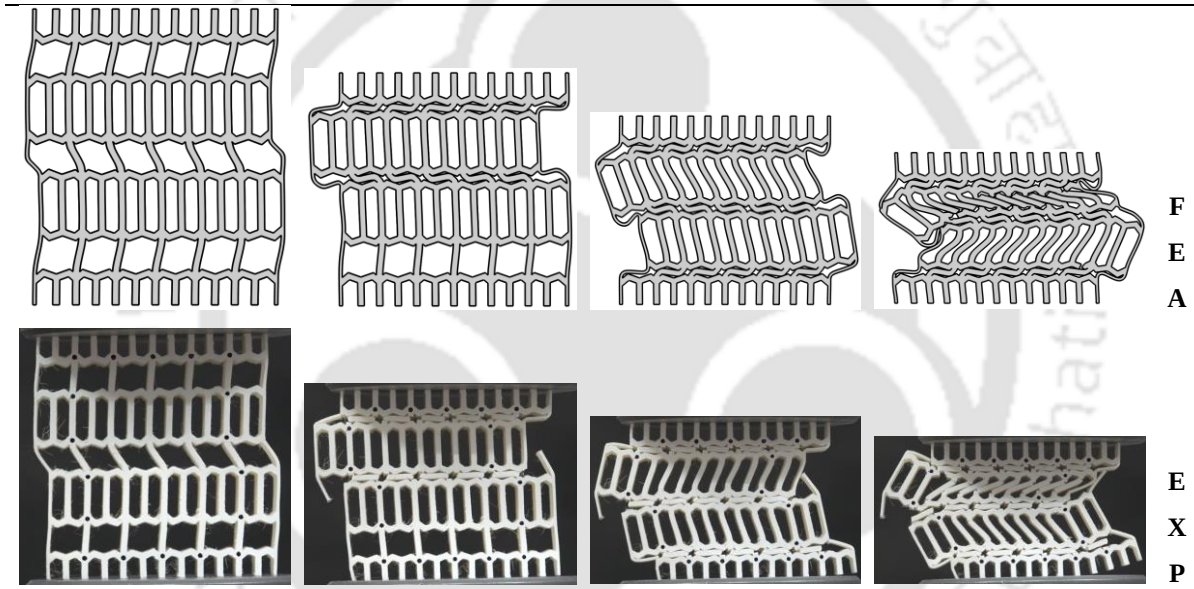

Overlapping Tessellation

In Case-1 of Non edge-to-edge tessellation, the right edge of the unit cell is partially sheared with the left edge of the next unit cell leading to an alternating arrangement of the higher and lower density sub-cells throughout the row (Table 5.2 (Case-1)). This arrangement of the subcells gives a uniform distribution of lower and higher-density subcells throughout the lattice structure. As the lattice structure enters into the plateau region, due to more instability at the center of the lattice structure (the cells near the top and bottom plates encounter frictional resistance arising from contacting surfaces and leads to in-plane buckling of the structures, and hence the center of the lattice structure becomes more unstable), the central row started deforming first. Initially, the lower density subcell near the center of the structure deforms first (Table 5.2, Case-1, $\varepsilon = 0.018$) and thereafter nearby locally higher

Table 5.2 Deformation sequential maps of Non edge-to-edge tessellated lattice structures

Strain (ε)	Case-1	Case-2	Case-3
0.00	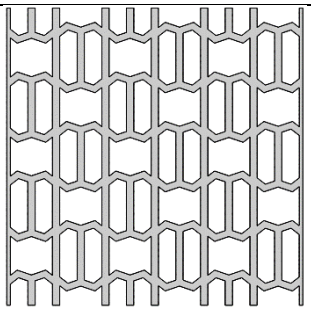	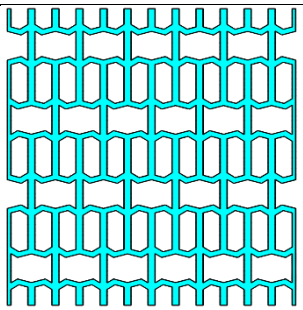	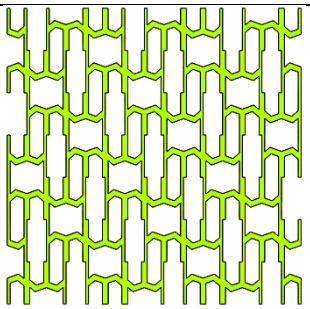
0.018	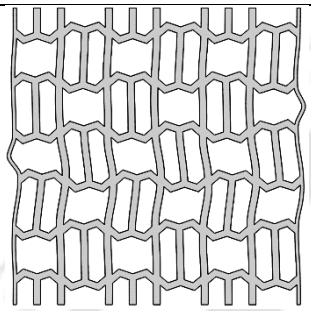	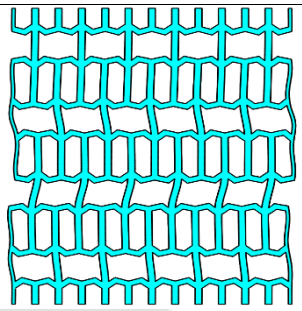	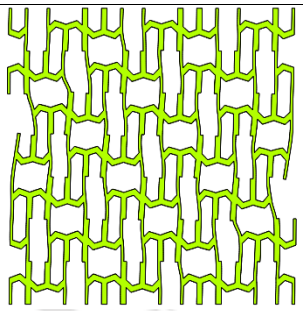
0.10	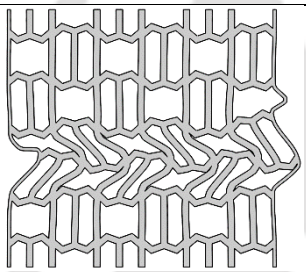	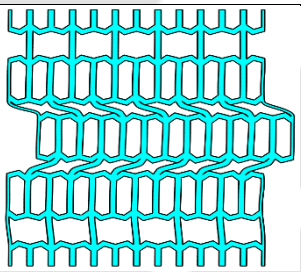	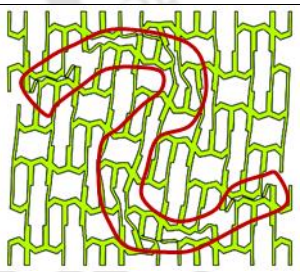
0.20	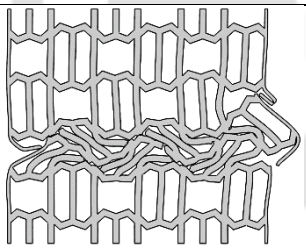	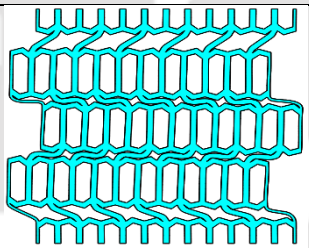	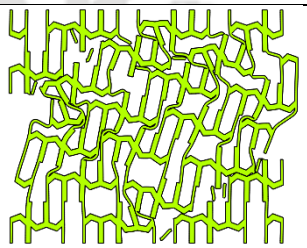
0.30	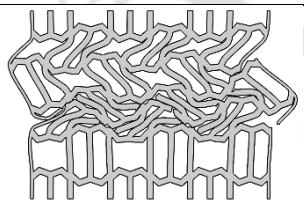	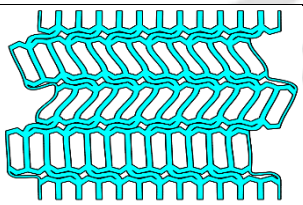	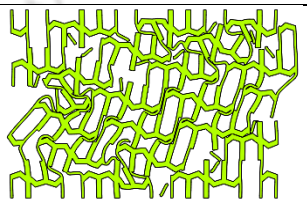
0.40	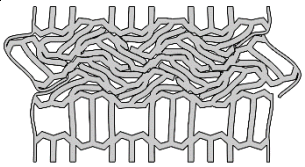	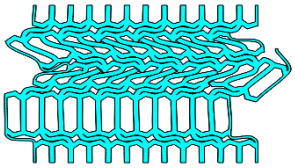	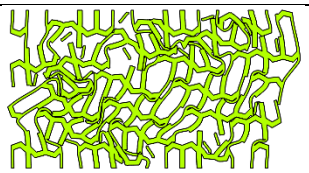
0.50	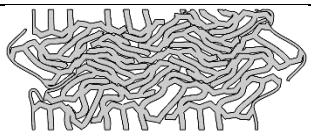	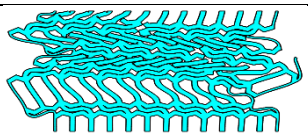	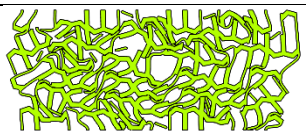

density sub-cells (Table 5.2, Case-1, ε = 0.1). In this way, deformation waves move from the center of the lattice structure to both directions gradually (top and bottom) (Table 5.2, Case-1, ε = 0.2 to 0.5) till it reaches the onset of densification.

In Case-2 of Non edge-to-edge tessellation, the bottom edge of the unit cell is partially sheared with the top edge of the below unit cell which leads an alternate arrangement of higher and lower density rows (due to higher and lower density subcells respectively) throughout the lattice structure (Table 5.2 (Case-2)). This type of arrangement of subcells is similar to edge-to-edge tessellation, and hence lattice structure showed a similar stress-strain response and deformation pattern as that of edge-to-edge tessellation (Table 5.2, Case-2, ε = 0.00 to 0.5).

In Case-3 of Non edge-to-edge tessellation, since both the edges of the unit cell of the lattice structure are partially shared with the other unit cell, which leads to variation in the thickness of the ligaments of the lattice structure (not seen in Case-1 and Case-2; thickness of ligaments remains same throughout the lattice structure), and hence subcells with variable thickness are found. These subcells are uniformly distributed throughout the lattice structure. Initially, at the beginning of plastic deformation, the lattice starts deforming throughout the structure at the lower wall or ligament thickness (Table 5.2, Case-3, ε = 0.018), and as crushing continued the "S" type of deformation pattern formed (Table 5.2, Case-3, ε = 0.1). Further crushing leads the deformation of subcells near the diagonal of the lattice structure at both corners and continued till both corners collapsed (Table 5.2, Case-3, ε = 0.2 to 0.5).

Plastic deformation of overlapping tessellation- there is three different arrangement of the unit cell lattice in overlapping tessellation. These three overlapping tessellated lattice structures are termed as Case-1, Case-2 and Case-3. The stress-strain response of all three overlapping tessellated lattice structures is shown in Fig. 5.2(c).

In Case-1 of overlapping tessellation, due to the overlapping of the right edge of the left unit cell with the left edge of the right unit cell, there is a marginal increase in the thickness of the outer left and right walls of the unit cell but others parameter remains constant and hence overlapped lattice structure behaves similar to the edge-to edge tessellation (Table 5.1). The stress-strain response and deformation maps of Case-1 are shown in Fig. 5.2(c) and Table 5.1 respectively.

In Case-2 of overlapping tessellation, due to the overlapping of the bottom ligaments of the top unit cell to the top ligaments of the bottom unit cell, the thickness of overlapped ligaments becomes twice as that of other other ligaments. However, still, two subcells are formed with different densities. The subcell of lower and higher density is arranged in a row

Table 5.3 Deformation sequential maps of overlapping tessellated lattice structures

Strain (ε)	Case-1	Case-2	Case-3
0.00	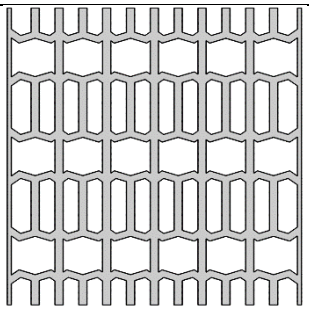	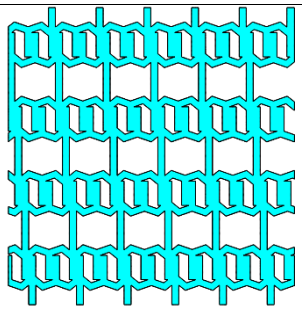	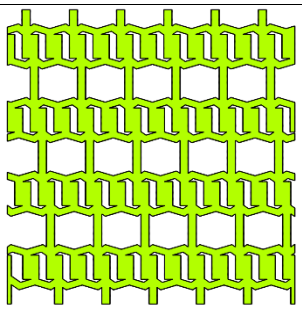
0.18	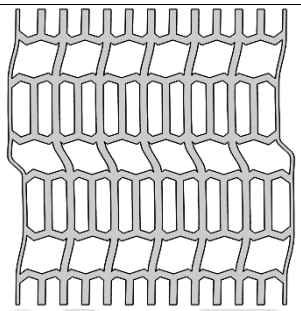	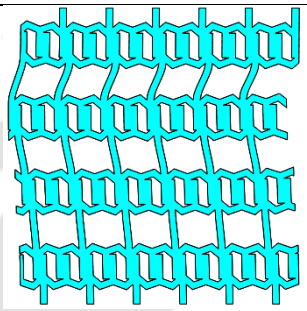	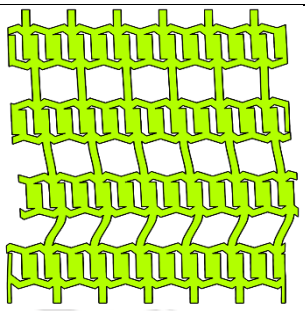
0.10	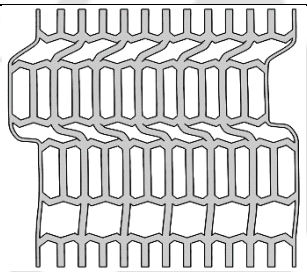	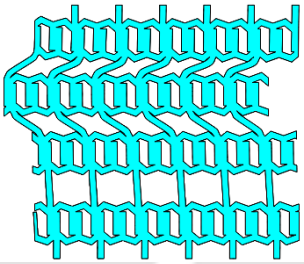	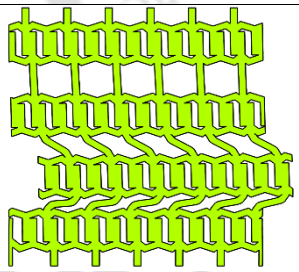
0.20	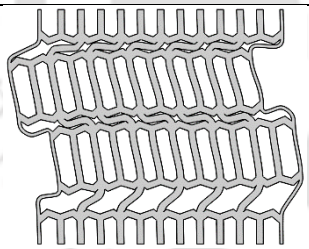	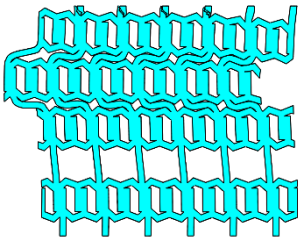	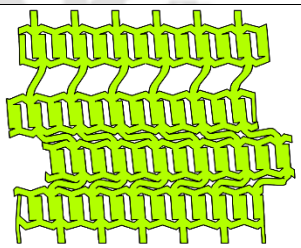
0.30	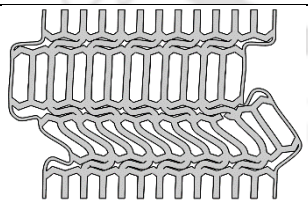	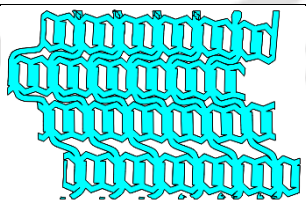	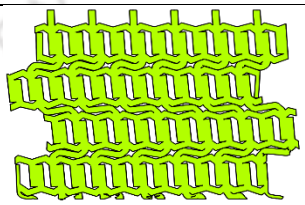
0.40	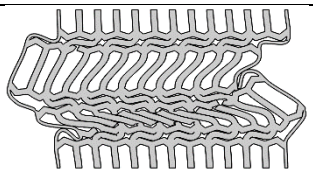	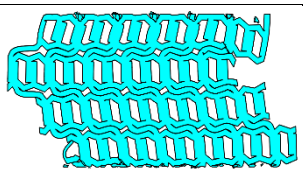	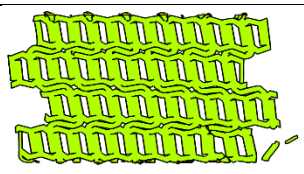
0.50	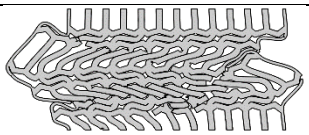	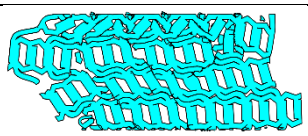	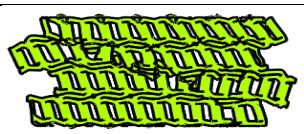

leading to an alternate layer of rows with lower and higher densities. This type of arrangement of lower and higher-density rows allows the deformation of lower row density first, once all lower-density rows collapsed then the deformation of higher-density rows starts (Table 5.3, Case-2, ε = 0.0 to 0.5).

In Case-3 of overlapping tessellation, here overlapping of both the side of ligaments i.e top & bottom and left & right took place due to which variation in the thickness of ligaments was found. Two subcells with different densities are formed. The subcell of lower and higher density is arranged in a row leading to an alternate layer of rows with lower and higher densities. Similar deformation maps are formed as that of Case-2, but due to higher density than that of Case-2, it reaches early to the onset of densification strain (Fig. 5.2(c)). It has been observed that as all lower-density rows collapsed further crushing of the lattice structure led to a shear failure (Table 5.3, Case-3, ε = 0.5) of the lattice structure which was not observed in any other case of the tessellation.

5.3.2 Young's modulus and yield strength

Elastic modulus and Yield strength [33] determine the bearing capacity of a structure. Fig. 5.3 (a and b) shows the comparative analysis of the elastic behavior of the structures in terms of Young's modulus and Yield strength. It is found that Young's modulus of Overlapping tessellation of Case-1 structure (450.43 MPa) is the highest among all the tessellated structures which indicates that it possesses strong support ability during small deformation, while Case-3 of non-edge-to-edge tessellation structure (157.93 MPa) has lowest Young's modulus. The yield strength of the Overlapping tessellation of Case-1 structure (6.52 MPa) is superior to other Tessellated structures, and therefore, it has very good resistance to an external force. The least yield strength is 2.04 MPa which is shown by Case-3 of non-edge-to-edge tessellated structure as this lattice structure possed variable wall thickness having least wall thickness of 1mm which is at least half than that of other tessellated lattice structure. The elastic behavior of all lattice structures under quasi-static compression is shown in Table 5.4. These properties are measured from simulation results. It can be noted from Table 5.4 that the Case-1 of Overlapping tessellation showed the highest Young's modulus and Yield strength than that of other tessellations which indicates that it has better resistance to external forces and have a stronger support ability under small deformation.

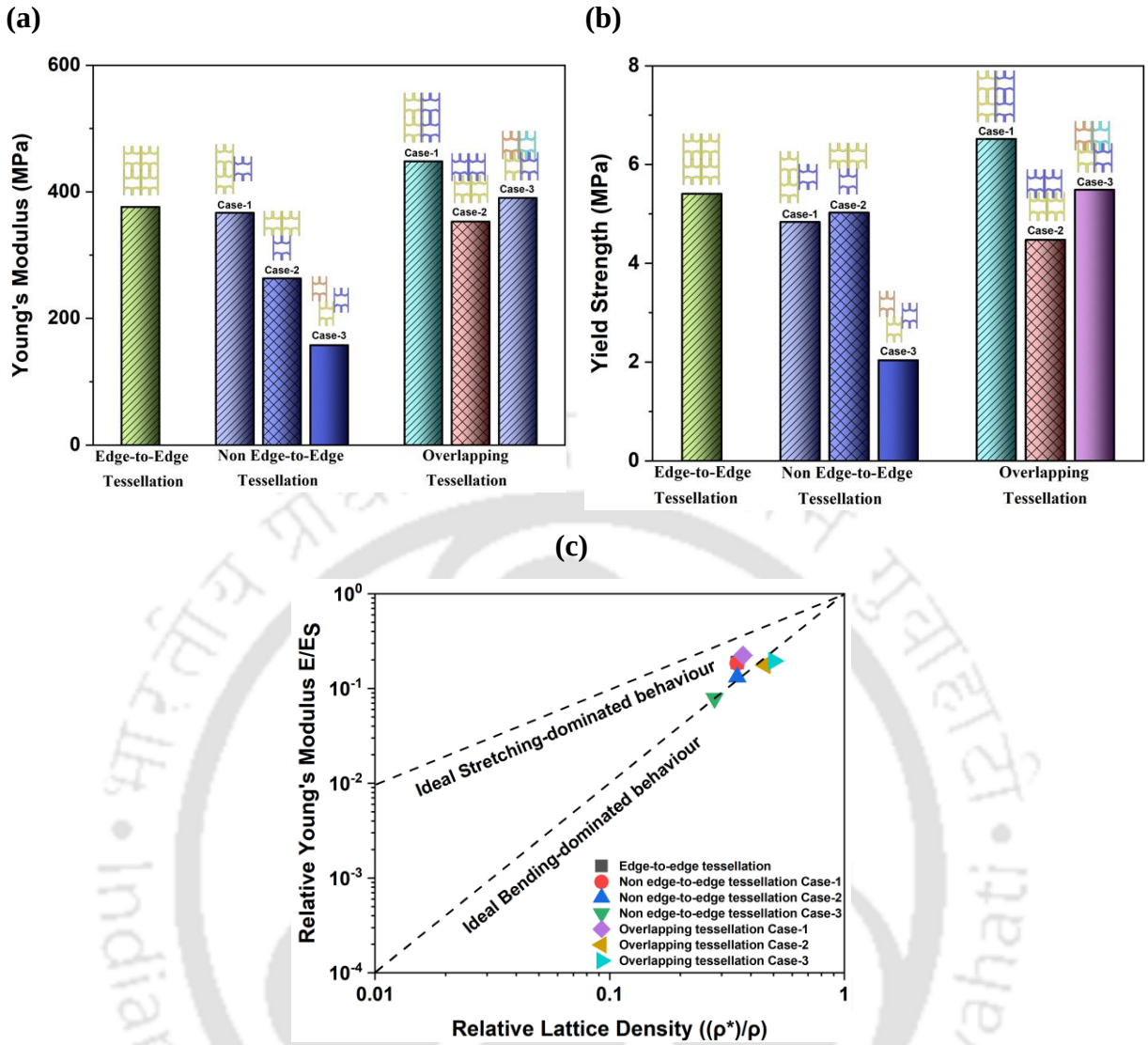

Fig. 5.3 Comparative analysis of properties; (a). Young's modulus, (b) Yield strength and (c) relative Young's modulus

Fig. 5.3(c) shows the scaling relation between Young's modulus and the relative density for all tessellated lattice structures. Relative Young's modulus for the tessellated lattice structures is calculated by dividing the Young's modulus of the tessellated lattice structures to the Young's modulus of the base material (ABS polymer; E_s = 2000MPa). As per the Ashby model [8, 75], approximated relation for open-cell cellular structures for relative Young's modulus to relative lattice density is given by equation 5.1.

$$\frac{E}{E_S} = C\left(\frac{\rho^*}{\rho}\right)^n \tag{5.1}$$

Where E and E_S are Young's modulus of cellular structure and its base material respectively, and ρ^* and ρ are the densities of cellular structure and its base material respectively while C and n are the geometric constants of proportionality and exponent of the

Ashby model respectively. As per the Gibson-Ashby model, the fitting exponent n for Young's modulus is 1 for stretch-dominated structures and 2 for bending-dominated structures [76, 77], respectively.

Equation 5.1 is used to obtain the scaling relation between Young's modulus and the relative density for all tessellated lattice structures, and the value of the geometric constant of proportionality C and exponent n are obtained. The geometric constant of proportionality C for all tessellated lattice structures is in the range of 0.679 to 0.885, while the exponent m is in the range of 1.48 to 1.79 which means all tessellated lattice structures show bending-dominated deformation behavior. Fig. 5.3(c) also suggests that all the tessellated lattices are having bending-dominated deformation behavior. Many of the tessellated lattice structures are at the ideal bending-dominated deformation line while few of them are in between the ideal bending-dominated deformation and ideal stretching-dominated deformation zone.

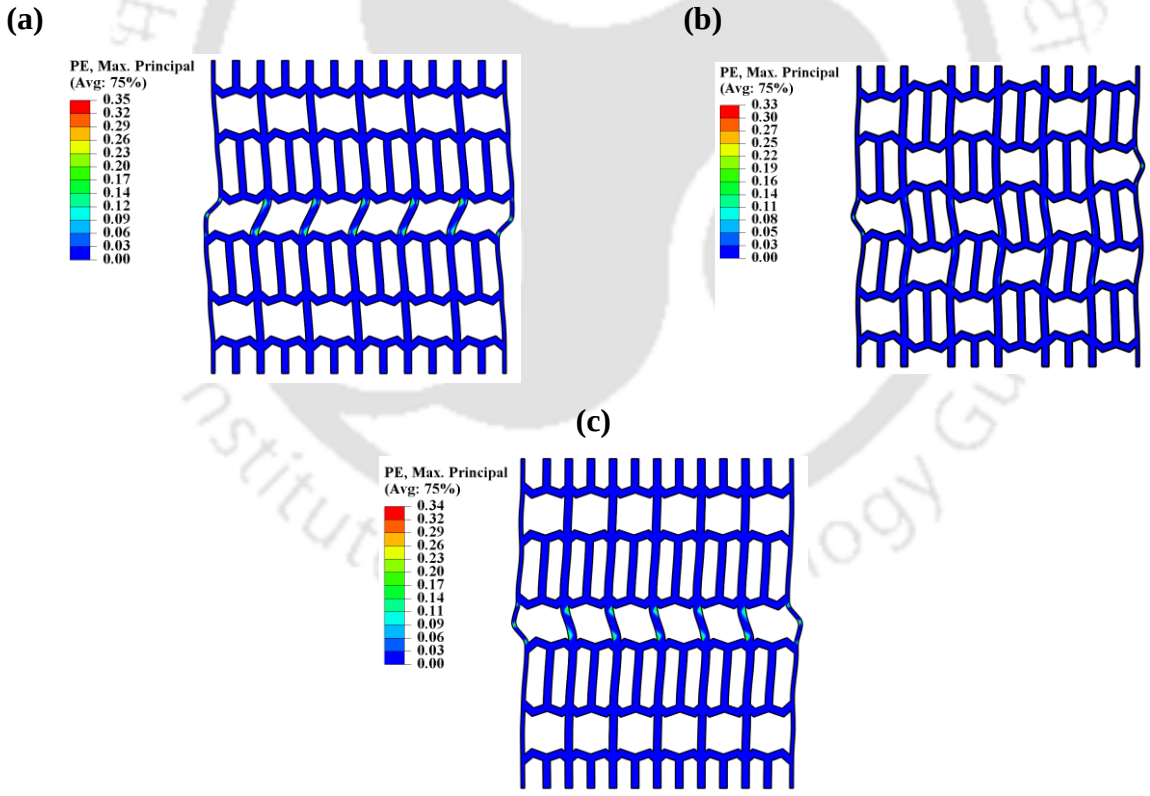

Fig. 5.4 End of elastic behavior of tessellated structure due to start of plastic deformation of the different ligaments at different locations within the structure; (a) Edge-to-Edge tessellation, (b) Non Edge-to-Edge tessellation and (c) Overlapping tessellation

The yield strength of a lattice structure is the ability of a structure to withstand maximum stress before showing plastic deformation and is measured at the end of the elastic region. The elastic region ends when some of the ligaments start deforming plastically as shown in Fig. 5.4. As within the elastic region lattice structures deform uniformly and hence distribute uniform load throughout. These loads are responsible for stress generation within the ligaments of the cells. When stress generated within the ligament goes beyond its critical load it starts deforming plastically. Due to tessellation, lattices have different wall thicknesses at different locations of the ligaments, and hence the ligament or some portion of the ligament which have a lower wall thickness is critical.

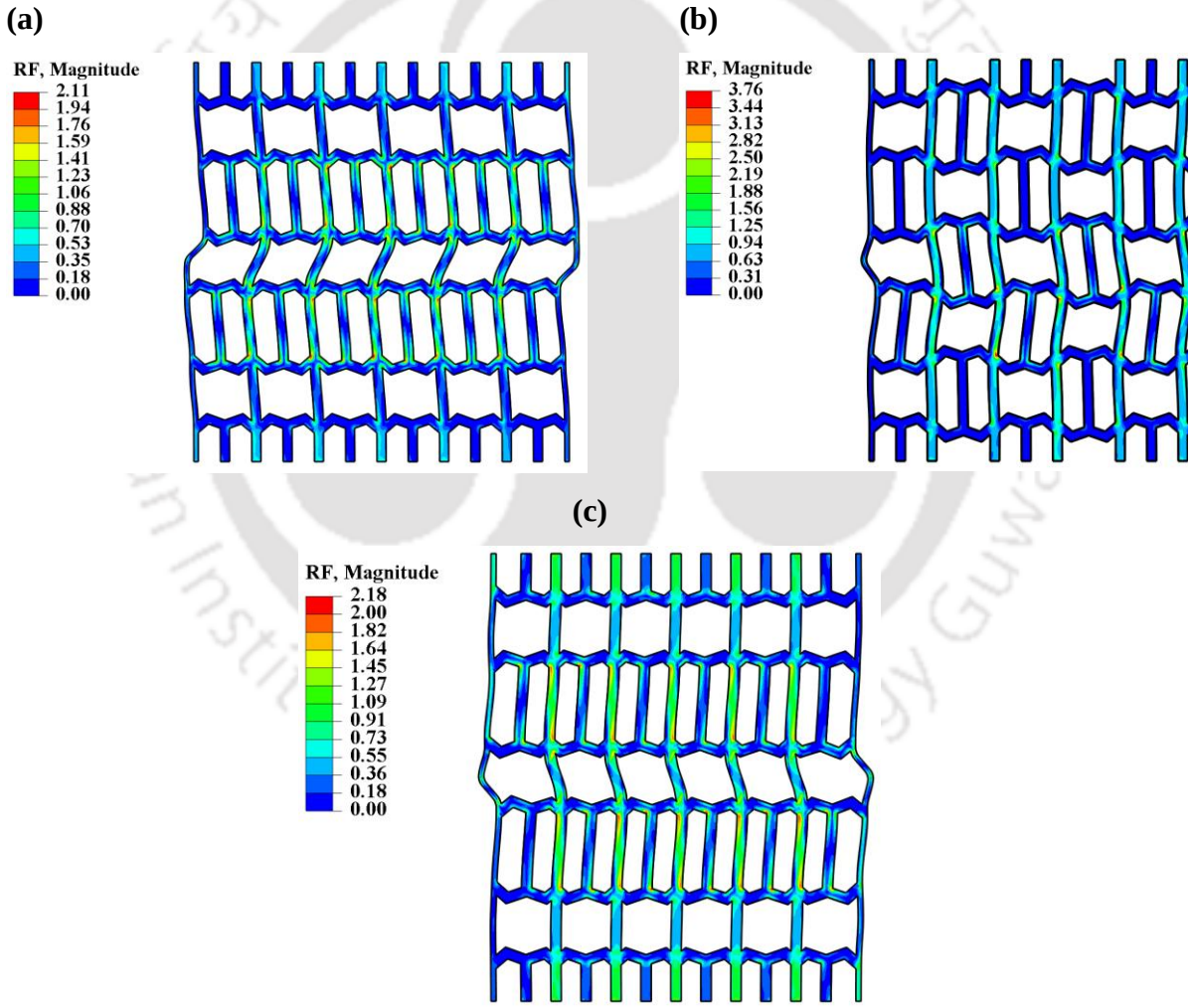

Fig. 5.5 Reaction forces (RF) induced within the ligaments at the end of the elastic region; (a) Edge-to-Edge tessellation, (b) Non Edge-to-Edge tessellation and (c) Overlapping tessellation

When structures start deforming elastically initially forces are directly transferred to the other end through the vertical ligaments which leads to a sharp increase in the stress-strain curve at the beginning. Further loading causes elastic deformation of the material of the ligaments causing the generation of internal forces within it. As generated forces increase beyond the elastic value it starts deforming plastically. Fig. 5.5 shows reaction forces (RF) induced within the ligaments at different positions at the end of the elastic region.

Table 5.4 Mechanical properties of structures under quasi-static compression

Tessellation		Elastic modulus (MPa)	Yield strength (MPa)
Edge-to-edge tesselation		376.3	5.41
Non edge-to-edge tesselation	Case -1	367.05	4.84
	Case -2	263.51	5.03
	Case -3	157.93	2.04
Overlapping tesselation	Case -1	448.35	6.52
	Case -2	353.15	4.48
	Case -3	390.69	5.49

5.3.3 Poisson's ratio

Fig. 5.6 shows Poisson's ratio versus nominal strain curves for all tessellated lattice structures compressed quasi-statically till 0.1 strain. As Poisson's ratio is geometry dependent [78, 79] properties it is highly affected by changing the geometric parameters. The basic unit cell used for the study of the tessellation effect is auxetic having a negative Poisson's ratio (NPR) of -0.121 but due to different tessellations, their geometric parameters changed (Fig. 5.1), and hence their Poisson's ratio.

Out of all tessellated lattice structures, three structures exhibited auxetic behavior while four structures exhibited non-auxetic behavior. For all auxetic tessellated lattice structures, a similar pattern for variation in Poisson's ratio with strain was observed; in the early stages of loading, their NPR increases and becomes maximum, thereafter, further compression causes a decrease in the NPR. On the other hand, all non-auxetic tessellated lattice structures showed the same trend for Poisson's ratio variation with strain; in the early stages of loading, their

Poisson's ratio increases and becomes maximum, thereafter, further compression causes a decrease in the Poisson's ratio.

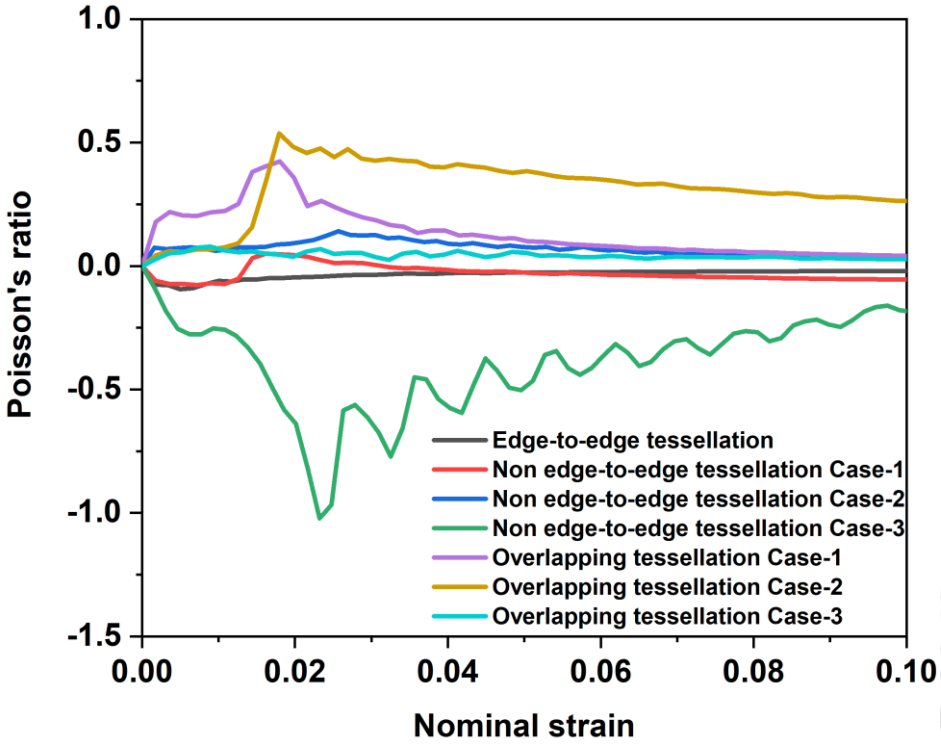

Fig. 5.6 Poisson's ratio versus nominal strain curve of all tessellated lattice structures

There is a variation in the auxeticity of tessellated lattice structures, and 'Non edge-to-edge tessellation Case-3' lattice structure showed the highest auxeticity than that of the 'edge-to-edge tessellation' and 'Non edge-to-edge tessellation Case-1' lattice structure with a Poisson's ratio of -1.022, -0.121 and -0.116 respectively. Similarly, there is a variation in the non-auxetic behavior (i.e. positive Poisson's ratio) of tessellated lattice structures, and the 'Overlapping tessellation Case-2' lattice structure showed the highest positive Poisson's ratio than that of the 'Overlapping tessellation Case-1', 'Overlapping tessellation Case-3' and 'Non edge-to-edge tessellation Case-2' lattice structures with a Poisson's ratio of 0.538, 0.425, 0.172 and 0.141 respectively.

5.3.4 Energy absorption

Comparisons of energy absorption capacities of all tessellated lattice structures under quasi-static compression are presented in Fig. 5.7(a). The deformation and failure characteristics of a lattice structure play a vital role in determining the energy absorption performance of the lattice. The stress-strain response and deformation maps of the tessellated

lattice structures are discussed in detail in section 5.3.1. Initially, for all the tessellated lattice structures, the EA curves coincide and vary linearly with a lower slope up to strain value 0.2, which suggests that the energy absorption rate of the tessellated structures at lower strain is low. Among all tessellated lattice structures up to strain value 0.2, 'Overlapping tessellation Case-3' showed the highest slop of EA curve while 'Non edge-to-edge tessellation Case-3' showed the least slop of EA curve and hence had the highest and lowest energy absorption rate respectively. Further increase in strain leads to higher energy absorption of the tessellated structures with different rates. The energy absorption of the 'Overlapping tessellation Case-2' is the highest among all tessellated lattice structures while 'Non edge-to-edge tessellation Case-3' lattice structure has the least energy absorption capacity.

The specific energy absorption (SEA) of all the tessellated lattice structures is shown in Fig. 5.7(b). The specific energy absorption (SEA) of all the cases of 'Non edge-to-edge tessellation' and 'overlapping tessellation' is higher than that of the 'edge-to-edge tessellation'. The specific energy absorption (SEA) of all the cases of 'Non edge-to-edge tessellation' is the same (~6400 J/kg) which is ~16.36 % more than Edge-to-edge tessellation (~5500.36 J/kg). The SEA of 'Overlapping tessellation Case-2' structure is the highest (~ 10495.35 J/kg) amongst all the tessellated lattice structures and is ~ 90.81 % more than 'Edge-to-edge tessellation' (~5500.36 J/kg).

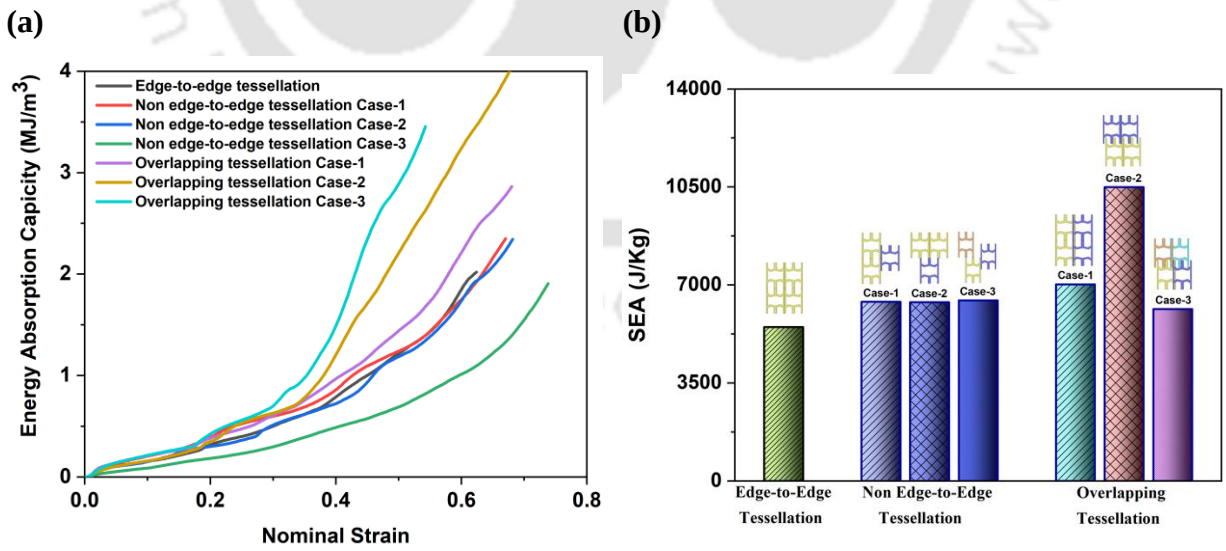

Fig. 5.7 Energy absorption characteristic of all tessellated lattice structures under quasi-static compression; (a) energy absorption capacity and (b) specific energy absorption capacity

5.4 Summary

In this study, the unit cell from our previous work (Type-A variant) is considered the base unit cell, and different tessellation strategies such as 'edge-to-edge' 'non-edge-to-edge' and 'overlapping' tessellation are applied. The effect of tessellation on the mechanical properties of cellular structures is studied. Various tessellation strategies were designed in Solid Works by importing the unit cell. The deformation patterns and the energy absorption characteristics of tessellated lattice structures under quasi-static compression were investigated through Finite Element (FE) simulations. One tessellated structure from each group is 3D printed and experimentally tested. Numerical results are validated by comparing them with the experimental results. The FE results corroborated by experiments, elucidate the role of tessellation on the effective mechanical properties of the tessellated lattices. The results indicate that the Case-1 of Overlapping tessellation showed the highest Young's modulus and Yield strength than that of other tessellated structures which indicates that it has better resistance to external forces and has a stronger support ability under small deformation. While the 'Overlapping tessellation Case-2' structure showed the highest SEA amongst all the tessellated lattice structures. Furthermore, the findings of the study suggest that the strength, stiffness, energy absorption capacity and Poisson's ratio of 2D auxetic lattices can be tailored by applying different tessellation strategies.

Chapter 6 Crushing behavior of cementitious composites reinforced with 3D printed auxetic structures

This chapter discusses the crushing performance of cementitious composites. Cementitious composites are developed by reinforcing the 3D-printed polymeric auxetic structures within the plain mortar. Four auxetic lattice structures including the Type-A variant (previous work) are considered in this study as mortar reinforcement. The effect of Poisson's ratio on peak compressive strength, ductility and energy absorption capability were examined. Based on the modified Hashin-Shtrikman model, Young's modulus of the LRCC specimens was estimated[1].

[1]A portion of this chapter is submitted as:

Choudhry, N. K., Nguyen, T. K., Panda, B. & Tran, P. Crushing behavior of cementitious composites reinforced with 3D printed auxetic lattice structures: Experiments and modelling. Cement and Concrete Composites

6.1 Introduction

Concrete is a widely used building material but it is subjected to many limitations in engineering applications because of poor ductility, high brittleness, low tensile strength and lower failure strain [97]. Therefore, reinforcement is necessary to ensure structural load capacity and reliability of concrete structures. This paper seeks to contribute to a broader understanding and application of 3D-printed auxetic structures for improving mechanical properties of mortar specimens. NPR is a distinguishing characteristic of auxetic structures that can result in improved fracture toughness, indentation resistance, shear modulus, energy absorption and fatigue crack propagation [98–103]. The presence of auxetic structures effectively limit the transverse deformation of the infill material, thereby enhancing the composite's overall bearing capacity and energy absorption performance. Due to limited understanding about auxetic reinforced concrete composite, in this work, 3D printed polymeric auxetic lattice structures were used as reinforcement to develop cementitious composites with enhanced ductility. Compression performance of plain mortar along with reinforced specimens were experimentally investigated using four auxetic lattices with different Poisson's ratio. The performance analysis was conducted adopting experimental fracture images and the effect of auxetic Poisson's ratio on peak compressive strength and ductility properties were examined. Based on modified Hashin-Shtrikman model, Young's modulus of the LRCC specimens was estimated followed by the energy absorption capability discussion.

6.2 Auxetic lattice design

Here, the Type-A auxetic design is used from the previous work along with conventional RH as benchmark structure (Tessellated auxetic designs are not considered in this chapter). In order to investigate the effect of NPR, two other auxetic lattice structures from the literature [53, 104] are reffered. The four lattice designs having NPR ranging from -0.431 to 0.038 are used as mortar reinforcement. Based on Maxwell's stability factor (M), the bending-dominated deformation mode is confirmed for all the lattice designs. Table 6.1 shows a computer-aided design (CAD) model of four unit cells with the respective design variables and NPR, while Table 6.2 summarizes the numerical value of these design parameters. In this study, relative density ($\bar{\rho}$) of the lattice structures are kept constant (= 0.325).

Table 6.1 Different auxetic lattice designs

Lattice design	Unit cell	CAD model of 2D auxetic structures	NPR
Koch snowflake structure	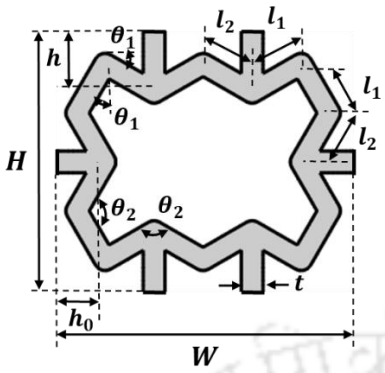	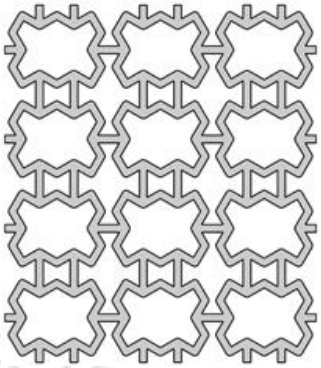	-0.038
Type-A Variant	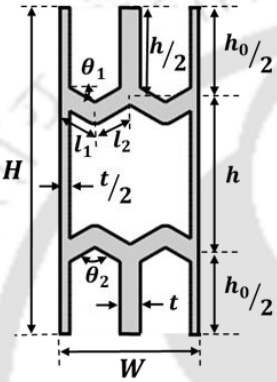	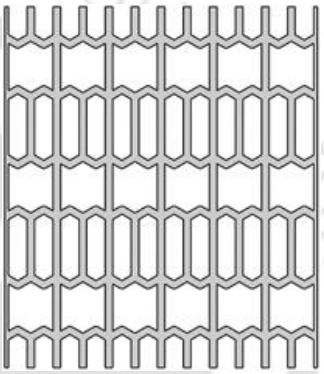	-0.095
Tubular structure	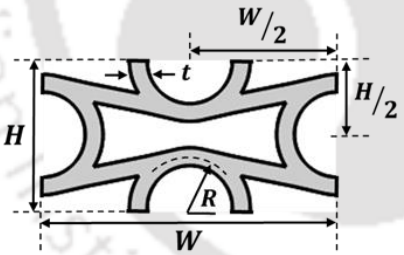	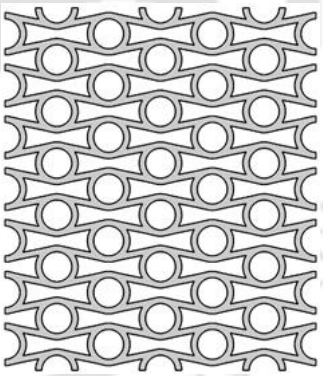	-0.189
RH structure	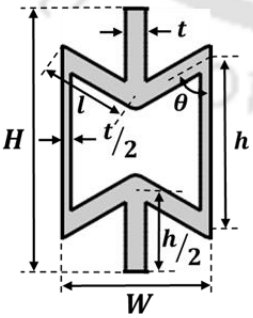	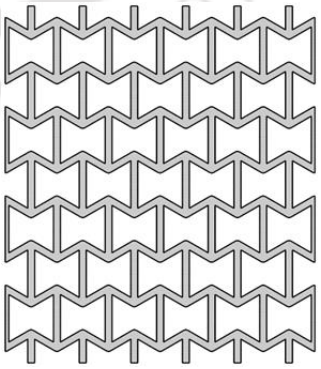	-0.431

Table 6.2 Design parameters of auxetic lattices

Lattice design	l	l_1	l_2	θ	θ_1	θ_2	h	h_0	t	R	H	W
Koch snowflake structure	-	4	4	-	30°	120°	4	3	1.54	-	18	20
Type-A Variant	-	3	3	-	30°	120°	12	12	1.5	-	24	10
Tubular structure	-	-	-	-	-	-	-	-	1.2	3.5	10.3	20
RH structure	6	-	-	60°	-	-	12		1.4	-	18	10

6.3 LRCC preparation- casting, curing and testing

Initially a homogeneous cementitious mortar was prepared as discussed in section 2.1.2. The mortar was poured in an acrylic mold containing 3D printed lattice structure. The mold was vibrated to ensure proper filling of mortar without any air bubbles. The steps involved in the fabrication of 3D printed lattice-reinforced concrete composites are summarized in Fig. 6.1.

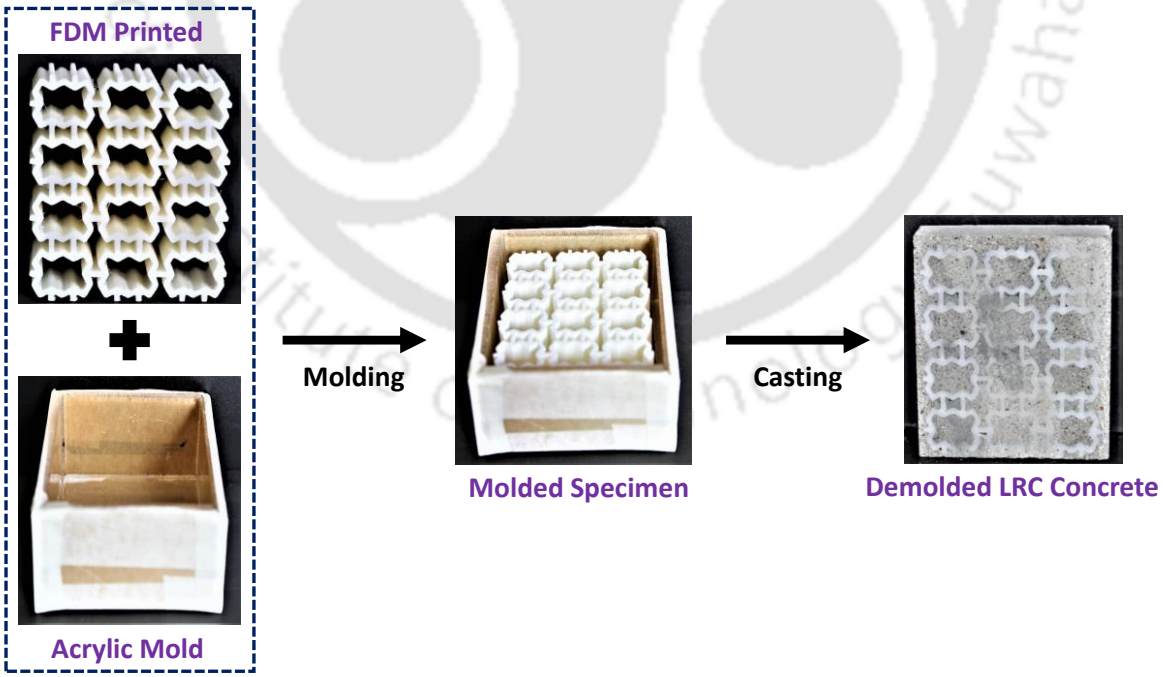

Fig. 6.1 Steps involved in the fabrication of 3D printed lattice-reinforced concrete composite

The LRCC composites were demolded after 2 days of casting and cured for 28 days in moist environment. The LRCC specimens containing Koch snowflake structure, Type-A Variant, Tubular structure and RH structure are named as LRCC1, LRCC2, LRCC3 and LRCC4 respectively.

6.4 Results and discussion

6.4.1 Crushing performance of lattice structure

6.4.1.1 Deformation sequences and mechanical response

Fig. 6.2 shows the stress-strain response and deformation sequences of all lattices during quasi-static compression. The elastic-plastic response of lattices has been studied in three stages. These three distinct stages have been identified and highlighted in Fig. 6.2 as the elastic regime, plateau regime and densification regime.

Elastic regime- it starts from the beginning of compression and ends when lattices start deforming plastically (yield point). It can be identified by a linear straight line in the stress-strain curves of the lattices at the early crushing. The inclined struts of the lattices are the critical member during the elastic phase, and the elastic performances of the lattices are highly influenced by them. These inclined struts generally experience all types of loading; axial loading, shear loading and bending, and fail when the stress inside the inclined strut reaches its critical stress. Near the end of the elastic regime, plastic hinges are formed at the joint and the cell of the lattices collapsed. The strength (yield stress), stiffness (Young's modulus) and stability (yield strain) of lattice structures are very important parameters that belong to the elastic performance of the lattice. Higher the strength, stiffness and stability properties of the lattice better the lattice design.

Out of the four lattice designs, Type-A Variant showed the highest stiffness (Young's modulus) 348.22MPa followed by RH structure, Koch snowflake structure and Tubular structure with stiffness of 85.26 MPa, 14.51 MPa and 13.95 MPa respectively. The variation in the stiffness for the lattices is in the range of 348.22-13.95 MPa where Type-A Variant has 2396.21% higher stiffness than Tubular structure. A similar pattern has been followed for the strength where again Type-A Variant has the highest yield stress (4.52 MPa). On the other hand, the yield strain follows the reverse pattern i.e. higher the stiffness lower will be the yield strain, and hence Tubular structure which showed the least stiffness has the highest yield strain (0.15). The variation in the yield strain for the lattices is in the range of 0.15-0.02 where Tubular

structure has a 650% higher yield strain than Type-A Variant. The elastic behavior of all lattice designs is presented in Table 6.3.

Table 6.3 Elastic behavior of lattice designs

Elastic properties	Koch snowflake structure	Type-A Variant	Tubular structure	RH structure
Young's modulus (MPa)	14.51	348.22	13.95	85.26
Yield stress (MPa)	1.05	4.52	1.53	2.50
Yield strain	0.09	0.02	0.15	0.04

Plateau regime- It is a long region in the stress-strain curves where lattices deform plastically. This region mainly contributed to the energy absorption by the lattices. The larger and more stable the plateau regime higher will be the energy absorption by the lattice. In this regime, during the crushing of the lattices, the deformation waves move from one cell or cells within a row to another cell or row; leaving a collapsed cell or row of cells behind them (a cell is collapsed either by the formation of a plastic hinge at the joint or by the buckling of the cell strut); forming a cell-collapsed pattern known as the deformation pattern of deforming lattices. These deformation pattern shown by deforming lattices is mainly responsible for the stress-strain relationship and formation of peaks and valleys within the plateau regime. When all cells within the lattices collapsed there is a sudden rise in the stress values due to the further compaction (densification) of collapsed cells; leading to the end of the plateau regime.

The deformation pattern shown by different lattices at different strains is presented in Fig. 6.2. It can be noted from Fig. 6.2(a) that the deformation pattern shown by the Koch snowflake structure is initially a "V" type deformation pattern due to shrinkage of the cell wall at a localized position and expansion at the boundaries. Further crushing leads to a change in the deformation pattern of Koch snowflake structure to the "Z" type deformation pattern. This type of deformation pattern makes the plateau region flat and stable with lower plateau stress by resisting the peaks and valleys formation.

While the deformation pattern of Type-A Variant depends (Fig. 6.2(b)) on its sub-cells. Initially, the lower relative density sub-cell deforms and collapsed due to its lower strength. Once all lower relative density sub-cell collapsed thereafter higher relative density sub-cell starts collapsing. Deformation moves from a more unstable region to a stable region. This type of deformation pattern forms peaks and valleys in the plateau region leading to an unstable plateau region.

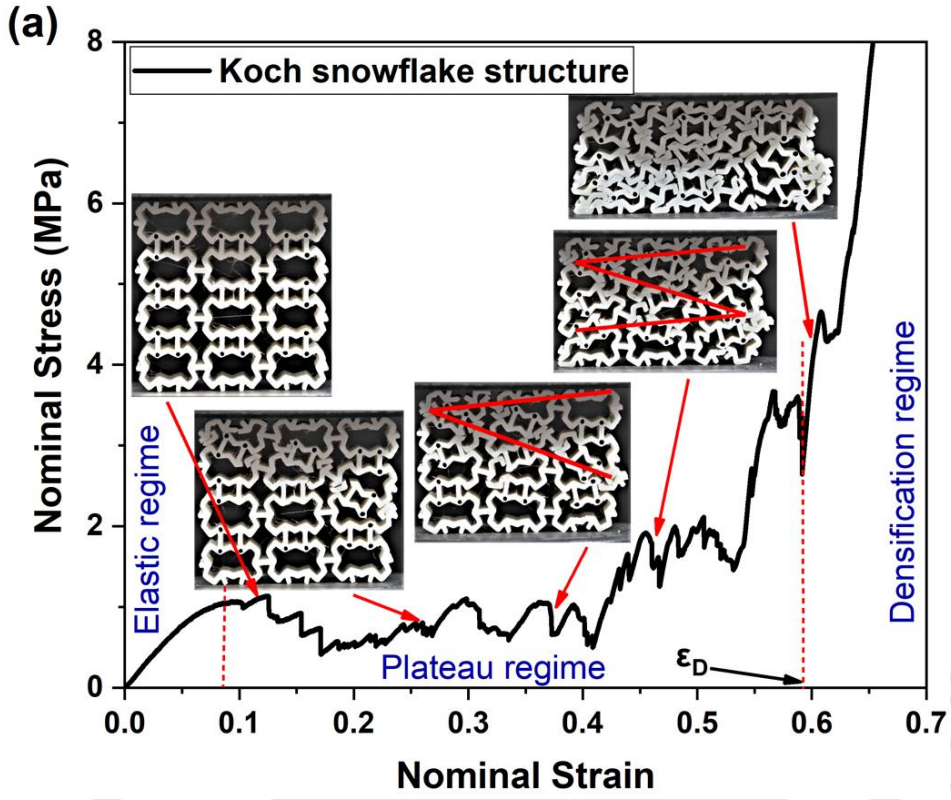

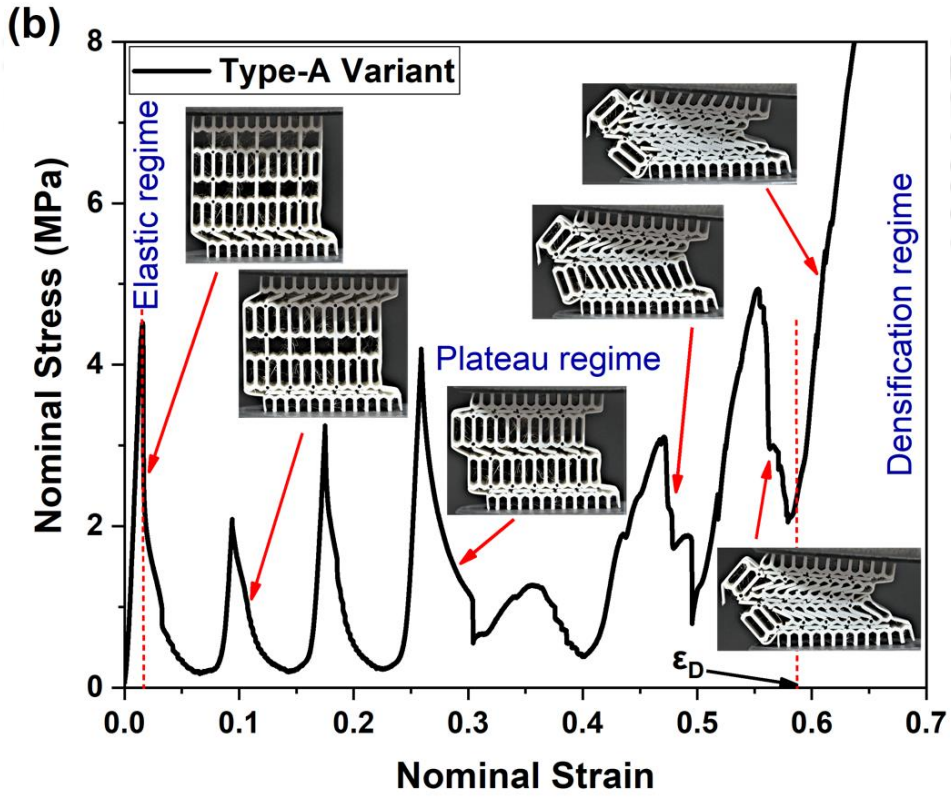

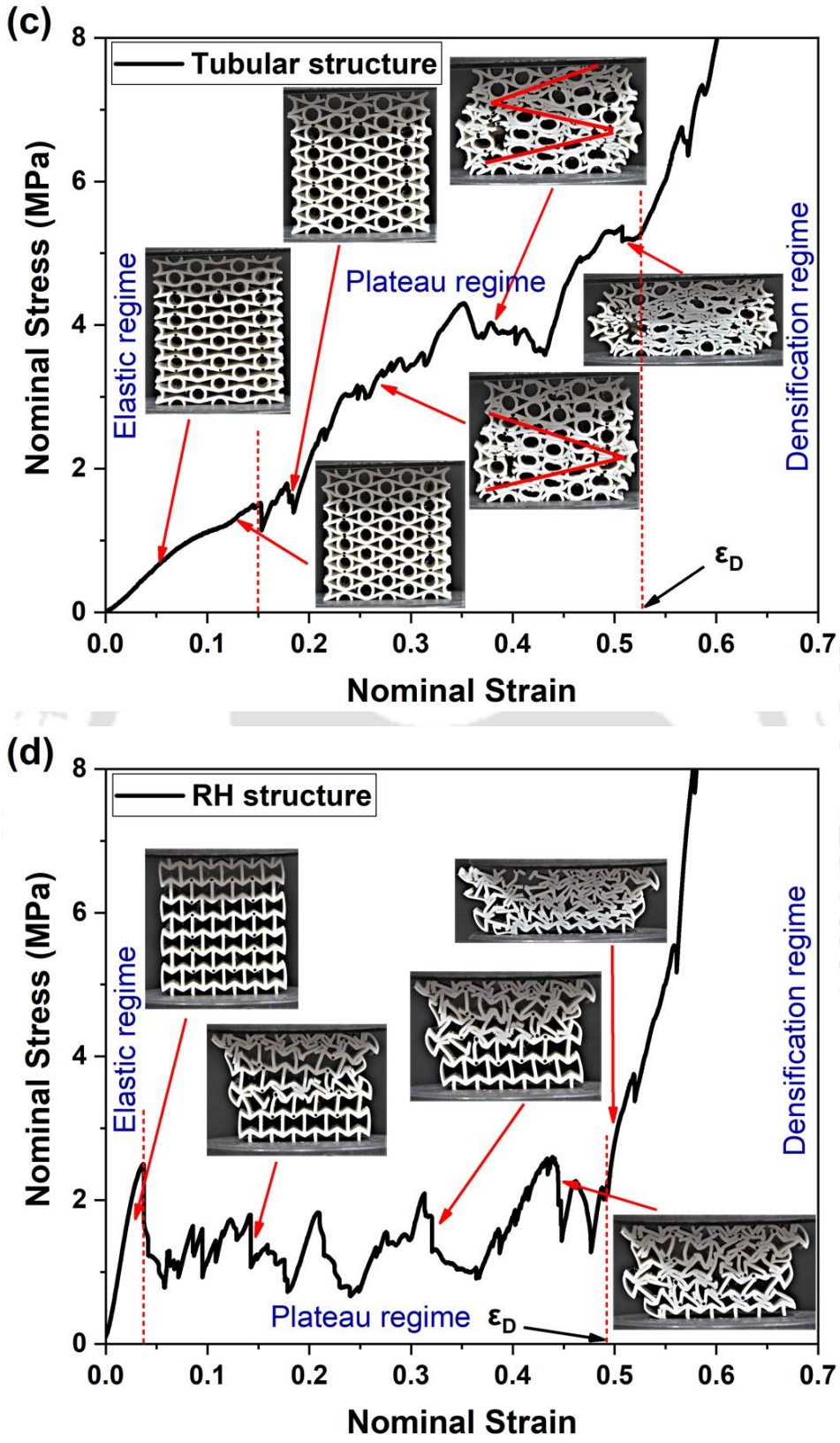

Fig. 6.2 Stress-strain response and deformation sequences of lattices during quasi-static compression; (a) Koch snowflake structure, (b) Type-A Variant, (c) Tubular structure and (d) RH structure

Fig. 6.2(c) shows the deformation pattern shown by Tubular structure during quasi-static compression. It can be noted that the deformation pattern shown by Tubular structure is initially a “V” type deformation pattern which further changed to the “Z” type deformation pattern which is similar to the Koch snowflake structure deformation pattern. But one should be noted that the deformation pattern which has already formed due to the collapse of cells was further continuously compacting during the continuous crushing, leading to an increase in the stress in the plateau region. Fig. 6.2(d) shows the deformation pattern of the RH structure where deformation moves from a more unstable region (at the center) to a stable region (at the ends) forming peaks and valleys in the plateau region.

Out of the four lattice designs, Tubular structure showed the highest energy absorption 1.47MJ/m^3 followed by Type-A Variant, Koch snowflake structure and RH structure with the energy absorption capacity of 0.86MJ/m^3, 0.68MJ/m^3 and 0.37MJ/m^3 respectively. The variation in the energy absorption capacity of the lattices is in the range of 1.47-0.68MJ/m^3 where Tubular structure has 297.29% higher energy absorption than RH structure.

Densification regime- densification regime is identified by a sharp increase in stress of the stress-strain curve. When all cells within the lattices collapsed there is a sudden rise in the stress values due to the further compaction (densification) of collapsed cells. In the compaction phase, the base material properties of the structure play an important role.

6.4.1.2 Poisson’s ratio

Fig. 6.3 shows Poisson’s ratio versus strain maps for all lattice designs. It can be noted that all lattices showed NPR for a wider strain range. For all the lattices, a similar trend has been observed for Poisson’s ratio variation with the deforming strain. Initially, up to 80% (approximately) of the maximum auxeticity, the auxeticity of the lattices increased linearly with a higher slope thereafter a fall in the slope of the auxeticity line was observed, and the rate of increasing the auxeticity slow down. Auxeticity became maximum at the yield point thereafter a sharp fall in auxeticity was observed till it reaches to 20% (approximately) of the maximum auxeticity. RH structure showed the highest auxeticity -0.431 followed by Tubular structure, Type-A Variant and Koch snowflake structure with the auxeticity of -0.189, -0.095 and -0.038 respectively. As RH structure showed the highest auxeticity than other lattices, and hence is more compressible compared to the other lattices. The variation in the auxeticity of the lattices is in the range of -0.189 to -0.038 where RH structure has 1034.21% higher

auxeticity than Koch snowflake structure. The variation in the auxeticity of the lattices is concerned with their geometry [78, 79].

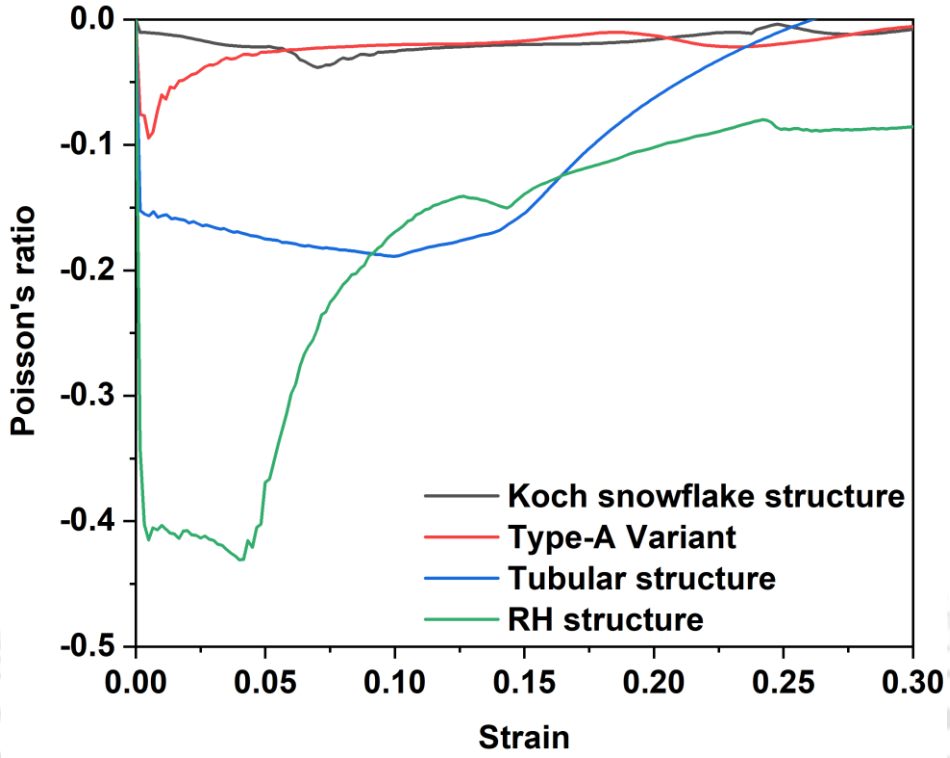

Fig. 6.3 Poisson's ratio versus strain maps for all lattice designs

6.4.2 Crushing performance of LRCC

Fig. 6.4(a) represents the nominal stress-strain response of the LRCC specimens during quasi-static compression. The overall response of LRCC composites was controlled by their constituent phases (reinforcement and matrix). As the volume fraction of matrix and reinforcement are 0.675 and 0.325 respectively, the crushing performance of LRCC specimens mainly governs by the matrix phase property. Despite this fact, reinforcement addition has highly affected the performance of LRCC composites. All LRCC specimens including concrete (without lattice reinforcement) shows five critical stresses which are marked in Fig. 6.4(b): (1)-Stress at the beginning of the crack, (2)-Stress at the yield point, (3)-Peak stress, (4)-Stress at the 15% drop of peak stress and (5)-Stress at the 50% drop of peak stress. In the initial compaction stage (i.e. till point (1)) the behavior of concrete and LRCC specimens were found to be similar. The stress increases slowly with the strain due to the formation of local indention at the top and bottom surfaces. However, in elastic deformation stage, the compressive capacity of concrete and LRCC specimens increases rapidly. The stress in this stage varies linearly with

strain. The Young's modulus of LRCC specimens was obtained from experimental testing and discussed in section 6.4.4 with the effect of auxetic lattice stiffness and Poisson's ratio.

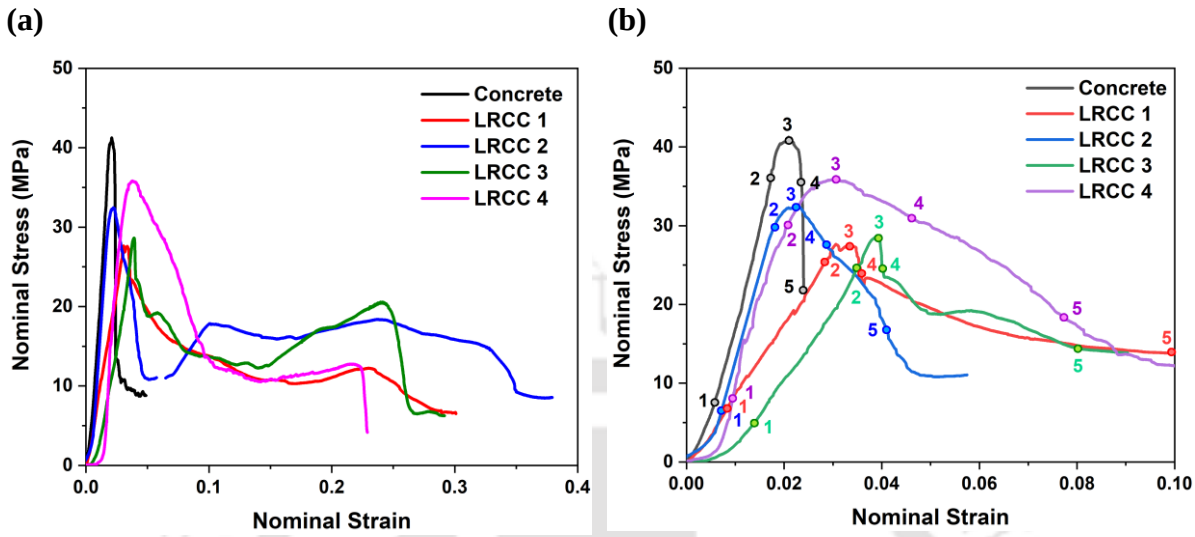

Fig. 6.4 (a) Nominal stress-strain response of the lattice-reinforced cementitious concrete (LRCC) specimens during quasi-static compression and (b) Nominal stress-strain response of LRCC and concrete specimens; numbering has been done to represent some of the critical stresses as (1)-Stress at the beginning of crack, (2)-Stress at the yield point, (3)-Peak stress, (4)-Stress at the 15% drop of peak stress and (5)-Stress at the 50% drop of peak stress

It can be noted from Fig. 6.5(a) that the LRCC 4 showed highest peak stress (35.82MPa) among the LRCC specimens followed by LRCC 2(32.38MPa), LRCC 3(28.64MPa) and LRCC 1(27.63MPa). All LRCC specimens exhibited lower peak stress but higher strain at peak than the concrete (Fig. 6.5(b)). These reinforced specimens have lower yield stress (compressive strength) and longer elastic deformation regions leading to higher yield strain. The auxetic lattices have lower stiffness and yield strength, hence they behave as soft inclusion in the concrete leading to higher strain at the peak stress. Except LRCC 2, all LRCC specimens have more than 50% improvement in the strain at peak stress. The highest improvement was seen in case of LRCC 3 specimen (85.71% more strain at peak stress than concrete) followed by LRCC 4, LRCC 1 and LRCC 2 with the improvement of 80.95%, 47.62% and 9.52% respectively.

The stress-strain response of LRCC specimens further deviated from concrete with progress in crushing; resulting in widespread of the curves due to the reinforced auxetic lattices. These lattices act as soft inclusion, contributing to larger elastic regions of LRCC specimens. One can assume that the LRCC specimens can be represented as a hard concrete phase surrounded by soft polymer lattice phase with connection at boundaries. Due to the larger elastic zone and NPR of lattices (refer section 6.4.1), the elastic zone of LRCC specimens

become higher than the concrete. The NPR of lattices inhibits shearing of concrete by preventing the formation and propagation of micro-cracks due to biaxial compression, while elastic property of the lattices increases elastic deformation of LRCC specimens.

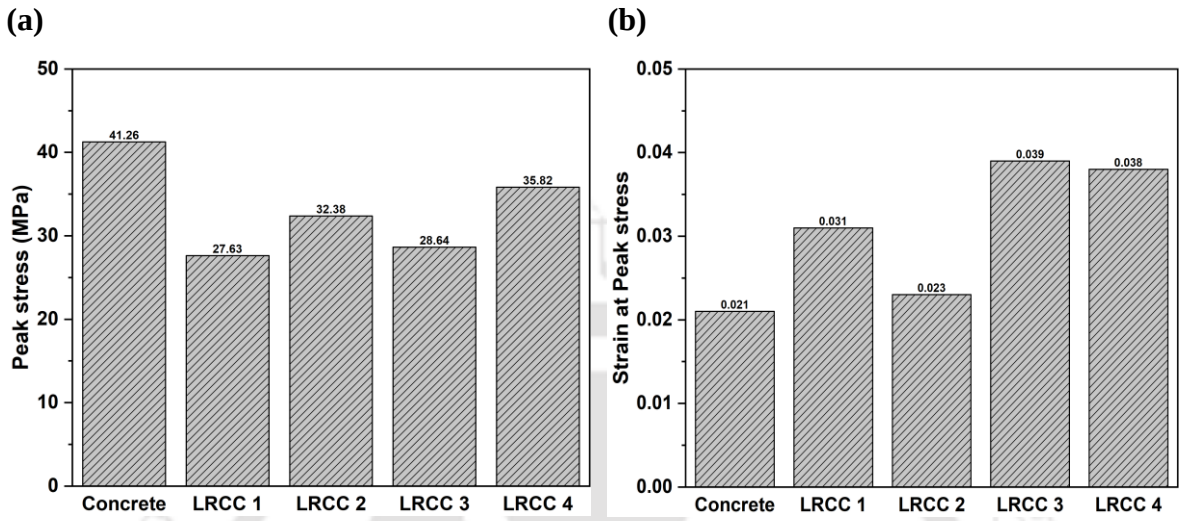

Fig. 6.5 (a) Peak stress and (b) strain at peak stress of concrete and LRCC specimens

A summary of stress values of different LRCC is given in Table 6.4. The load-bearing capacity of concrete and LRCC specimens decreases with progress in compression. The auxetic lattices have lower strength and stiffness than the concrete due to which they are unable to restrain the transverse expansion of concrete effectively. Shear bands formed from the free wall along the oblique direction and continuously penetrated inside the LRCC specimens as loading continued. The reinforced lattices restrict the shear band penetration and control failure patterns of LRCC specimens before showing "X" type brittle shear failure pattern [105]. It can be noted that auxetic lattices have completely damaged in the shear plane.

Table 6.4 Stress at different locations of LRCC specimens

Specimen type	(1)-Stress at the beginning of crack (MPa)	(2)-Stress at the yield point (MPa)	(3)-Peak stress (MPa)	(4)-Stress at the 15% drop of peak stress (MPa)	(5)-Stress at the 50% drop of peak stress (MPa)
Concrete	7.64	35.41	41.26	35.07	20.63
LRCC 1	6.98	26.01	27.63	23.49	13.82
LRCC 2	6.71	27.67	32.38	27.52	16.19
LRCC 3	6.82	24.85	28.64	24.34	14.32
LRCC 4	8.59	27.39	35.82	30.45	17.91

6.4.3 Failure behavior of LRCC

Fig. 6.6(a) shows the failure pattern and shear band formation of LRCC 1 specimen leading to "Z" type deformation pattern, which further converted to "X" type shear failure pattern. On the other hand, in LRCC 2 specimen, a shear band formed from the free wall along the oblique direction and continuously penetrated inside the LRCC specimens till they meet. After that another shear band formed perpendicular to the previous shear band, forming "Y" type deformation pattern, which further converted to "X" type shear failure pattern due to the formation of another shear band from the opposite direction. Fig. 6.6(b) shows the formation and movement of the shear band in LRCC 2 specimen. The deformation pattern shown by LRCC 3 is quite different from the other LRCC specimens (Fig. 6.6(c)). Here the specimen deforms gradually from bottom side till the formation of shear band, while in LRCC 4 specimen, a double "V" type of deformation pattern was observed (Fig. 6.6(d)).

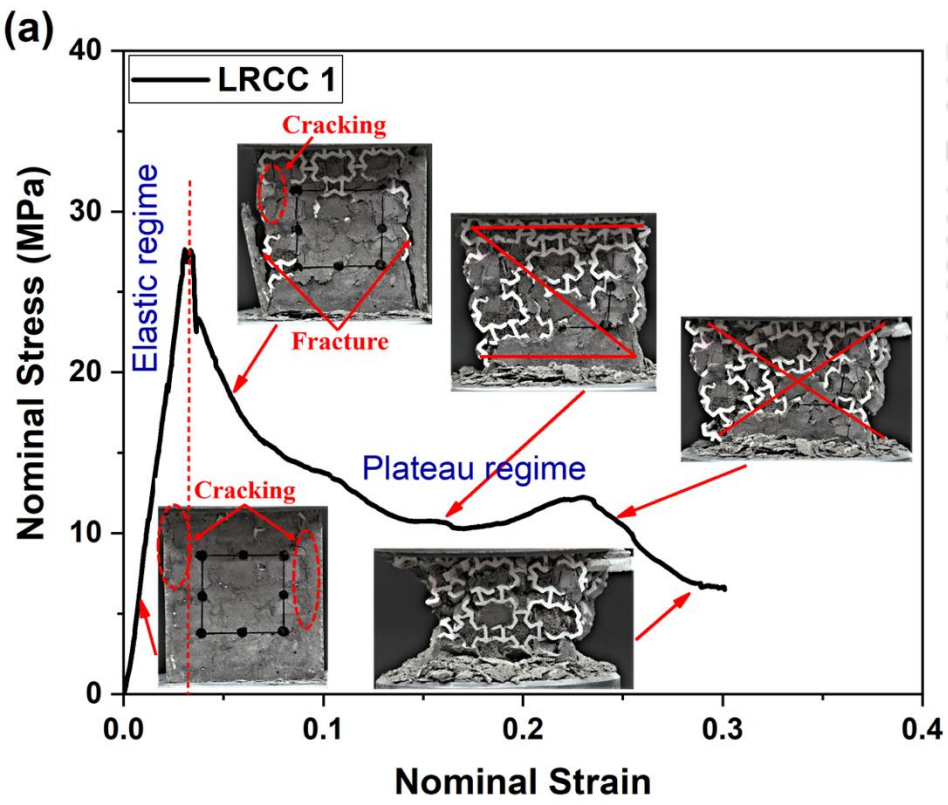

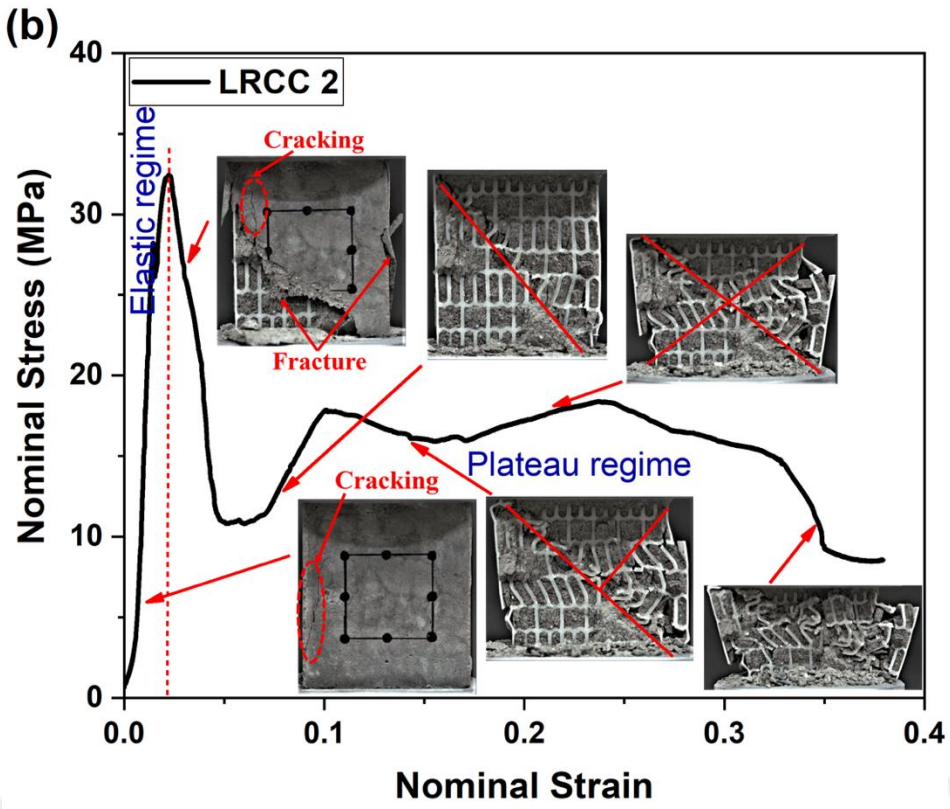

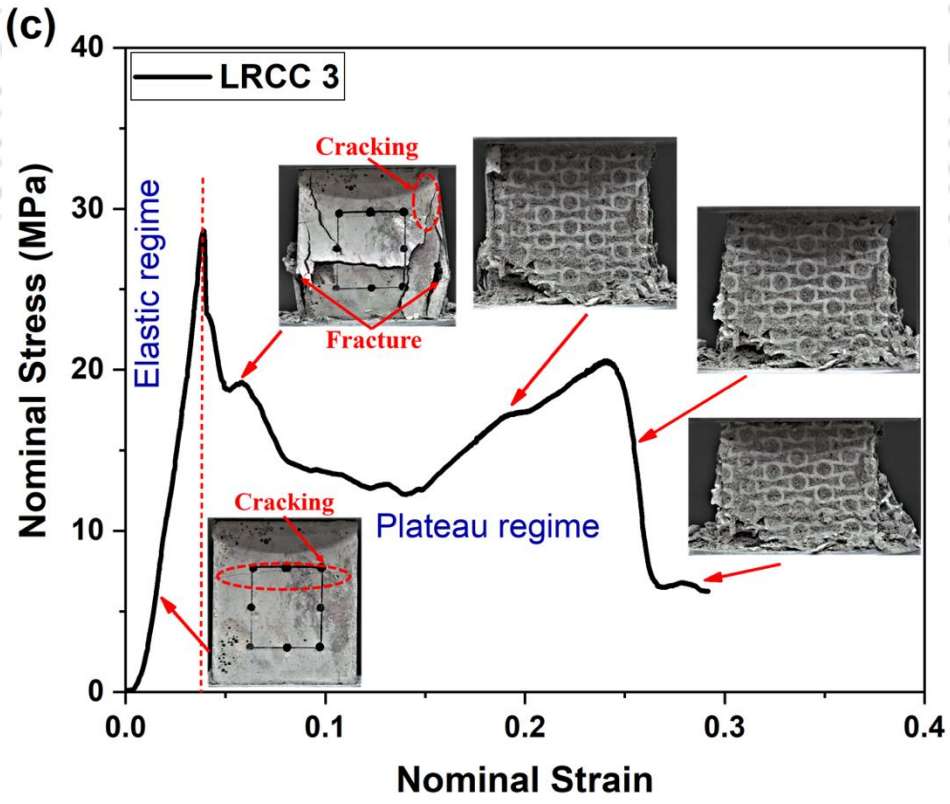

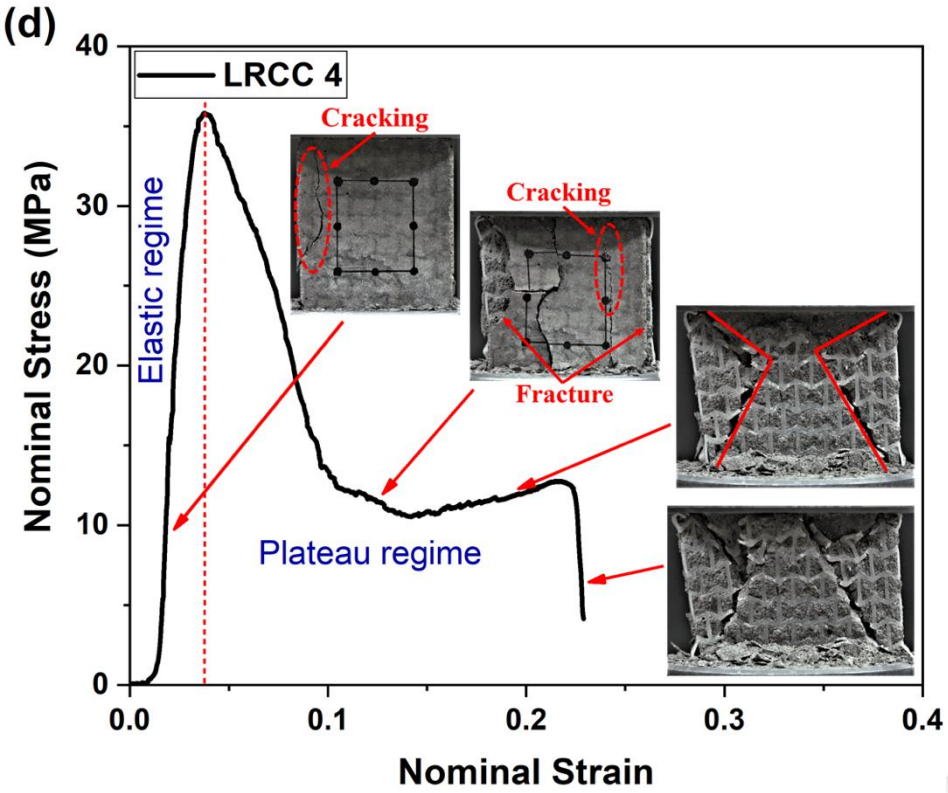

Fig. 6.6 Stress-strain response and deformation sequences of (a) LRCC 1, (b) LRCC 2, (c) LRCC 3 and (d) LRCC 4 specimens

6.4.4 Elastic modulus of LRCC

Fig. 6.7 shows Young's modulus of the LRCC specimens. It can be noted that all LRCC specimens exhibit lower (35.64% - 64.16%) Young's modulus than the concrete and LRCC 2 showed the highest Young's modulus. Young's modulus of the LRCC specimens is influenced by their constituent phases i.e. lattice and concrete properties . Young's modulus of lattices contributes in providing stiffness of LRCC against the applied load, while the NPR of lattices inhibits shearing of concrete by preventing the formation and propagation of micro-cracks due to biaxial compression. It is observed that due to higher Young's modulus of Type-A variant, the LRCC 2 specimen possess higher Young's modulus. A similar effect on Young's modulus of the LRCC specimen has been observed with NPR, i.e. Young's modulus of the LRCC specimen increases with increase in NPR of LD, as they tend to restrict the deformation, resulting in higher Young's modulus [106].

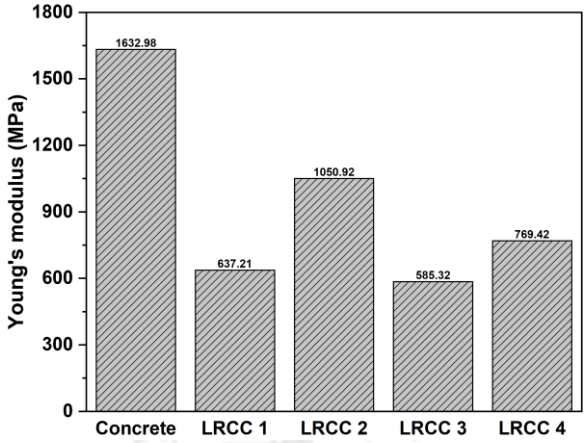

Fig. 6.7 Young's modulus of LRCC specimens

6.4.5 Ductility of LRCC

The structural behavior of LRCC specimens is investigated through ductility. Fig. 6.8(a) represents different types of loads and its corresponding axial deformation used for the calculation of ductility. The Ductility (μ) is calculated using equation 6.9.

$$\mu = \frac{\delta_u}{\delta_y} \tag{6.9}$$

Where δ_u and δ_y are axial deformations at ultimate load and yield load respectively.

In this section, the ductility of LRCC specimens in axial compression is calculated at two points similar to [107][108]. The first point refers to 15% drop in peak load and second point is considered at 50% drop in peak load. The corresponding axial deformations are considered as axial deformations at ultimate load. The axial deformations of LRCC specimens at different loads are given in Fig. 6.8(b). In Fig. 6.8(b) δ_y, δ_0, $\delta_{15\%}$ and $\delta_{50\%}$ represents axial deformation at yield load, peak load, 15% drop in peak load and 50% drop in peak load respectively. Ductility calculated at 1st and 2nd points is represented as μ_1 and $\mu_2$respectively. The ductility of all LRCC specimens is given in Fig. 6.8(c).

It can be noted from Fig. 6.8(c) that LRCC 4 showed the highest ductility among all LRCC specimens. The ductility of LRCC 4 specimen is 102.87% higher than concrete. Similarly, LRCC 2 specimen has 53.03% higher ductility than concrete. However, LRCC 1 and LRCC 3 specimens possess 7.8% and 10.8% lower ductility than concrete.

It has been observed that the axial deformation of LRCC specimens at yield load is highly controlled by the yield strain of auxetic lattices rather than their auxeticity: higher the yield strain of lattices, more will be the axial deformation of LRCC specimens at yield load (Fig. 6.8(d)). There is a linear fit between the axial deformation of LRCC specimens at yield load and yield strain of lattices, which suggests that with increase in yield strain of lattices, the axial

deformation of LRCC specimens at yield load increases linearly with a slop of 11.88±1.01. But as it reaches to peak load the influence of auxeticity dominates since it tends to restrict the movement of micro-cracks due to the by-axial compression. The maximum auxeticity of lattices was shown near the yield strain of the lattice and thereafter there was a fall in the auxetic behavior of lattices. Further, as compression continued after the peak load, the concrete was unable to hold the load and there was a sudden drop in the load. On the other hand, due to auxeticity of reinforced lattices, the LRCC specimens were still able to hold the load for a longer axial deformation after the peak load. The more the auxeticity of lattices, more will be the axial deformation of LRCC specimens after the peak load.

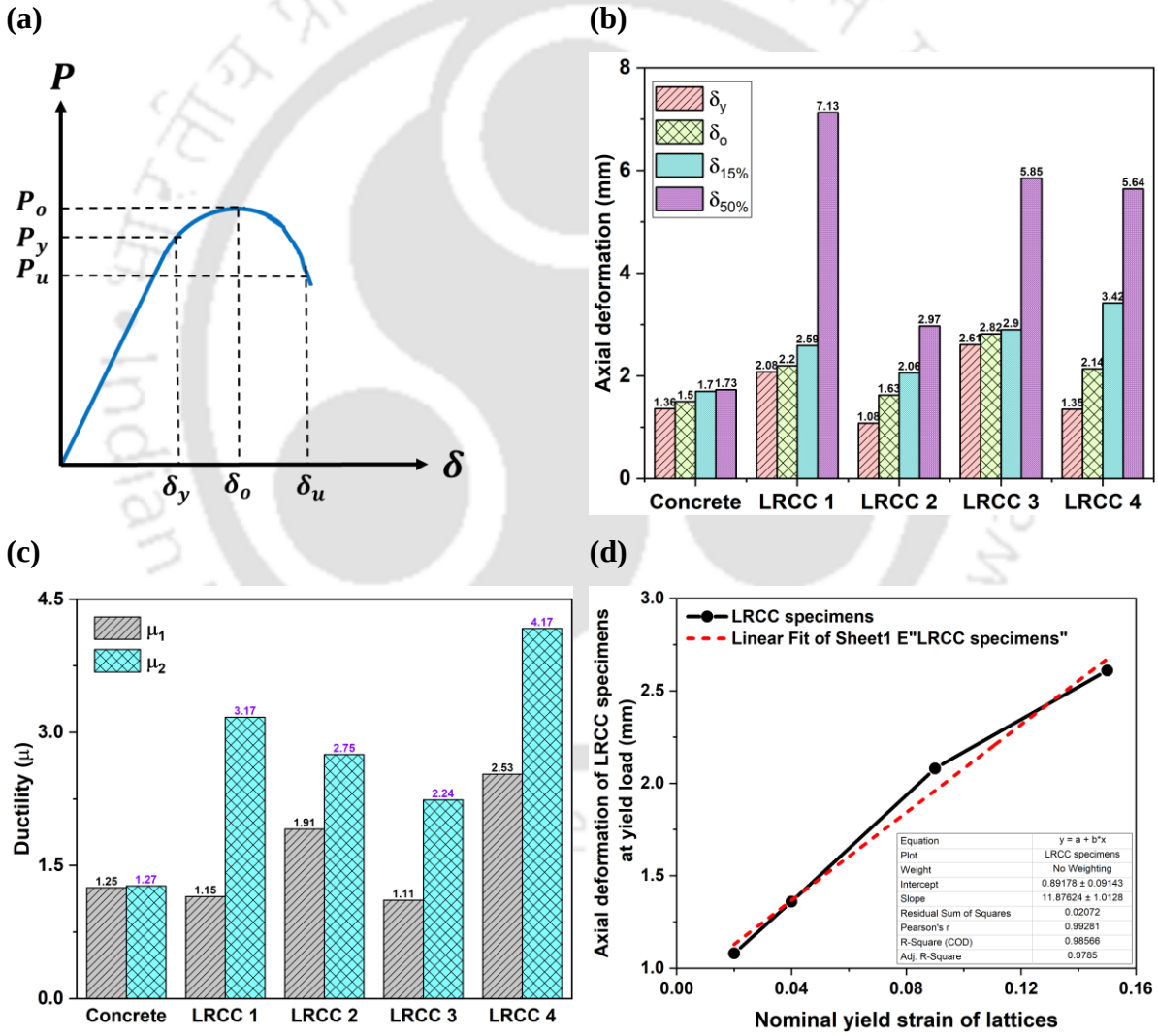

Fig. 6.8 (a). Types of loads and its corresponding axial deformation used for the calculation of ductility, (b) axial deformations of LRCC specimens at different loads; $\boldsymbol{\delta_y}$, $\boldsymbol{\delta_0}$, $\boldsymbol{\delta_{15\%}}$ and $\boldsymbol{\delta_{50\%}}$ represents axial deformation at yield load, peak load, 15% drop in peak load and

50% drop in peak load respectively, (c) ductility of LRCC specimens and (d) plot between axial deformation of LRCC specimens at yield load and yield strain of lattices

As per the above discussion, it can be concluded that the axial deformation of LRCC specimens at yield load is highly influenced by the yield strain of lattices, while auxeticity has a high influence after the yielding of LRCC specimens. As ductility (μ) is the ratio of axial deformation at ultimate load to that of axial deformation at yield load, hence it can be increased either by reducing the axial deformation at yield load or increasing the axial deformation at ultimate load. In this regard, to increase the ductility of LRCC specimens, lattices having lower yield strain and higher auxeticity are highly recommended. Here, the RH structure has the highest auxeticity with low yield strain and hence LRCC 4 specimen exhibited the highest ductility.

The LRCC 4 specimen also exhibited highest ductility at second point. The ductility shown by LRCC 4 specimen is 229.08% higher than concrete. The other LRCC specimens also have higher ductility, for example the ductility of LRCC 1, LRCC 2 and LRCC 3, calculated at second point, was found to be approximately 150%, 117% and 76% higher than concrete respectively.

6.4.6 Energy absorption of LRCC

Here three points were identified at which energy absorbed by concrete and LRCC specimens were calculated, these points are 15% drop in peak load, 50% drop in peak load and complete failure [107]. As majority of the energy absorption by the specimen belongs to the plateau area; more the plateau area higher will be the energy absorption capacity (MJ/m^3) of the specimen. The plateau area is a region between the yield point and the failure point of the LRCC specimens [109].

Fig. 6.9(a) represents the energy absorption capacity versus nominal strain maps of concrete and LRCC specimens. This plot helps in analyzing the energy absorption performance of concrete and LRCC specimens under quasi-static compression. The slope of the energy absorption capacity versus the nominal strain curve indicates the rate of energy absorption by the LRCC specimen.

For a given strain, if the slope of energy absorption capacity versus nominal strain curve is higher it indicates higher load-bearing capacity of the LRCC specimen. The energy absorption within the elastic region is very small compared to the total energy absorption by

the LRCC specimens, but it is significant for the concrete as more than half of the energy is absorbed by the concrete within the elastic region.

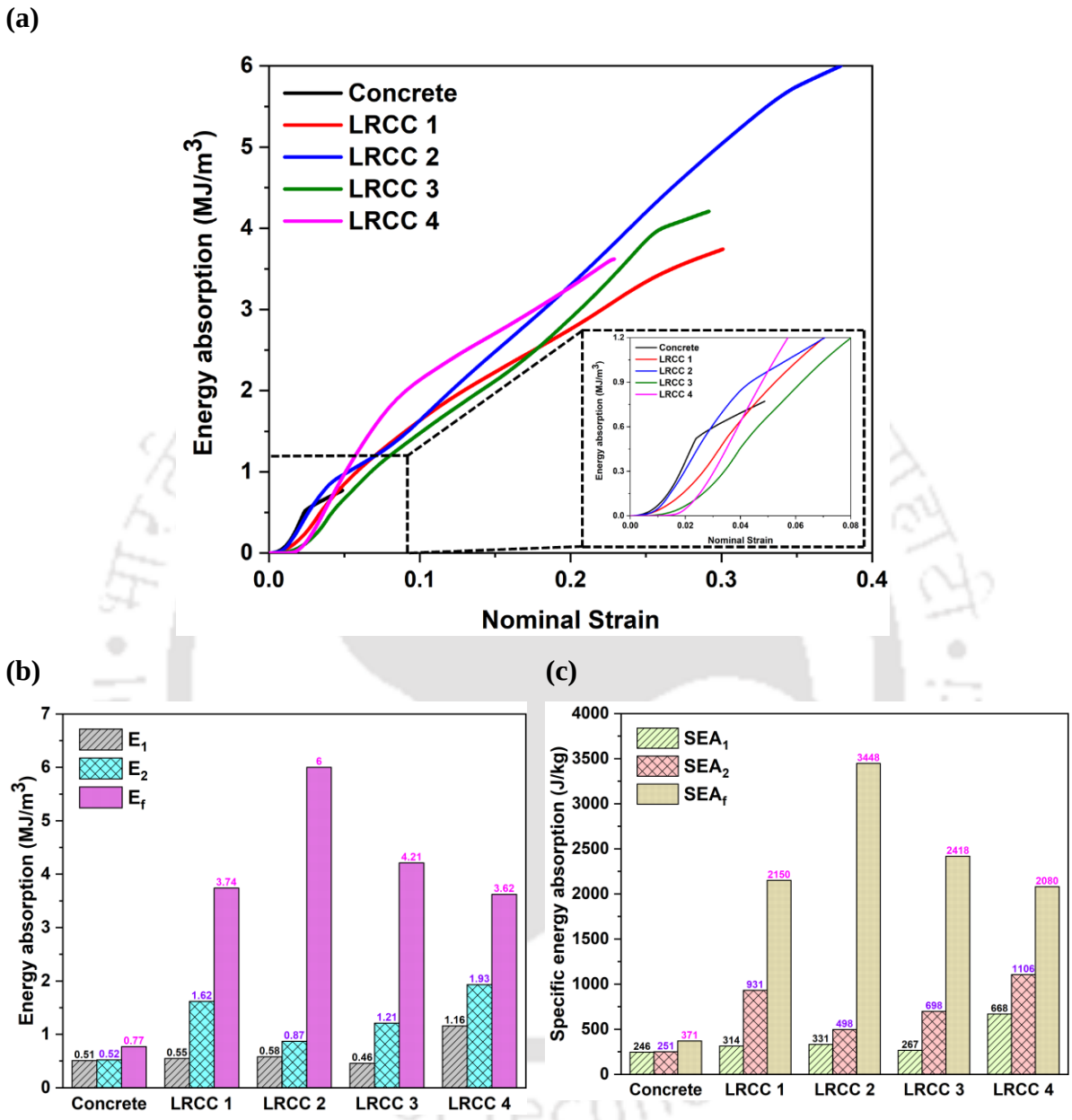

Fig. 6.9 (a). Energy absorption versus nominal strain plot, (b). energy absorption capacity (MJ/m^3) of the concrete and the LRCC specimens; E_1- energy absorption at 15% drop in peak load, E_2- energy absorption at 50% drop in peak load and E_f- energy absorption at failure and (c). specific energy absorption capacity (J/kg) of the concrete and the LRCC specimens; SEA_1- specific energy absorption at 15% drop in peak load, SEA_2- specific energy absorption at 50% drop in peak load and SEA_f- specific energy absorption at failure

It can be observed from Fig. 6.9(a) that within the elastic region, concrete has the highest rate of energy absorption, followed by LRCC 2, LRCC 4, LRCC 1 and LRCC 3 which suggests

that concrete has higher load-carrying capacity within the elastic region due to its stiffness (stiffness of concrete is highest than the LRCC specimens). Within the elastic region, there is a linear relation between the stress and strain, and for a given strain, stress is higher if stiffness is higher and hence load-bearing capacity.

But when the compressive strain becomes higher than the yield strain auxeticity plays an important role (near the peak load), as they tend to restrict the movement of micro-cracks due to by-axial compression and control the load-bearing capacity of the LRCC specimens. The LRCC 4 has highest slope of 'energy absorption capacity versus nominal strain' curve after the yield region due to the presence of lattice design with highest auxeticity within it, and it's slope gradually reduced due to reduction in auxeticity with strain. Thereafter, the energy absorption capacity of LRCC specimens is controlled by the deformation patterns. Similar behavior has been observed for other LRCC specimens.

Fig. 6.9(b) represents the energy absorption capacity (MJ/m^3) of the concrete and LRCC specimens at three points; E_1- energy absorption at 15% drop in peak load, E_2- energy absorption at 50% drop in peak load and E_f- energy absorption at failure. In general, all LRCC specimens and concrete have absorbed nearly equal energy at 15% drop in peak load except the LRCC 4. The energy absorbed by LRCC 4 at 15% drop in peak load was 1.16 MJ/m^3 which was more than twice the value of concrete. On the other hand, for the 2^{nd} and 3^{rd} points i.e. E_2- energy absorption at 50% drop in peak load and E_f- energy absorption at failure respectively, there was a significant improvement in the energy absorption by the LRCC specimens than concrete. The energy absorbed by LRCC 4, LRCC 1, LRCC 3 and LRCC2 at 50% drop in peak load were 268.56%, 210.00%, 132.45% and 65.74% higher than concrete respectively. Similar performance has been observed for the 3^{rd} point i.e for the E_f- energy absorption at failure. Here the energy absorbed by LRCC specimens was many folds higher than concrete. Among all, the LRCC 2 showed highest energy absorption at failure which is nearly eight times higher than concrete, as LRCC 2 showed higher failure strain which leads to a larger plateau region and hence higher energy absorption capacity. Similarly, LRCC 3, LRCC 1 and LRCC 4 specimens have nearly 5.5, 4.8 and 4.7 times higher energy absorption than concrete at failure, respectively.

The specific energy absorption (SEA) is used to correlate the concrete and LRCC specimen performance having density equals to 2080 kg/m^3 and 1740 kg/m^3 (same for all LRCC specimens) respectively. Fig. 6.9(c) represents specific energy absorption capacity (J/kg) of the concrete and LRCC specimens at different points. All LRCC specimens and concrete have nearly equal SEA at 15% drop in peak with an exception of LRCC 4. The SEA_1

of LRCC 4 was found to be highest among all with an improvement of 171.61% than concrete. Similarly, the LRCC 4 and LRCC 2 have highest specific energy absorption of 1106J/kg and 3448J/kg (with an improvement of 340.58% and 830.25%) with respect to concrete in SEA_2- specific energy absorption at 50% drop in peak load and SEA_f- specific energy absorption at failure, respectively.

6.5 Summary

In this study, 3D printed polymeric auxetic lattice structures were used as reinforcement to develop cementitious composites with enhanced ductility. The compression performance of plain mortar along with reinforced specimens was experimentally investigated using four auxetic lattices with different Poisson's ratio. Results indicate that auxetic structures have low stiffness and yield strength and hence they behave as soft inclusion in the concrete leading to higher strain at the peak stress, despite resulting low peak stress concrete composites. Due to the larger elastic zone and NPR of lattices, the elastic zone of LRCC becomes higher than the plain concrete. Based on the investigation, it was found that Young's modulus of LRCC increases with an increase in NPR and Young's modulus of auxetic lattice and it can be accurately estimated using a modified Hashin-Shtrikman model. The maximum ductility improvement was found to be around 100% and 200% at 15% and 50% drop in peak load respectively for the LRCC 4 due to lower yield strain and higher auxeticity of the lattice. Out of all, the LRCC 2 showed highest energy absorption at failure which is nearly eight times higher than concrete followed by LRCC 3, LRCC 1 and LRCC 4 specimens. The findings of the study suggest that the peak stress, ductility, Young's modulus and energy absorption capacity of LRCC can be tailored by tuning auxetic lattice properties.

Chapter 7 Conclusions and scope for future work

This chapter presents the conclusions and critical findings of the study, and it also provides scope for future work.

7.1 Conclusions

Auxetic lattices have attracted increasing attention due to their unusual mechanical behavior and potential for an array of applications. However, a narrow window of stiffness realizable for a given cell topology limits their applications. In the present work, auxetic lattice structures have been designed to improve their mechanical performance specifically Young's modulus and the energy absorption capacity. Novel 2D re-entrant auxetic lattices capable of exhibiting enhanced stiffness and energy absorption are proposed based on the geometric tailoring method. These modified re-entrant auxetic lattices were realized via fused deposition additive manufacturing. The deformation patterns and the energy absorption characteristics of 3D printed auxetic lattices under quasi-static compression were investigated via both Finite Element (FE) simulations and experiments. The effective elastic stiffness of the proposed lattices was theoretically estimated. Thereafter the best-proposed auxetic lattice structure has been used to study the effect of tessellation on the mechanical performance of the lattice. For this purpose, various tessellation strategies according to the periodic tessellation based on connectivity were designed.

Further, the best-proposed auxetic lattice structure has been used as reinforcement to develop cementitious composites with enhanced ductility. The compression performance of plain mortar along with reinforced specimens was experimentally investigated using four auxetic lattices with different Poisson's ratios. The following conclusions are drawn from the work reported in the thesis.

7.1.1 In-plane energy absorption of modified re-entrant auxetic structure

Eenergy absorption characteristics of a modified re-entrant auxetic structure processed via fused filament fabrication technique were evaluated both experimentally and numerically and its performance was compared with a conventional re-entrant auxetic structure of the same mass. Many topology-tailored designs were investigated using the Design of Experiment (DOE). The statistical models (derived by response surface methodology) were used to estimate their mechanical properties. It is clear from the results of the parametric study that the performance of the proposed auxetic structure is dependent on the strut-length ratio and joint angles. Having captured these relationships, optimization of geometrical parameters for the highest energy absorption was carried out for the proposed auxetic structure. The following conclusions can be drawn from this study:

- The compression response of auxetic structure predicted using the finite element method shows that the link length ratio has the highest influence on the energy absorption properties followed by joint angle interaction effects.
- The analysis shows that for the highest joint angles, the proposed structure evinces the lowest energy absorption capacity. However, it is interesting to note that the joint angles significantly affect the compressive strength but the strength is least affected by the link length ratio.
- It is also clear from the parametric analysis that the structure exhibits the highest Young's modulus at higher values of θ_1 with the highest value of θ_2 (i.e. 180^0), as at the highest value of θ_2 (i.e. 180^0) the structure response is analogous to that of the traditional regular re-entrant model and hence it is no more affected by the l_1: l_2 ratio.
- The most desirable solution with the highest energy absorption was found to be at l_1:l_2 ratio, θ_1 and θ_2 of 1, 40°, and 120° respectively. The crushing analysis indicates that the optimized structure outperforms (+36%) regular re-entrant honeycomb and the improvement can be attributed to the introduction of more nodes with lower node connecting joints. This results in increased compliance of structure and thus the energy absorption capacity.

7.1.2 Novel auxetic re-entrant structure exhibiting enhanced stiffness and energy absorption

Two novel re-entrant auxetic lattices namely, Type A and Type B variants were proposed by introducing vertical ligaments into the re-entrant lattice structure (previous work). The addition of ligament converts the unit cell into binary sub-cells and the resulting sub-cell properties were found to significantly affect the mechanical properties. The theoretical formulae for computing the effective Young's modulus of the proposed structures were developed using an energy-based approach and validated by the FE results. The FE model was able to reasonably accurately predict the deformation patterns and the failure observed in the experiments. The following conclusions can be drawn from this study:

- Type A and Type B variants exhibit about 165% and 147% higher specific energy absorption than conventional re-entrant structure respectively, due to their effective composite architecture.

- Similarly, an improvement of about 355% and 198% in Young's modulus was observed for Type A and B auxetics respectively.
- RH structure is more auxetic than Type-A and Type-B variants with a Poisson's ratio of -1.324, -0.121 and -0.057 respectively. The presence of vertical ligament in Type A and B structures restricted the inward movement of inclined walls lowering the transverse strain and hence their Poisson's ratio.
- Architectural tailoring of auxetic structures opens the possibility of simultaneously enhancing stiffness, strength, and energy absorption.
- The enhanced stiffness and energy absorption capability make the proposed novel structures as potential candidates for protective devices.

7.1.3 Tessellation controlled mechanical properties of 3D printed auxetic structures

In this study, the unit cell from our previous work (Type-A variant) is considered the base unit cell, and different tessellation strategies such as 'edge-to-edge' 'non-edge-to-edge' and 'overlapping' tessellation are applied. The effect of tessellation on the mechanical properties of cellular structures is studied. Various tessellation strategies were designed in Solid Works by importing the unit cell and investigated through Finite Element (FE) simulations. One tessellated structure from each group is 3D printed and experimentally tested. Numerical results are validated by comparing them with the experimental results. The FE results corroborated by experiments, elucidate the role of tessellation on the effective mechanical properties of the tessellated lattices. The following conclusions can be drawn from this study:

- Different tessellation strategies lead to different crushing responses of lattices during quasi-static compression.
- Tessellation causes variable thickness of the ligaments of the cells; some portions of the ligaments have low thickness which limits the elastic performance of the tessellated lattice structure.
- Young's modulus of Overlapping tessellation of Case-1 structure (450.43 MPa) is the highest among all the tessellated structures which indicates that it possesses strong support ability during small deformation, while Case-3 of non-edge-to-edge tessellation structure (157.93 MPa) has lowest Young's modulus.

- The yield strength of the Overlapping tessellation of Case-1 structure (6.52 MPa) is superior to other Tessellated structures, and therefore, it has very good resistance to an external force.
- The least yield strength is 2.04 MPa which is shown by Case-3 of non-edge-to-edge tessellated structure due to its variable wall thickness where the least wall thickness is 1mm which is at least half than that of other tessellated lattice structures.
- Out of all tessellated lattice structures, three structures exhibited auxetic behavior while four structures exhibited non-auxetic behavior. 'Non edge-to-edge tessellation Case-3' lattice structure showed the highest auxeticity than that of the 'edge-to-edge tessellation' and 'Non edge-to-edge tessellation Case-1' lattice structure with a Poisson's ratio of -1.022, -0.121 and -0.116 respectively. While 'Overlapping tessellation Case-2' lattice structure showed the highest positive Poisson's ratio than that of the 'Overlapping tessellation Case-1', 'Overlapping tessellation Case-3' and 'Non edge-to-edge tessellation Case-2' lattice structures with a Poisson's ratio of 0.538, 0.425, 0.172 and 0.141 respectively.
- The specific energy absorption (SEA) of all the cases of 'Non edge-to-edge tessellation' and 'overlapping tessellation' is higher than that of the 'edge-to-edge tessellation'. The SEA of 'Overlapping tessellation Case-2' structure is the highest (~ 10495.35 J/kg) amongst all the tessellated lattice structures and is ~90.81 % more than 'Edge-to-edge tessellation' (~5500.36 J/kg).
- The findings of the study suggest that the strength, stiffness, energy absorption capacity and Poisson's ratio of 2D auxetic lattices can be tailored by applying different tessellation strategies.

7.1.4 Crushing behavior of cementitious composites reinforced with auxetic lattice structures

This work investigates the crushing behavior of cementitious composites reinforced by 3D printed auxetic structures. Four auxetic lattice structures are 3D printed using polymeric material ABS and used as reinforcement for cementitious mortar. The compressive properties, ductility, energy absorption and failure behavior of the lattice reinforced cementitious composite (LRCC) are investigated. Based on the obtained results, following conclusions are drawn.

- The experimental results indicate that the failure behavior of plain concrete altered from brittle cracking to ductile failure after incorporation of the auxetic lattice. The ductility of LRCC 4 was significantly increased (max. value > 200%) due to the presence of auxetic lattices having lower yield strain and high auxeticity.
- Both experimental and numerical results reported that despite lower peak stress, the LRCC specimens have higher yield strain than plain concrete. The negative Poisson's ratio of lattices inhibits shearing of concrete by preventing the formation and propagation of micro-cracks due to by-axial compression, while elastic property the lattices increases elastic deformation of LRCC.
- According to the modified Hashin-Shtrikman model, higher Young's modulus and negative Poisson's ratio of RH structure resulted in the highest Young's modulus of the LRCC 4 among all LRCC specimens.
- The presence of auxetic lattices influences the failure strain and energy absorption capability of LRCC. The LRCC 2 specimens showed the highest (+800%) energy absorption compared to plain concrete due to higher failure strain which leads to a larger plateau region and hence higher energy absorption capacity.

7.2 Scope for future work

Although some authors have proposed new re-entrant designs, there are still a number of challenges that need to be overcome for the final utilization of 3D printed lattice structures.

- The surface roughness characteristics of FDM 3D printed are not acceptable in many applications and thus, it requires improvement.
- Anisotropic structure–property relationship is also non-negligible in FDM printing, which is caused due to layer-wise manufacturing and interfacial issues.
- Optimization of the process parameters and part post-processing can highly improve the mechanical performances.
- In most of the studies, the design concepts were guided by human intuition and demands for new approaches to further optimize existing lattice unit cells and propose unique structures. Integrating the finite element method with machine learning is an important future research direction. Data driven techniques such as AI and ML have the capability to capture the stochastic nature of the 3D printing process, which is highly important for producing robust and repeatable part properties.

- Ultimately, the widespread applications of 3D and 4D printed auxetic re-entrant structures will provide substantial motivation for developing new models and multi-functional structures.

References

1. Del Vescovo D, Giorgio I (2014) Dynamic problems for metamaterials: review of existing models and ideas for further research. Int J Eng Sci 80:153–172
2. Carneiro V, Meireles J, Puga H (2013) Auxetic materials—A review. Mater Sci 31:561–571
3. Yu X, Zhou J, Liang H, et al (2018) Mechanical metamaterials associated with stiffness, rigidity and compressibility: A brief review. Prog Mater Sci 94:114–173
4. Wegener M (2013) Metamaterials beyond optics. Science (80-) 342:939–940
5. Gibson LJ, F.Ashby M (1997) [Lorna_J._Gibson,_Michael_F._Ashby]_Cellular_Solid(z-lib.org).pdf. Cambridge Solid State Sci. Ser.
6. Surjadi JU, Gao L, Du H, et al (2019) Mechanical metamaterials and their engineering applications. Adv Eng Mater 21:1800864
7. Zhang J, Lu G, You Z (2020) Large deformation and energy absorption of additively manufactured auxetic materials and structures: A review. Compos Part B Eng 201:108340. https://doi.org/10.1016/j.compositesb.2020.108340
8. Gibson LJ, Ashby MF (1999) Cellular solids: structure and properties. Cambridge university press
9. Ubaid J, Schneider J, Deshpande VS, et al (2022) Multifunctionality of nanoengineered self-sensing lattices enabled by additive manufacturing. Adv Eng Mater
10. Evans KE, Nkansah MA, Hutchinson IJ, Rogers SC (1991) Molecular network design. Nature 353:124
11. Ren X, Das R, Tran P, et al (2018) Auxetic metamaterials and structures: a review. Smart Mater Struct 27:23001
12. Linforth S, Ngo T, Tran P, et al (2021) Investigation of the auxetic oval structure for energy absorption through quasi-static and dynamic experiments. Int J Impact Eng 147:103741. https://doi.org/10.1016/j.ijimpeng.2020.103741
13. Askari M, Hutchins DA, Thomas PJ, et al (2020) Additive manufacturing of metamaterials: A review. Addit Manuf 36:101562. https://doi.org/10.1016/j.addma.2020.101562
14. Robert F (1985) An isotropic three-dimensional structure with Poisson's ratio=- 1. J Elast 15:427–430
15. Grima JN, Gatt R, Alderson A, Evans KE (2005) On the potential of connected stars as

auxetic systems. Mol Simul 31:925–935

16. Ai L, Gao XL (2018) An analytical model for star-shaped re-entrant lattice structures with the orthotropic symmetry and negative Poisson's ratios. Int J Mech Sci 145:158–170. https://doi.org/10.1016/j.ijmecsci.2018.06.027
17. Rad MS, Hatami H, Ahmad Z, Yasuri AK (2019) Analytical solution and finite element approach to the dense re-entrant unit cells of auxetic structures. Acta Mech 230:2171–2185. https://doi.org/10.1007/s00707-019-02387-x
18. Zhang W, Zhao S, Sun R, et al (2019) In-plane mechanical behavior of a new star-re-entrant hierarchical metamaterial. Polymers (Basel) 11:. https://doi.org/10.3390/polym11071132
19. Yang H, Wang B, Ma L (2019) Mechanical properties of 3D double-U auxetic structures. Int J Solids Struct 180:13–29
20. Qiao J, Chen CQ (2015) Analyses on the in-plane impact resistance of auxetic double arrowhead honeycombs. J Appl Mech Trans ASME 82:1–9. https://doi.org/10.1115/1.4030007
21. Gao Q, Wang L, Zhou Z, et al (2018) Theoretical, numerical and experimental analysis of three-dimensional double-V honeycomb. Mater Des 139:380–391. https://doi.org/10.1016/j.matdes.2017.11.024
22. Li X, Lu Z, Yang Z, Yang C (2017) Directions dependence of the elastic properties of a 3D augmented re-entrant cellular structure. Mater Des 134:151–162
23. Wu X, Su Y, Shi J (2020) In-plane impact resistance enhancement with a graded cell-wall angle design for auxetic metamaterials. Compos Struct 247:112451
24. Alomarah A, Ruan D, Masood S, et al (2018) An investigation of in-plane tensile properties of re-entrant chiral auxetic structure. Int J Adv Manuf Technol 96:2013–2029. https://doi.org/10.1007/s00170-018-1605-x
25. Lu Z-X, Li X, Yang Z-Y, Xie F (2016) Novel structure with negative Poisson's ratio and enhanced Young's modulus. Compos Struct 138:243–252
26. Duan S, Xi L, Wen W, Fang D (2020) A novel design method for 3D positive and negative Poisson's ratio material based on tension-twist coupling effects. Compos Struct 236:111899
27. Gao Q, Wang L, Zhou Z, et al (2018) Theoretical, numerical and experimental analysis of three-dimensional double-V honeycomb. Mater \& Des 139:380–391
28. Zhang W, Zhao S, Scarpa F, et al (2021) In-plane mechanical behavior of novel auxetic hybrid metamaterials. Thin-Walled Struct 159:.

https://doi.org/10.1016/j.tws.2020.107191

29. Qi C, Jiang F, Remennikov A, et al (2020) Quasi-static crushing behavior of novel re-entrant circular auxetic honeycombs. Compos Part B Eng 197:108117. https://doi.org/10.1016/j.compositesb.2020.108117
30. Alomarah A, Ruan D, Masood S (2018) Tensile properties of an auxetic structure with re-entrant and chiral features—a finite element study. Int J Adv Manuf Technol 99:2425–2440. https://doi.org/10.1007/s00170-018-2637-y
31. Qiao JX, Chen CQ (2015) Impact resistance of uniform and functionally graded auxetic double arrowhead honeycombs. Int J Impact Eng 83:47–58
32. Zhang WM, Li ZY, Yang JS, et al (2022) A lightweight rotationally arranged auxetic structure with excellent energy absorption performance. Mech Mater 166:. https://doi.org/10.1016/j.mechmat.2022.104244
33. Ingrole A, Hao A, Liang R (2017) Design and modeling of auxetic and hybrid honeycomb structures for in-plane property enhancement. Mater Des 117:72–83. https://doi.org/10.1016/j.matdes.2016.12.067
34. Quan C, Han B, Hou Z, et al (2020) 3D Printed Continuous Fiber Reinforced Composite Auxetic Honeycomb Structures. Compos Part B Eng 187:. https://doi.org/10.1016/j.compositesb.2020.107858
35. Bai L, Gong C, Chen X, et al (2020) Mechanical properties and energy absorption capabilities of functionally graded lattice structures: Experiments and simulations. Int J Mech Sci 182:. https://doi.org/10.1016/j.ijmecsci.2020.105735
36. Alomarah A, Masood SH, Sbarski I, et al (2020) Compressive properties of 3D printed auxetic structures: experimental and numerical studies. Virtual Phys Prototyp 15:1–21. https://doi.org/10.1080/17452759.2019.1644184
37. Dong Z, Li Y, Zhao T, et al (2019) Experimental and numerical studies on the compressive mechanical properties of the metallic auxetic reentrant honeycomb. Mater \& Des 182:108036
38. Wang T, Wang L, Ma Z, Hulbert GM (2018) Elastic analysis of auxetic cellular structure consisting of re-entrant hexagonal cells using a strain-based expansion homogenization method. Mater \& Des 160:284–293
39. Baran T, Öztürk M (2020) In-plane elasticity of a strengthened re-entrant honeycomb cell. Eur J Mech A/Solids 83:. https://doi.org/10.1016/j.euromechsol.2020.104037
40. Vyavahare S, Kumar S (2021) Numerical and experimental investigation of FDM fabricated re-entrant auxetic structures of ABS and PLA materials under compressive

loading. Rapid Prototyp J 27:223–244. https://doi.org/10.1108/RPJ-10-2019-0271

41. Zied K, Osman M, Elmahdy T (2015) Enhancement of the in-plane stiffness of the hexagonal re-entrant auxetic honeycomb cores. Phys Status Solidi Basic Res 252:2685–2692. https://doi.org/10.1002/pssb.201552164
42. Yang L, Harrysson O, West H, Cormier D (2013) Modeling of uniaxial compression in a 3D periodic re-entrant lattice structure. J Mater Sci 48:1413–1422. https://doi.org/10.1007/s10853-012-6892-2
43. Lu ZX, Li X, Yang ZY, Xie F (2016) Novel structure with negative Poisson's ratio and enhanced Young's modulus. Compos Struct 138:243–252. https://doi.org/10.1016/j.compstruct.2015.11.036
44. Zhu Y, Luo Y, Gao D, et al (2022) In-plane elastic properties of a novel re-entrant auxetic honeycomb with zigzag inclined ligaments. Eng Struct 268:114788. https://doi.org/10.1016/j.engstruct.2022.114788
45. Chen Z, Wu X, Xie YM, et al (2020) Re-entrant auxetic lattices with enhanced stiffness: A numerical study. Int J Mech Sci 178:. https://doi.org/10.1016/j.ijmecsci.2020.105619
46. Li X, Wang Q, Yang Z, Lu Z (2019) Novel auxetic structures with enhanced mechanical properties. Extrem Mech Lett 27:59–65
47. Deshpande VS, Fleck NA (2000) Isotropic constitutive models for metallic foams. J Mech Phys Solids 48:1253–1283
48. Fu MH, Chen Y, Hu LL (2017) A novel auxetic honeycomb with enhanced in-plane stiffness and buckling strength. Compos Struct 160:574–585. https://doi.org/10.1016/j.compstruct.2016.10.090
49. Boldrin L, Hummel S, Scarpa F, et al (2016) Dynamic behaviour of auxetic gradient composite hexagonal honeycombs. Compos Struct 149:114–124
50. Xu N, Qian Y, Yu J, Leung CKY (2022) Tensile performance of 3D-printed Strain-Hardening Cementitious Composites (SHCC) considering material parameters, nozzle size and printing pattern. Cem Concr Compos 132:104601. https://doi.org/10.1016/j.cemconcomp.2022.104601
51. Liu J, Nguyen-Van V, Panda B, et al (2022) Additive Manufacturing of Sustainable Construction Materials and Form-finding Structures: A Review on Recent Progresses. 3D Print Addit Manuf 9:12–34. https://doi.org/10.1089/3dp.2020.0331
52. Nguyen-Van V, Choudhry NK, Panda B, et al (2022) Performance of concrete beam reinforced with 3D printed Bioinspired primitive scaffold subjected to three-point bending. Autom Constr 134:104060. https://doi.org/10.1016/j.autcon.2021.104060

53. Rosewitz JA, Choshali HA, Rahbar N (2019) Bioinspired design of architected cement-polymer composites. Cem Concr Compos 96:252–265. https://doi.org/10.1016/j.cemconcomp.2018.12.010
54. Choudhry NK, Panda B, Kumar S (2022) In-plane energy absorption characteristics of a modified re-entrant auxetic structure fabricated via 3D printing. Compos Part B Eng 228:109437
55. Choudhry NK, Panda B (2023) Mechanical Properties of 3D Printed Modified Auxetic Structure: Experimental and Finite Element Study. In: Low Cost Manufacturing Technologies: Proceedings of NERC 2022. Springer, pp 189–200
56. Choudhry NK, Panda B, Kumar S (2023) Enhanced energy absorption performance of 3D printed 2D auxetic lattices. Thin-Walled Struct 186:110650. https://doi.org/10.1016/j.tws.2023.110650
57. Ingrole A, Hao A, Liang R (2017) Design and modeling of auxetic and hybrid honeycomb structures for in-plane property enhancement. Mater Des 117:72–83. https://doi.org/10.1016/j.matdes.2016.12.067
58. Li QM, Magkiriadis I, Harrigan JJ (2006) Compressive strain at the onset of densification of cellular solids. J Cell Plast 42:371–392
59. Li X, Lu Z, Yang Z, Yang C (2018) Anisotropic in-plane mechanical behavior of square honeycombs under off-axis loading. Mater \& Des 158:88–97
60. Hu LL, Luo ZR, Zhang ZY, et al (2019) Mechanical property of re-entrant anti-trichiral honeycombs under large deformation. Compos Part B Eng 163:107–120. https://doi.org/10.1016/j.compositesb.2018.11.010
61. Zhang X, Ding H, An L, Wang X (2015) Numerical investigation on dynamic crushing behavior of auxetic honeycombs with various cell-wall angles. Adv Mech Eng 7:679678
62. Shokri Rad M, Hatami H, Alipouri R, et al (2019) Determination of energy absorption in different cellular auxetic structures. Mech Ind 20:15–20. https://doi.org/10.1051/meca/2019019
63. Wang Q, Li Z, Zhang Y, et al (2020) Ultra-low density architectured metamaterial with superior mechanical properties and energy absorption capability. Compos Part B Eng 202:108379. https://doi.org/10.1016/j.compositesb.2020.108379
64. Alomarah A, Masood SH, Sbarski I, et al (2020) Compressive properties of 3D printed auxetic structures: experimental and numerical studies. Virtual Phys Prototyp 15:1–21
65. Lu H, Wang X, Chen T (2021) In-plane dynamics crushing of a combined auxetic honeycomb with negative Poisson's ratio and enhanced energy absorption. Thin-Walled

Struct 160:107366

66. Lv W, Li D, Dong L (2020) Study on mechanical properties of a hierarchical octet-truss structure. Compos Struct 249:112640. https://doi.org/10.1016/j.compstruct.2020.112640
67. Arjunan A, Zahid S, Baroutaji A, Robinson J (2021) 3D printed auxetic nasopharyngeal swabs for COVID-19 sample collection. J Mech Behav Biomed Mater 114:104175. https://doi.org/10.1016/j.jmbbm.2020.104175
68. Bai L, Gong C, Chen X, et al (2020) Mechanical properties and energy absorption capabilities of functionally graded lattice structures: Experiments and simulations. Int J Mech Sci 182:. https://doi.org/10.1016/j.ijmecsci.2020.105735
69. Tao Y, Kong F, Li Z, et al (2021) A review on voids of 3D printed parts by fused filament fabrication. J Mater Res Technol 15:4860–4879. https://doi.org/10.1016/j.jmrt.2021.10.108
70. Blok LG, Longana ML, Yu H, Woods BKS (2018) An investigation into 3D printing of fibre reinforced thermoplastic composites. Addit Manuf 22:176–186. https://doi.org/10.1016/j.addma.2018.04.039
71. Alam F, Verma P, Mohammad W, et al (2021) Architected poly (lactic acid)/poly (ε-caprolactone)/halloysite nanotube composite scaffolds enabled by 3D printing for biomedical applications. J Mater Sci 56:14070–14083
72. Logakannan KP, Ruan D, Rengaswamy J, et al (2023) Fracture locus of additively manufactured AlSi10Mg alloy. Thin-Walled Struct 184:110460
73. Deshpande VS, Ashby MF, Fleck NA (2001) Foam topology: Bending versus stretching dominated architectures. Acta Mater 49:1035–1040. https://doi.org/10.1016/S1359-6454(00)00379-7
74. Kaw AK (2005) Mechanics of composite materials. CRC press
75. Ashby MF (2006) The properties of foams and lattices. Philos Trans R Soc A Math Phys Eng Sci 364:15–30
76. Maconachie T, Leary M, Lozanovski B, et al (2019) SLM lattice structures: Properties, performance, applications and challenges. Mater \& Des 183:108137
77. Wang H, Chen P, Wu H, et al (2022) Comparative evaluation of printability and compression properties of poly-ether-ether-ketone triply periodic minimal surface scaffolds fabricated by laser powder bed fusion. Addit Manuf 102961
78. Fu M-H, Chen Y, Hu L-L (2017) Bilinear elastic characteristic of enhanced auxetic honeycombs. Compos Struct 175:101–110

79. Harkati A, Boutagouga D, Harkati E, et al (2020) In-plane elastic constants of a new curved cell walls honeycomb concept. Thin-Walled Struct 149:. https://doi.org/10.1016/j.tws.2020.106613
80. Saleh MS, Hu C, Brenneman J, et al (2021) 3D printed three-dimensional metallic microlattices with controlled and tunable mechanical properties. Addit Manuf 39:101856. https://doi.org/10.1016/j.addma.2021.101856
81. Gohar S, Hussain G, Ilyas M, Ali A (2021) Performance of 3D printed topologically optimized novel auxetic structures under compressive loading: experimental and FE analyses. J Mater Res Technol 15:394–408. https://doi.org/10.1016/j.jmrt.2021.07.149
82. Quan C, Han B, Hou Z, et al (2020) 3d printed continuous fiber reinforced composite auxetic honeycomb structures. Compos Part B Eng 187:. https://doi.org/10.1016/j.compositesb.2020.107858
83. Sun ZP, Guo YB, Shim VPW (2022) Static and dynamic crushing of polymeric lattices fabricated by fused deposition modelling and selective laser sintering – an experimental investigation. Int J Impact Eng 160:104059. https://doi.org/10.1016/j.ijimpeng.2021.104059
84. Sun ZP, Guo YB, Shim VPW (2021) Characterisation and modeling of additively-manufactured polymeric hybrid lattice structures for energy absorption. Int J Mech Sci 191:106101. https://doi.org/10.1016/j.ijmecsci.2020.106101
85. Wang S, Ding Y, Yu F, et al (2020) Crushing behavior and deformation mechanism of additively manufactured Voronoi-based random open-cell polymer foams. Mater Today Commun 25:101406. https://doi.org/10.1016/j.mtcomm.2020.101406
86. Habib FN, Iovenitti P, Masood SH, Nikzad M (2018) Fabrication of polymeric lattice structures for optimum energy absorption using Multi Jet Fusion technology. Mater Des 155:86–98. https://doi.org/10.1016/j.matdes.2018.05.059
87. Guo M-F, Yang H, Ma L (2022) 3D lightweight double arrow-head plate-lattice auxetic structures with enhanced stiffness and energy absorption performance. Compos Struct 290:115484. https://doi.org/10.1016/j.compstruct.2022.115484
88. Bhate D, Penick CA, Ferry LA, Lee C (2019) Classification and selection of cellular materials in mechanical design: Engineering and biomimetic approaches. Designs 3:1–31. https://doi.org/10.3390/designs3010019
89. Bell SB, Holroyd FC (1991) Tesseral amalgamators and hierarchical tessellations. Image Vis Comput 9:313–328. https://doi.org/10.1016/0262-8856(91)90036-O
90. Zhang Q, Yang X, Li P, et al (2015) Bioinspired engineering of honeycomb structure -

Using nature to inspire human innovation. Prog Mater Sci 74:332–400. https://doi.org/10.1016/j.pmatsci.2015.05.001

91. Seidel R, Lyons K, Blumer M, et al (2016) Ultrastructural and developmental features of the tessellated endoskeleton of elasmobranchs (sharks and rays). J Anat 229:681–702. https://doi.org/10.1111/joa.12508
92. Tadayon M, Amini S, Wang Z, Miserez A (2018) Biomechanical Design of the Mantis Shrimp Saddle: A Biomineralized Spring Used for Rapid Raptorial Strikes. iScience 8:271–282. https://doi.org/10.1016/j.isci.2018.08.022
93. Mendoza-Galván A, Del Río LF, Järrendahl K, Arwin H (2018) Graded pitch profile for the helicoidal broadband reflector and left-handed circularly polarizing cuticle of the scarab beetle Chrysina chrysargyrea. Sci Rep 8:1–12. https://doi.org/10.1038/s41598-018-24761-w
94. Babaee S, Shim J, Weaver JC, et al (2013) 3D soft metamaterials with negative poisson's ratio. Adv Mater 25:5044–5049. https://doi.org/10.1002/adma.201301986
95. Yuan S, Shen F, Bai J, et al (2017) 3D soft auxetic lattice structures fabricated by selective laser sintering: TPU powder evaluation and process optimization. Mater Des 120:317–327. https://doi.org/10.1016/j.matdes.2017.01.098
96. Bhat C, Kumar A, Jeng J-Y (2021) Effect of atomic tessellations on structural and functional properties of additive manufactured lattice structures. Addit Manuf 47:102326
97. Hao W, Liu J, Kanwal H (2023) Compressive properties of cementitious composites reinforced by 3D printed PA 6 lattice. Polym Test 117:107811. https://doi.org/10.1016/j.polymertesting.2022.107811
98. Choi JB (1996) Fracture toughness of re-entrant foam materials with a negative Poisson's ratio: Experiment and analysis. Int J Fract 80:73–83. https://doi.org/10.1007/BF00036481
99. Argatov II, Guinovart-Díaz R, Sabina FJ (2012) On local indentation and impact compliance of isotropic auxetic materials from the continuum mechanics viewpoint. Int J Eng Sci 54:42–57. https://doi.org/10.1016/j.ijengsci.2012.01.010
100. Novak N, Krstulović-Opara L, Ren Z, Vesenjak M (2020) Compression and shear behaviour of graded chiral auxetic structures. Mech Mater 148:. https://doi.org/10.1016/j.mechmat.2020.103524
101. Henyš P, Vomáčko V, Ackermann M, et al (2019) Normal and shear behaviours of the auxetic metamaterials: homogenisation and experimental approaches. Meccanica

54:831–839. https://doi.org/10.1007/s11012-019-01000-8

102. Choi JB, Lakes RS (1992) Non-linear properties of polymer cellular materials with a negative Poisson's ratio. J Mater Sci 27:4678–4684. https://doi.org/10.1007/BF01166005
103. Imbalzano G, Tran P, Lee PVS, et al (2016) Influences of material and geometry in the performance of auxetic composite structure under blast loading. In: Applied Mechanics and Materials. pp 476–481
104. Farina I, Fabbrocino F, Carpentieri G, et al (2016) On the reinforcement of cement mortars through 3D printed polymeric and metallic fibers. Compos Part B Eng 90:76–85. https://doi.org/10.1016/j.compositesb.2015.12.006
105. Zhong R, Ren X, Yu Zhang X, et al (2022) Mechanical properties of concrete composites with auxetic single and layered honeycomb structures. Constr Build Mater 322:126453. https://doi.org/10.1016/j.conbuildmat.2022.126453
106. Chawla K, Kiran R (2022) Numerical predictions for the effect of negative Poisson's ratio on thermoelastic properties of triply periodic minimal surface-based composites. Results Mater 14:100273. https://doi.org/10.1016/j.rinma.2022.100273
107. Wang W, Sheikh MN, Hadi MNS (2016) Axial compressive behaviour of concrete confined with polymer grid. Mater Struct Constr 49:3893–3908. https://doi.org/10.1617/s11527-015-0761-9
108. GangaRao HVS, Taly N, Vijay P V (2006) Reinforced concrete design with FRP composites. CRC press
109. Zhao C, Goh KL, Lee HP, et al (2023) Experimental study and finite element analysis on energy absorption of carbon fiber reinforced composite auxetic structures filled with aluminum foam. Compos Struct 303:116319. https://doi.org/10.1016/j.compstruct.2022.116319

List of Publications

Publications from Ph.D. Thesis

(A) Journal Publications:

1. Choudhry, N. K., Panda, B., & Kumar, S. (2022). In-plane energy absorption characteristics of a modified re-entrant auxetic structure fabricated via 3D printing. *Composites Part B: Engineering*, *228*, 109437.
2. Choudhry, N. K., Panda B, Kumar S. Enhanced energy absorption performance of 3D printed 2D auxetic lattices. Thin-Walled Struct 2023;186:110650. https://doi.org/10.1016/j.tws.2023.110650.
3. Choudhry, N. K., Panda B, Dixit US. Energy Absorption Characteristics of Fused Deposition Modeling 3D Printed Auxetic Re-entrant Structures : A Review. J Mater Eng Perform 2023. https://doi.org/10.1007/s11665-023-08243-3.
4. Choudhry, N. K., Nguyen, T. K., Panda, B. & Tran, P. Crushing behavior of cementitious composites reinforced with 3D printed auxetic lattice structures: Experiments and modelling. Cement and Concrete Composites (under review).
5. Choudhry, N. K., Panda, B., Kumar, A & Kumar, S. Tessellation controlled mechanical properties of 3D printed auxetic structures. Additive Manufacturing (under review).

(B) Book Chapter:

1. Choudhry, N. K., Panda B (2023) Mechanical Properties of 3D Printed Modified Auxetic Structure: Experimental and Finite Element Study. In: Low Cost Manufacturing Technologies: Proceedings of NERC 2022. Springer, pp 189–200.

Publications from other collaborative research projects

(A) Journal Publications:

1. Nguyen-Van, V., Choudhry, N. K., Panda, B., Nguyen-Xuan, H., & Tran, P. (2022). Performance of concrete beam reinforced with 3D printed Bioinspired primitive scaffold subjected to three-point bending. *Automation in Construction*, *134*, 104060.

(B) Conference Publications:

1. Choudhry, N. K., Bankar, S. R., Panda, B., & Singh, H. (2021). Experimental and numerical analysis of the bending behavior of 3D printed modified auxetic sandwich structures. *Materials Today: Proceedings*.
2. Miah, M. J., Patoary, M. M. H., Ali, M. K., Paul, S. C., Babafemi, A. J., Choudhry, N. K., & Panda, B. (2021). Effect of chemically treated recycled tire aggregate on the resistance to chloride ion penetration of concrete. *Materials Today: Proceedings*.

(C) Conference, Seminar, Workshop Participation/Presentations:

1. Choudhry, N. K., Harshvardhan V., & Panda, B. Development of Ceramic Clay Printer. Innovation & Entrepreneurship conclave IEC 2022.
2. Singh, A.P, Choudhry, N. K., & Panda, B. Optimization of printing process parameters for Dual-material FDM 3D printing. BIO-Remedi 2022.
3. Boda, Ramalingaiah, Choudhry, N. K., Panda, B. & Kumar S. Numerical evaluation of hybrid 3D porous cellular biomaterials for bone implant application. BIO-Remedi 2022.